CANCER IMAGING AND TREATMENT MONITORING WITH COLOR MAGNETIC PARTICLE IMAGING

A DISSERTATION SUBMITTED TO

THE GRADUATE SCHOOL OF ENGINEERING AND SCIENCE

OF BILKENT UNIVERSITY

IN PARTIAL FULFILLMENT OF THE REQUIREMENTS FOR

THE DEGREE OF

DOCTOR OF PHILOSOPHY

IN

ELECTRICAL AND ELECTRONICS ENGINEERING

By

Mustafa Ütkür

September 2021

CANCER IMAGING AND TREATMENT MONITORING WITH COLOR MAGNETIC PARTICLE IMAGING

By Mustafa Ütkür

September 2021

We certify that we have read this dissertation and that in our opinion it is fully adequate, in scope and in quality, as a dissertation for the degree of Doctor of Philosophy.

Emine Ülkü Sarıtaş Çukur(Advisor)

Ergin Atalar

Nevzat Güneri Gençer

Urartu Özgür Şafak Şeker

Esin Öztürk Işık

Approved for the Graduate School of Engineering and Science:

Ezhan Karaşan
Director of the Graduate School

ABSTRACT

CANCER IMAGING AND TREATMENT MONITORING WITH COLOR MAGNETIC PARTICLE IMAGING

Mustafa Ütkür
Ph.D. in Electrical and Electronics Engineering
Advisor: Emine Ülkü Sarıtaş Çukur
September 2021

Magnetic particle imaging (MPI) is emerging as a highly promising non-invasive tomographic imaging modality for cancer research. Superparamagnetic iron oxide nanoparticles (SPIONs) are used as imaging tracers in MPI. By exploiting the relaxation behavior of SPIONs, the capabilities of MPI can also be broadened to functional imaging applications that can distinguish different nanoparticles and/or environments. One of the important applications of functional MPI is viscosity mapping, since certain cancer types are shown to have increased cellular viscosity levels. MPI can potentially detect these cancerous tissues through estimating the viscosity levels of the tissue environment. Another important application area of MPI is temperature mapping, since SPIONs are also utilized in magnetic fluid hyperthermia (MFH) treatments and MPI enables localized application of MFH. To achieve accurate temperature estimations, however, one must also take into account the confounding effects of viscosity and temperature on the MPI signal. This dissertation studies relaxation-based viscosity and temperature mapping with MPI, covering the biologically relevant viscosity range ($<$5 mPa·s) and the therapeutically applicable temperature range (25-45°C). The characterization of the SPION relaxation response was performed on an in-house arbitrary-waveform magnetic particle spectrometer (MPS) setup, and the imaging experiments were performed on an in-house MPI scanner. Both the MPS setup and the MPI scanner were designed and developed as parts of this thesis. The effects of viscosity and temperature on relaxation time constant estimations were investigated, and the sensitivities of MPI to these functional parameters were determined at a wide range of operating points. The relaxation time constants, τ's, were estimated with a technique called TAURUS (TAU, τ, estimation via Recovery of Underlying mirror Symmetry), which is based on a linear relaxation equation. Although the nonlinear relaxation behaviors of the SPIONs are highly dependent on the excitation field parameters, SPION type, and the hardware configuration, the results suggest that one-to-one relation between the estimated τ and the targeted functional parameters (i.e., viscosity or temperature) can

be obtained. According to these results, MPI can successfully map viscosity and temperature, with higher than 30%/mPa/s sensitivity for viscosity mapping and approximately 10%/°C sensitivity for temperature mapping, at 10 kHz drive field frequency. In addition, the results suggest that the simultaneous mapping of viscosity and temperature can be achieved by performing multiple measurements at different drive field frequencies and/or amplitudes. Overall, these findings show that hybrid MPI-MFH systems offer a promising approach for real-time monitored and localized thermal ablation treatment of cancer. The viscosity and temperature mapping capabilities of MPI via relaxation time constant estimation can provide feedback for high accuracy thermal dose adjustment to the cancerous tissues, thereby, increasing the efficacy of the treatment.

Keywords: Magnetic particle imaging, superparamagnetic iron oxide nanoparticles, nanoparticle relaxation, temperature mapping, viscosity mapping.

ÖZET

RENKLİ MANYETİK PARÇACIK GÖRÜNTÜLEME İLE KANSER GÖRÜNTÜLEME VE TEDAVİ İZLEME

Mustafa Ütkür
Elektrik ve Elektronik Mühendisliği, Doktora
Tez Danışmanı: Emine Ülkü Sarıtaş Çukur
Eylül 2021

Manyetik parçacık görüntüleme (MPG), kanser araştırmaları için oldukça umut verici bir non-invaziv tomografik görüntüleme yöntemi olarak ortaya çıkmaktadır. Süperparamanyetik demir oksit nanoparçacıkları (SPDON'ları), MPG'de görüntüleme izleyicileri olarak kullanılır. SPDON'ların relaksasyon davranışından yararlanılarak MPG'nin yetenekleri, farklı nanoparçacıkları ve/veya ortamları ayırt edebilen fonksiyonel görüntüleme uygulamalarına genişletilebilir. Fonksiyonel MPG'nin önemli uygulamalarından biri viskozite haritalamasıdır, çünkü belirli kanser türlerinin hücresel viskozite seviyelerini artırdığı daha önce gösterilmiştir. MPG, doku ortamının viskozite seviyelerini ölçerek kanserli dokuları potansiyel olarak tespit edebilir. MPG'nin bir diğer önemli uygulama alanı ise sıcaklık haritalamasıdır, çünkü SPDON'lar manyetik alanlı hipertermi (MAH) tedavilerinde de kullanılır, ve MPG ile bölgesel MAH uygulaması mümkün hale gelmektedir. Bununla birlikte, doğru sıcaklık ölçümleri gerçekleştirebilmek için viskozite ve sıcaklığın MPG sinyali üzerindeki karışıklığa neden olan etkileri de hesaba katılmalıdır. Bu tez, biyolojik olarak anlamlı viskozite aralığını ($<$5 mPa·s) ve terapötik olarak uygulanabilir sıcaklık aralığını (25-45°C) kapsayan MPG ile relaksasyona dayalı viskozite ve sıcaklık haritalanmasını incelemektedir. SPDON'ların relaksasyon yanıtının karakterizasyonu için özel olarak tasarlanmış, her dalga formuyla çalışabilen bir manyetik parçacık spektrometresi (MPS) düzeneğinden yararlanılmıştır, ve görüntüleme deneyleri özel olarak tasarlanmış bir MPG tarayıcısında gerçekleştirilmiştir. Hem MPS düzeneği hem de MPG tarayıcısı bu tezin parçaları olarak tasarlanmış ve geliştirilmiştir. Viskozite ve sıcaklığın relaksasyon zaman sabiti hesaplamalarındaki etkileri incelenmiştir, ve MPG'nin bu fonksiyonel parametrelere olan hassasiyetleri geniş bir aralıkta belirlenmiştir. Relaksasyon zaman sabitleri τ'lar, doğrusal bir relaksasyon denklemine dayanan TAURUS (altta yatan ayna simetrisinin geri kazanımı yoluyla τ tahmini) tekniği ile hesaplanmıştır. SPDON'ların doğrusal olmayan relaksasyon davranışları eksitasyon alanı parametrelerine, SPDON tipine ve donanım konfigürasyonuna büyük ölçüde bağlı olsa

da, τ ile hedeflenmiş fonksiyonel parametreler (yani viskozite veya sıcaklık) arasında birebir bir ilişki kurulabileceği sonuçlarla gösterilmiştir. Bu sonuçlara göre, MPG ile 10 kHz sürücü alan frekansında 30%/mPa/s'den daha yüksek hassasiyetle viskozite haritalama ve yaklaşık 10%/°C hassasiyetle sıcaklık haritalama başarılı bir şekilde gerçekleştirilebilmektedir. Ek olarak bu sonuçlar, viskozite ve sıcaklığın eşzamanlı haritalandırılmasının farklı sürücü alan frekansında ve/veya genliğinde birden fazla ölçüm yaparak elde edilebileceğini göstermektedir. Genel olarak bu bulgular, hibrit MPG-MAH sistemlerinin kanserin gerçek zamanlı takip edilen ve bölgesel uygulanan termal ablasyon tedavisi için umut verici bir yaklaşım sunacağını göstermektedir. MPG'nin relaksasyon zaman sabiti hesaplaması yoluyla viskozite ve sıcaklık haritalama yetenekleri, kanserli dokulara yüksek doğrulukta termal doz ayarı için geri bildirim sağlayacak ve neticede tedavinin etkinliğini artıracaktır.

Anahtar sözcükler: Manyetik parçacık görüntüleme, süperparamanyetik demir oksit nanoparçacıkları, nanoparçacık relaksasyonu, sıcaklık haritalama, viskozite haritalama.

Acknowledgement

I am completing my twelve years of education at Bilkent as a biomedical engineer. In this long but fulfilling adventure, I am thankful to many people for patiently providing me academic as well as personal support over the years.

First of all, I would like to express my deepest gratitude to my advisor and mentor Emine Ülkü Sarıtaş. Who I am today as a researcher is based on her reflection that is projected on me. I have spent more than half of my Bilkent years under her supervision, and I sincerely believe that every student must have such a role model in their life that they can look up to. She had always treated me as if I am her collegue, which encouraged me to become an independent researcher. Regardless of working on either a short homework or a months-long journal paper, she showed me that I must work diligently and spend sleepless nights if necessary because the outcome always includes my signature. I am honored to know and work with her, and be her first doctoral graduate.

I would like to extend my gratitude to the members of thesis examination committee Ergin Atalar and Nevzat Güneri Gençer for their valuable contributions and feedback over the years. I would also like to thank Urartu Özgür Şafak Şeker and Esin Öztürk Işık for accepting to be on the thesis committee, for their valuable time and feedback.

I would also like to acknowledge the following agencies for supporting the work in this thesis: the Scientific and Technological Research Council of Turkey through TÜBITAK Grants 114E167, 115E677, and 217S069, the European Commission through FP7 Marie Curie Career Integration Grant PCIG13-GA-2013-618834, the Turkish Academy of Sciences through GEBIP Young Scientist Outstanding Achievement Award, and the Science Academy through BAGEP Young Scientist Award given to Emine Ülkü Sarıtaş.

I am grateful to have the opportunity to work with the former and current members of our research lab. Yavuz Muslu, Semih Kurt, Rahmi Çağıl, Ecrin Yağız, Toygan Kılıç, Alper Özaslan, Aslı Alpman, Beril Alyüz, Tunç Arslan, Elif Aygün, and Atakan

Topçu have always been very kind and helpful. I would also like to thank UMRAM family, especially Salman Ul Hassan Dar, Bilal Taşdelen, Cemre Arıyürek, Koray Ertan, Uğur Yılmaz, Reyhan Ergün, Aydan Ercingöz, and Elif Ünal, who created a fun and warm office environment. I am fortunate to have the support of my dear friends Denizhan Kara, Dorukhan Güngör, Okan Demir, and Barış Canatan during my Ph.D. years. I also consider myself extremely lucky to have Akbar Alipour in my life, who motivated me in every step of this journey.

Lastly, I would like to thank my family especially my two amazing sisters, Gözde and Özge, for their continuous support and endless love. From the first day of my Ph.D. years till my graduation, there was this one person I can not thank and love enough. When there was no one, she was always there for me. My dearest wife, Ayşe, you deserve all the good things in the world.

After all, I am thankful to all of you for bringing me closer to where I want to be.

MUSTAFA ÜTKÜR
September 2021

Contents

List of Figures

List of Tables

Chapter 1

Introduction

Cancer is the leading cause of death worldwide, and about 10 million people died in 2020 due to cancer, which means that 1 out of every 6 deaths is caused by cancer [1]. By 2030, it is predicted that the number of cancer cases will exceed 20 million and deaths will reach 13 million [2]. Cancer is also one of the deadliest diseases in Turkey, and caused the death of more than 126 thousand people in 2020 [3]. Considering the growing threats of cancer to public health, it is of great importance to develop effective methods in cancer diagnosis and treatment.

1.1 Current Imaging Modalities for Diagnosing Cancer

For the diagnosis and staging of cancer, the following non-invasive medical imaging modalities are being used in the clinics [4, 5]: X-ray (X-ray and computed tomography – CT), nuclear medicine (single photon emission tomography – SPECT and positron emission tomography – PET), magnetic resonance imaging (MRI), ultrasound (US), and near-infrared optical tomography. Since the depth of penetration in ultrasound and optical imaging are limited, only X-ray/CT, SPECT/PET and MRI can detect three dimensional cancer in the whole body. The use of ionizing radiation

in X-ray/CT and the use of radioactive tracers in nuclear medicine are harmful to human health. In addition, the contrast of soft tissues in X-ray/CT is insufficient, and the spatial resolution in nuclear medicine can reach up to 1 cm [6, 7, 8]. Hence, early diagnosis becomes difficult with these modalities.

On the other hand, MRI uses non-ionizing radiation and its spatial resolution can be better than 1 mm [9]. However, functional imaging capability of MRI is not as advanced as nuclear medicine, and it is more suitable for soft-tissue anatomical imaging. In addition, gadolinium contrast agent used for cancer diagnosis carries fatal risks in patients with kidney diseases. Overall, the methods used for cancer research today are either insufficient in early diagnosis or use harmful contrast agents. Considering the increasing number of cancer cases, there is a need for new non-invasive and harmless methods in cancer research.

1.2 Magnetic Particle Imaging (MPI) as an Emerging Imaging Modality for Cancer

Magnetic Particle Imaging (MPI) is a relatively new imaging modality that was first published in 2005 by Gleich and Weizenecker [10], where superparamagnetic iron oxide nanoparticles (SPIONs) are utilized as imaging tracers. MPI is a safe imaging modality especially for patients with chronic kidney disease (CKD), since SPIONs are generally uptaken by Kupffer cells in the reticuloendothelial system, hence, cleared by the liver [11, 12]. Magnetic field frequencies used in MPI are in the relatively low kHz range, hence, MPI does not use ionizing radiation. MPI is a quantitative imaging modality with high sensitivity and high resolution, where the received signal only reflects the SPION concentration without any depth limitation or any background signal from the tissue [13]. The potential biomedical applications of MPI have been rapidly growing and include angiography [13, 14], stem cell tracking [15, 16, 17, 18], perfusion imaging [19, 20, 21], guiding cardiovascular interventions [22, 23, 24], blood flow quantification [25], detecting the changes in cerebral blood volume [26, 27], and cancer imaging [28, 29]. Although there are no human-sized MPI scanners available

in the biomedical market, preclinical MPI scanners for small animal imaging have recently been commercialized. Many preclinical MPI scanners, on the other hand, are developed in laboratory settings [30, 31, 32, 33].

The tumor tissue has more porous structure than healthy tissues, such that SPIONs can leak into these structures due to the enhanced permeability and retention (EPR) effect [34, 35, 36, 28]. Alternatively, SPIONs can also be bounded to tumors via functionalization of their surface with either proteins [37] or labeled white blood cells [38]. Labeling SPIONs is a method frequently used in MRI studies [39, 40, 41, 42, 43]. SPIONs create negative contrast in MRI, and therefore cancer detection can be achieved via detecting the associated local signal losses [44, 45]. However, signal losses can also be observed in the air/tissue boundaries or due to the differences in the magnetic susceptibility among different tissues [46, 47, 48]. This ambiguity makes it difficult to determine the location or quantity of SPIONs with MRI. On the other hand, SPIONs create positive contrast in MPI, where the signal is directly proportional to the SPION concentration [49]. Therefore, the quantification of tumor cells bounded by SPIONs can be directly achieved with MPI [50].

The response of the SPIONs to the applied magnetic field occurs with a certain delay called the relaxation effect. When the magnetic field is suddenly removed, the magnetic moments of the SPIONs return to their easy axis through two different mechanisms: Brownian relaxation via physical rotation, and Néel relaxation via internal rotation [51, 52, 53, 54, 55]. With the combined effect of these two mechanisms, the image becomes blurred and the signal intensity decreases. The details of the relaxation effects are given in Chapter 2. Since a physical rotation takes place in Brownian relaxation, the properties of the medium such as viscosity and temperature have a direct effect on the SPION response. Néel relaxation, on the other hand, is not affected by the viscosity of the medium as it occurs internally, but depends on the temperature of the medium. Recently, several groups have conducted studies to understand and use the relaxation effect in MPI to distinguish different nanoparticle types or chemical environments [56, 57]. The functional imaging potential of MPI has also been shown by estimating the viscosity level of the medium [58, 59, 60]. Certain diseases such as atherosclerosis and cancer are known to lead to increased levels of cellular viscosity [61, 62, 63]. Therefore, cancer imaging with MPI can potentially be performed by

detecting the viscosity level in the tissue.

1.3 Current Treatment Methods for Cancer

On the treatment side of cancer, non-invasive and non-harmful methods are not yet used in the clinics. Apart from surgery, chemotherapy and radiotherapy are mainly used in cancer screening and staging [64]. Hyperthermia is also used as an adjunctive therapy to increase the temperature in the tumor region to higher than 42°C, so that the resistance of tumor reduces and the efficiency of the treatment increases [65, 66, 67, 68, 69, 70]. However, when hyperthermia is used, it is essential to ensure that healthy cells are not damaged, which is typically achieved through temperature measurements using discrete number of temperature probes placed invasively to the region of the treatment [71]. Although this approach gives an idea about the course of treatment, it can not provide the overall distribution of the thermal dose. Alternatively, MRI thermometry was also proposed for hyperthermia treatments performed via high intensity focused ultrasound (HIFU) systems. Temperature-monitored thermal ablation treatments for prostate cancer or breast cancer were achieved with these integrated MRI-HIFU systems, where MRI non-invasively monitors the temperature distribution and HIFU delivers the thermal energy to the tumor tissue [72, 73, 74, 75]. Although the efficacy of the thermal therapy increases with the temperature feedback, there are some drawbacks such as extremely long treatment time reaching up to hours, or technical limitations in HIFU beam conformation, which may result in inhomogeneous thermal dose or damage the nearby healthy tissues [76, 77, 78].

Thermal therapy applications aim to damage the protein structures of tumor tissues with the applied heat, so that they cannot repair the damage in the DNA molecules during ionization radiation in chemotherapy or radiotherapy. As a result, tumor tissues become more sensitive to chemotherapy or radiotherapy and the overall treatment is applied more effectively. In addition, hyperthermia applications also have a physiological effect. With increases in body temperature, blood flow to the heated areas increases, which ensures that more oxygen is transported to those areas. With this process, immunogenicity increases and the immune system begins to react to cancerous

tissues. Therefore, although hyperthermia is used as an adjunctive therapy, it is also possible to use it alone as an immunotherapy in cancer research [79, 80, 81].

SPIONs also have a significant role in the treatment side of the cancer research for many years [82]. Magnetic fluid hyperthermia (MFH) is one of the thermal therapy treatments using SPIONs as nano-sized heat sources. Under AC magnetic field, SPIONs dissipate heat due to relaxation effect causing a hysteresis loss [83, 84, 85]. If a DC magnetic field with a certain amplitude is superimposed on the AC magnetic field, the heating capability of SPIONs would be significantly reduced due to the "saturation" characteristics of SPIONs [86]. Conceptually, MPI already uses the saturation characteristics of the SPIONs that can also be integrated into an MFH treatment. The hardware of MPI and MFH are compatible with each other, enabling hybrid MPI-MFH to be utilized as both an imaging modality and thermal therapy system [87, 88]. Such a system would be a very promising alternative for thermal ablation studies, where the SPIONs are used as efficient heat sources that can be sent to the tumor region and achieve immunogenicity without any depth limitations [28, 89]. While doing that, the selection field in MPI used for spatial encoding can create a high DC field that locks the heating response of SPIONs in healthy tissues [90, 88, 91].

There are three main challenges associated with hyperthermia: Efficiently delivering heat sources to the tumor region, controlling the temperature rise, and preventing the heating of the nearby healthy tissue. All of these challenges can be addressed in MFH with the help of the SPIONs. The tumor tissue has more irregular vascularization compared to healthy tissue, where the SPIONs can easily penetrate into the tumor site via the EPR effect [34, 35, 92, 93, 36, 28]. Alternatively, SPIONs can be functionalized with proteins or white blood cells to be bound to the cancerous tissues [38, 37]. In other words, the heat sources can be sent directly into tumor tissues and achieve immunogenicity [28, 89]. Secondly, there have been many studies on investigating the heating behavior of SPIONs for temperature control, which have generally aimed at synthesizing suitable SPIONs for MFH [94, 95, 96]. The thermal characteristics of SPIONs are directly related to the parameters of the applied AC magnetic field. The heat dissipation increases as the frequency or the amplitude of the applied field increases. Finally, the most critical issue in MFH is to focus the heat only to the cancerous tissues so

that healthy tissues would not be damaged. Although experimental setups have previously been proposed for focusing the magnetic field [86], MPI hardware already has an inherent focusing mechanism created by the selection field magnets [97, 90, 88, 91].

1.4 Motivation

Cancer is one of the leading causes of death worldwide, and the current methods in the diagnosis and treatment of cancer either have insufficiency for early diagnosis or use harmful contrast agents. On the other hand, the potential of MPI and MFH in cancer research shows great promise towards thermal ablation therapies with an hybrid approach. To increase the efficacy of a thermal ablation treatment, however, the thermal dose and the size or location of the tumor region needs to be known during treatment. The main motivation of this thesis is to investigate the relaxation-based SPION responses to perform simultaneous viscosity and temperature mapping with MPI. By doing so, cancer diagnosis via viscosity mapping and treatment monitoring via temperature mapping can be achieved with MPI, which can benefit the MFH treatment in a potential hybrid MPI-MFH system.

1.5 Outline

This thesis presents the potential of MPI in viscosity and temperature mapping. The relaxation behavior of SPIONs underlies the capability of MPI in functional mapping, and a previously proposed relaxation estimation technique called TAURUS (τ, **TAU**, estimation via **R**ecovery of **U**nderlying mirror **S**ymmetry) was utilized in this thesis. The characterization of the SPION relaxation response was performed on an in-house arbitrary-waveform magnetic particle spectrometer (i.e., MPS, or also known as MPI relaxometer), and the imaging demonstrations were performed on an in-house MPI scanner. Both the MPS setup and the MPI scanner were designed and developed for the work presented in this thesis. Overall, the organization of this thesis is provided in the following paragraphs.

An overview of the theoretical background on the SPIONs and how they are used in MPI for spatial encoding and signal generation are presented in Chapter 2, along with the image reconstruction techniques and spatial resolution in MPI. The functional imaging capability of MPI relies on the relaxation behavior of the SPIONs, hence, a detailed background on these relaxation mechanisms is given in this chapter. The previous work on the effect of viscosity on the relaxation time constants estimated by TAURUS is also summarized in this chapter.

In Chapter 3, the design, construction, and testing stages of an MPI scanner is presented. This MPI scanner is developed at Bilkent University National Magnetic Resonance Research Center (UMRAM), and has a 4.8 T/m/μ_0 gradient magnetic field in x-direction, and the maximum FOV is 1.9 cm in x-y direction without any limitation in the z-direction. Although the imaging bore of this MPI scanner is not sufficiently wide for small animal imaging experiments, the proof-of-concept imaging experiments in the following chapters are successfully conducted using this MPI scanner.

The relaxation-based color MPI experiments that distinguish the biologically relevant viscosity range of up to 5 mPa·s are presented in Chapter 4. To find the optimal drive field parameters for viscosity, the color MPI results at three different frequencies are compared. Frequencies around 10 kHz are shown to be well-suited for viscosity mapping using one of the commercially available multi-core cluster SPIONs, namely Nanomag-MIP (Micromod GmbH, Germany). The results provide a one-to-one mapping between the viscosity level and the relaxation time constants that are estimated using TAURUS.

In Chapter 5, the temperature and viscosity sensitivities of MPI at a wide range of operating points are determined to empower simultaneous mapping of these two parameters. To enable these extensive experiments, an in-house arbitrary-waveform MPS setup with temperature-controlled heating capability is developed. The results suggest that the simultaneous mapping of temperature and viscosity can be achieved by performing measurements at two different drive field settings that provide complementary temperature/viscosity sensitivities. Alternatively, temperature mapping alone can be achieved with a single measurement at drive field frequencies where viscosity sensitivity is minimized.

The MPS results in Chapter 5 are extended to color MPI experiments in Chapter 6. The effects of temperature and viscosity on the time constant estimations with TAURUS are investigated via 1D color MPI experiments at three different temperatures. The imaging phantom contains five different SPION samples at different viscosity levels, such that the confounding effects between the two functional parameters can be simultaneously investigated. The imaging experiments are performed at four different drive field amplitudes. The results show the potential of simultaneous temperature and viscosity mapping with MPI by performing two imaging experiments at two different drive field amplitudes.

The results of the functional imaging capabilities of TAURUS presented in this thesis for viscosity and temperature mapping with color MPI are summarized in Chapter 7. The potential extensions of the work in this thesis are also briefly discussed as future work.

Chapter 2

Theoretical Background

2.1 Superparamagnetic Iron Oxide Nanoparticles (SPIONs)

SPIONs are widely used products of biotechnology, thanks to their biocompatibility, low toxicity, and rich surface-functionality properties [98, 99, 100, 101, 102]. SPIONs in the phases of magnetite (Fe_3O_4) or maghemite (γ-Fe_2O_3) are typically used in biomedicine, where the products with magnetite or maghemite (e.g., Feraheme, Resovist, or NanoTherm) already have medical use approvals by FDA and EMA [103, 104, 105]. SPIONs have large magnetic moments that can be manipulated by external magnetic fields. Their remanent magnetization is zero when the applied field is removed, which makes SPIONs maintain colloidal stability and avoid agglomeration. Functionalization of the SPIONs with proteins, enzymes, or antibodies makes them suitable candidates for *in vivo* targeted drug delivery applications. The usage of SPIONs in biomedical technology includes magnetic fluid hyperthermia (MFH) therapies as nano-sized heating agents [106, 107, 108, 109], magnetic resonance imaging (MRI) as contrast agents [110, 111, 112, 113], and magnetic particle imaging (MPI) as imaging tracers [10, 114, 115, 116, 117]. Since this thesis will be primarily focusing on MPI, the discussion regarding SPIONs will be centered around its usage in MPI.

The nonlinear magnetization characteristics of the SPIONs are described by the Langevin physics as depicted in Figure 2.1, where the Langevin function, $\mathscr{L}$, is written as:

$$\mathscr{L}(\xi) = \begin{cases} coth(\xi) - \frac{1}{\xi}, & \xi \neq 0 \\ 0, & \xi = 0 \end{cases} \tag{2.1}$$

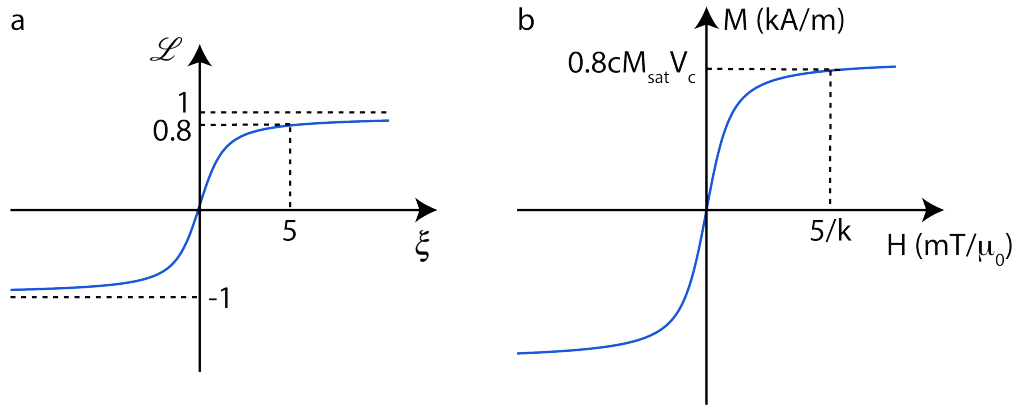

Figure 2.1: (a) The Langevin function given in Equation 2.1 is plotted. Here, the saturation is defined as reaching to 80% of the maximum value [118]. (b) The nonlinear magnetization characteristics of SPIONs are described by the Langevin function, which is weighted with the concentration, c, saturation magnetic moment, M_{sat}, and core volume, V_c, of the SPION. The magnetic moments of SPIONs are fully driven by the applied field when the applied magnetic energy exceeds the internal thermal energy of SPIONs.

SPIONs align their magnetic moments to the applied magnetic field, H. Once the applied field exceeds a certain value, H_{sat}, the magnetization remains in saturation and does not further increase with increasing field amplitude. In other words, when the applied magnetic energy, kH_{sat}, overcomes the internal thermal energy, k_BT, of SPIONs, then they are fully driven by the applied field [119]. The magnetization as a function of the applied field can be expressed as a scaled version of the Langevin function that is weighted with the SPION concentration, c, saturation magnetic moment, M_{sat}, and core volume of the SPION, V_c, as follows [118]:

$$M(H) = cM_{sat}V_c\mathscr{L}(kH) \tag{2.2}$$

where

$$k = \frac{\mu_0 M_{sat} V_c}{k_B T} \tag{2.3}$$

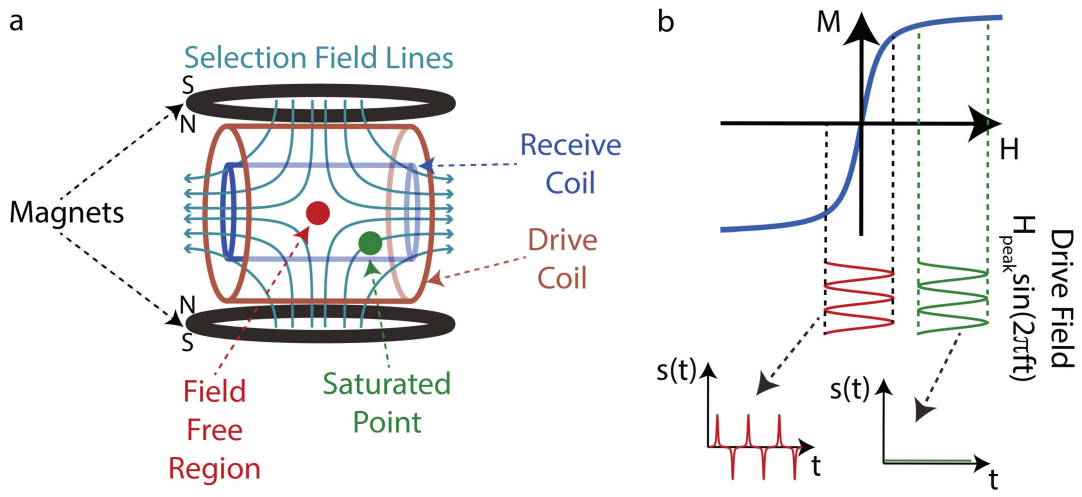

Figure 2.2: (a) An MPI scanner schematic is shown with the static selection field created by magnets with north poles facing each other. The selection field distribution creates a field free region in the middle, and other points in this configuration have a DC magnetic field that typically exceeds H_{sat}. (b) Once a sinusoidal drive field is applied on top of this configuration, only the SPIONs in the field free region will induce signal in the receive coil, and the SPIONs in the saturated regions can not further increase their magnetic moments, and hence, do not have any contribution to the received signal.

Here, μ_0 is the permeability of free space, k_B is the Boltzmann's constant, and T is the temperature.

2.2 MPI Overview

An MPI scanner uses three different magnetic fields for spatial encoding and signal generation of the SPIONs: (1) A static selection field created by magnets to obtain a field-free region (typically a point or a line) so that the SPIONs that are not in this region saturate, (2) a time-varying magnetic field called the drive field to excite SPIONs by scanning the field free region across them, and (3) slowly varying magnetic fields called focus fields to shift the field free region in space so that larger field-of-views can be scanned. Alternatively, the imaging object can also be moved in the selection field instead of using the focus fields. A corresponding schematic is shown in Figure 2.2(a).

When the SPIONs in the field free region are exposed to the drive field, they induce voltage on the receive coil as described by Faraday's law of induction, whereas the SPIONs in the saturation regions do not contribute to the received signal as shown in Figure 2.2(b). The drive field is generally chosen as a single frequency alternating field and the received signal appears in the harmonics of the drive field frequency, since the SPIONs have a nonlinear magnetization response. The MPI image is then reconstructed using these harmonics, so that the spatial distribution of SPIONs can be mapped.

2.2.1 Resolution in MPI

The spatial resolution of MPI is characterized by the full-width-at-half-maximum (FWHM) of the point spread function (PSF). Ideally, PSF of MPI is a delta function such that the MPI image is an exact replica of the SPIO distribution. The actual PSF, however, is related with the derivative of the magnetization curve and can be written using Equation 2.2 as follows:

$$\dot{M}(H) = cM_{sat}V_c k\dot{\mathscr{L}}(kH) \tag{2.4}$$

where the derivative of the Langevin function is expressed as:

$$\dot{\mathscr{L}}(\xi) = \begin{cases} \frac{1}{\xi^2} - \frac{1}{sinh^2(\xi)}, & \xi \neq 0 \\ \frac{1}{3}, & \xi = 0 \end{cases} \tag{2.5}$$

Using the fact that the FWHM of the derivative of the Langevin function in Equation 2.5 is approximately 4.16, the FWHM of the derivative of the magnetization (i.e. PSF in the unit of Tesla) in Equation 2.4 can be written using Equation 2.3 as follows [120]:

$$\Delta H = \frac{4.16}{k} = \frac{4.16k_BT}{\mu_0 M_{sat}V_c} \tag{2.6}$$

where the PSF in the unit of meters can be written using the selection field gradient, G, as follows:

$$\Delta x = \frac{\Delta H}{G} = \frac{4.16}{kG} = \frac{4.16k_BT}{\mu_0 M_{sat}V_c G} \tag{2.7}$$

The resolution of MPI is dependent on both the selection field gradient and the SPION-specific parameters such as saturation magnetization and core volume. While the commercial nanoparticle Resovist is widely used as a reference SPIO, a gold standard SPION is not yet available in MPI. However, SPIONs with different diameters, anisotropic structures, magnetization dynamics, or coatings are heavily studied in the MPI literature [121, 122, 123, 124, 125, 126, 127, 128].

2.2.2 MPI Signal Equation and Image Reconstruction

The excitation of the SPIONs in MPI is performed by a time-varying drive field under a DC selection field. Then, the overall position-dependent and time-varying magnetic field felt by the SPIONs can be written as follows for the 1D case [120, 129]:

$$H(x,t) = H_{peak} cos(2\pi f t) - Gx \tag{2.8}$$

Here, G is the gradient of the selection field, H_{peak} is the drive field peak amplitude, and f is the drive field frequency. The position of the field free region can be calculated by setting Equation 2.8 to zero as follows:

$$x_s(t) = \frac{H_{peak} cos(2\pi f t)}{G} \tag{2.9}$$

Inserting Equation 2.9 into Equation 2.8, and re-writing the magnetization equation in Equation 2.2 yields:

$$M(x,t) = c(x)\delta(y)\delta(z)M_{sat}V_c\mathscr{L}(kG(x_s(t)-x)) \tag{2.10}$$

Here, the density of the SPION distribution is assumed to be along the x-direction. Then, the SPION signal can be written as the time-derivative of the magnetization as follows:

$$\begin{aligned} s(t) &= -\mu_0 \int B_1 \frac{\partial M(u,t)}{\partial t} dV \\ &= -\mu_0 B_1 M_{sat} V_c \int c(u)\delta(v)\delta(w) \frac{\partial \mathscr{L}(kG(x_s(t)-u))}{\partial t} du\,dv\,dw \end{aligned} \tag{2.11}$$

By using the chain rule, this equation becomes:

$$\begin{aligned} s(t) &= \beta \int c(u)\delta(v)\delta(w)\dot{\mathscr{L}}(kG(x_s(t)-u))kG\dot{x_s}(t)\,du\,dv\,dw \\ &= \beta c(x) * \dot{\mathscr{L}}(kGx)\Big|_{x=x_s(t)} kG\dot{x_s}(t) \end{aligned} \tag{2.12}$$

where

$$\beta = -\mu_0 B_1 M_{sat} V_c \tag{2.13}$$

Here, B_1 is the receive coil sensitivity, which is assumed to be independent of the position.

Next, the MPI image can be reconstructed by gridding the SPION signal to the instantaneous position of the field free region as follows [129, 130]:

$$IMG(x_s(t)) = \frac{s(t)}{\beta k G \dot{x_s}(t)} = c(x) * \dot{\mathscr{L}}(kGx)\Big|_{x=x_s(t)} \tag{2.14}$$

In this reconstruction scheme called x-space reconstruction, the spatial distribution of the SPIONs is mapped using the time-domain SPION signal. However, the MPI image is blurred by the PSF of the MPI system, which is the convolution kernel in Equation 2.14 characterized by the derivative of the Langevin function. The blurring in the MPI systems with higher gradient strengths would be lower since the PSF is improved, hence better resolutions can be achieved. Moreover, for the 3D case, the blurring is also related to the scanning trajectory where better resolution is obtained along the scanning direction [130]. Note that, the 1D imaging equation given above can be extended to the multi-dimensional case by following the same steps (i.e., gridding and velocity compensating) [130].

Alternatively, an MPI image can be reconstructed using the frequency components of the SPION signal (called f-space or system function reconstruction). The SPION signal will be periodic in time with the drive field period, T, due to the periodicity of the drive field, hence, can be represented by a Fourier series as follows [120, 131]:

$$s(t) = \sum_{n=-\infty}^{\infty} S_n e^{i2\pi f n t} \tag{2.15}$$

where the Fourier series coefficients, S_n, are defined as follows:

$$S_n = \frac{1}{T} \int_{-T/2}^{T/2} s(t) e^{-i2\pi f n t} dt \tag{2.16}$$

A system matrix is formed by stacking up the frequency components of the SPION signal at each pixel in the field-of-view. Then, the mapping of an arbitrary SPION

distribution (i.e., the object of interest) can be imaged by solving an inverse problem as follows [120, 131]:

$$S\rho = u \tag{2.17}$$

Here, S is the system matrix, u is the acquired SPION signal for the object of interest, and ρ corresponds to the MPI image, which is to be solved for.

In system function reconstruction, once the system function is acquired the MPI imaging can be performed in close to real time. For complex scenarios (e.g., functional imaging purposes that maps different SPION types or parameters), however, extremely long calibration procedures are required to acquire system matrices at each condition. Note that, the blurring due to the non-ideal PSF in x-space reconstruction is already taken care of in the inverse solution.

So far, the SPION responses are assumed to be ideal, where the magnetic moments of SPION align with the drive field instantaneously. In reality, however, the response of the SPIONs to the drive field occurs with a delay due to their relaxation effects, which cause further blurring in the MPI image. The next section provides the detailed background on the relaxation behavior of SPIONs.

2.3 Relaxation Mechanisms of the SPIONs

The behavior of SPIONs under an applied magnetic field is a complex stochastic process due to thermal fluctuations in the microscopic level, and size- or coating-based macroscopic interactions with its environment. According to the adiabatic approximation, the magnetic moments of SPIONs align with the magnetic field instantaneously. In practice, however, the alignment occurs with a lag due to the relaxation effects via two different relaxation processes: Brownian relaxation through a physical rotation of SPIONs, and Néel relaxation through an internal rotation of the magnetic moment within the core volume. The governing equations for these two mechanisms are given as follows [51, 52]:

$$\tau_B = \frac{3\eta V_h}{k_B T} \tag{2.18}$$

and

$$\tau_N = \tau_0 \left(\frac{\sqrt{\pi}}{2} \right) \frac{e^{\sigma}}{\sqrt{\sigma}} \tag{2.19}$$

where

$$\sigma = \frac{KV_c}{k_B T} \tag{2.20}$$

Here, τ_B is the Brownian relaxation time constant, η is the viscosity of the medium, V_h is the hydrodynamic volume of the SPION. In addition, τ_N is the Néel relaxation time constant, τ_0 is the so-called attempt time (in the order of $\sim$1 ns) [132], K is the anisotropy constant of the SPION, and σ is a dimensionless ratio of the anisotropy energy and the internal thermal energy of the SPIONs.

These two mechanisms occur in parallel and the effective relaxation process will be dominated by the one with the faster rotational process (i.e., smaller time constant). Then, the effective time constant, τ_{eff} can be expressed as follows:

$$\tau_{eff} = \left(\frac{1}{\tau_B} + \frac{1}{\tau_N} \right)^{-1} = \frac{\tau_B \tau_N}{\tau_B + \tau_N} \tag{2.21}$$

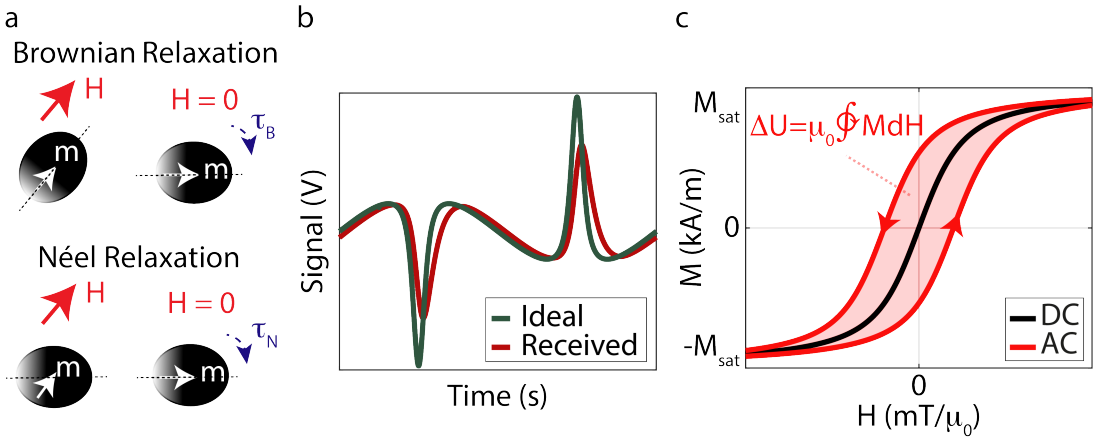

Figure 2.3: (a) Brownian relaxation (i.e., physical rotation) and Néel relaxation (i.e., internal rotation) describes the zero-field relaxation behaviors of the SPIONs. (b) The time-domain SPION response to an AC magnetic field is shown for two cases: The ideal signal with an adiabatic approximation that does not have any relaxation effects, and the actual received signal with the relaxation effects. (c) The magnetization curves of the SPIONs under DC and AC magnetic fields are shown. A hysteresis loop is observed in the AC case where the red shaded area corresponds to the magnetic work done on the SPIONs (ΔU) that result in heat dissipation.

The Brownian and Néel relaxation mechanisms describe the motion of SPION under zero-field conditions (i.e., when the applied field is removed) as depicted in Figure 2.3(a). In MPI, however, zero-field conditions do not fully represent the relaxation mechanism since the excitation of the SPIONs occurs continuously via sinusoidal drive fields.

To have an understanding on how relaxation will effect the MPI signal, firstly, the relaxation process under a DC magnetic field presented by [52, 53, 133, 134] can be investigated. In these studies, the Brownian rotation under small DC-field perturbations applied in parallel with and in perpendicular to the easy axis of the SPION was expressed as follows:

$$\tau_{B,DC,\parallel} = \tau_B \frac{kH\dot{\mathscr{L}}(kH)}{\mathscr{L}(kH)} \tag{2.22}$$

$$\tau_{B,DC,\perp} = \tau_B \frac{2\mathscr{L}(kH)}{kH - \mathscr{L}(kH)} \tag{2.23}$$

In addition, the Néel time constant in the presence of a DC field that is along the easy axis of the SPIONs is expressed as follows [135, 55]:

$$\tau_{N,DC,\parallel} = \tau_N \frac{e^{(kH)^2/(4\sigma)}}{\left(1-(\frac{kH}{2\sigma})^2\right)\left(cosh(kH) - \frac{kH}{2\sigma}sinh(kH)\right)} \tag{2.24}$$

Equations 2.22 - 2.24 were shown to be valid when the magnetic energy is small compared to the anisotropy energy (i.e., $kH < KV_c$). These relations suggest that time constants decrease with field amplitude, which is reasonable since higher applied magnetic energy enables the SPIONs to overcome their internal thermal energy more easily.

The dynamics of SPIONs in a time-varying magnetic field have a more complex nature, and are often discussed via the magnetic susceptibility measurements. To simplify the analysis, the nonlinear magnetization curve in the small field region is linearized as follows:

$$M(H) = \chi H \tag{2.25}$$

Here, the magnetic susceptibility, χ, is considered as the slope of the linear region. According to the theory developed by Debye, χ can be written as a complex quantity with in-phase and out-of-phase components as follows [136]:

$$\chi = \frac{\chi_0}{1+iw\tau_{eff}} = \frac{\chi_0}{1+(w\tau_{eff})^2} - i\frac{\chi_0 w\tau_{eff}}{1+(w\tau_{eff})^2} \tag{2.26}$$

Here, w is the frequency of the applied field in radians per second, τ_{eff} is the effective time constant, and χ_0 is the DC susceptibility, which can be calculated using Equations 2.4 and 2.5 as follows:

$$\chi_0 = \left.\frac{M(H)}{H}\right|_{H=0} = \frac{cM_{sat}V_c k}{3} \tag{2.27}$$

According to the Equation 2.26, the real part of χ decreases monotonically with frequency, whereas the imaginary part has a maximum at $w\tau_{eff} = 1$, at which point the delay in the SPION response is maximum [137, 138]. The location of the peak, however, is highly dependent on the anisotropy, size, and concentration of SPIONs [139]. More importantly, these expressions are only valid for the small amplitude AC magnetic fields that changes the magnetization curve in the linear region. In MPI, however, the drive fields usually saturate the SPION magnetization, hence, it is not straightforward to use Equation 2.26 to observe the effect of the relaxation in the MPI signal. Nevertheless, the overall relaxation effect causes a hysteresis loop in the magnetization curve as shown in Figure 2.3(c). Note that, the area between the hysteresis curves is directly related to the heat dissipation of the SPIONs [132, 140].

An alternative approach to study the relaxation effects in MPI includes a linear relaxation equation in the following form [136, 54, 141]:

$$\dot{M}(x,t) = -\frac{1}{\tau}\left(M(x,t) - M_{ideal}(x,t)\right) \tag{2.28}$$

Here, $M_{ideal}(x,t)$ is the magnetization under the adiabatic conditions (i.e., without the relaxation effects). Solving this differential equation to obtain $M(x,t)$ yields:

$$M(x,t) = M_{ideal}(x,t) * \left(\frac{1}{\tau}e^{-t/\tau}u(t)\right) \tag{2.29}$$

Here, $u(t)$ is the Heaviside step function, τ is the effective time constant, and '$*$' denotes convolution in time domain. By using the principle of reciprocity, the received SPION signal can be expressed using Equations 2.11 and 2.29 as follows, where the relaxation effect is modeled with an exponential kernel [141]:

$$s_{received}(t) = s_{ideal}(t) * \left(\frac{1}{\tau}e^{-t/\tau}u(t)\right) \tag{2.30}$$

Note that, τ corresponds to a single time constant that represents the combined effect of the Brownian and the Néel time constants in the time domain SPION response. The

relaxation behavior of SPIONs delays the signal in time while lowering its amplitude as shown in Figure 2.3(b). Importantly, Equation 2.30 can be directly used to observe the relaxation effects in the time-domain MPI signal.

In the next section, a previously proposed relaxation estimation technique will be explained. This technique estimates the effective time constant in Equation 2.30 and recovers the ideal signal from the received signal.

2.4 A Relaxation Mapping Technique: TAURUS

The ideal MPI signal depicted in Figure 2.3(b) has mirror symmetry property such that the positive and the mirrored negative half cycles (i.e., when negative half cycle is flipped and reflected horizontally) are exactly the same. The received signal, however, loses this property due to relaxation effect occurring in opposing directions for each half cycle. A previously developed time constant estimation technique called TAURUS (τ, **TAU**, estimation via **R**ecovery of **U**nderlying mirror **S**ymmetry) estimates τ in Equation 2.30 and restores the mirror symmetry property between the half cycles. The ideal signal, then, can be estimated by deconvolving the received signal with an exponential kernel having the correct τ in the exponent (see Figure 2.4). Importantly, TAURUS can estimate a time constant directly from the received signal without requiring any a priori information on the SPIONs or their spatial distribution [60, 142, 143]. The formulation is as follows:

$$\tau = \frac{S^*_{pos}(f) + S_{neg}(f)}{i2\pi f \left(S^*_{pos}(f) - S_{neg}(f)\right)} \tag{2.31}$$

Here, $S_{pos}(f)$ and $S_{neg}(f)$ are the Fourier transforms of the positive and negative half cycles of the received signal, respectively, and the superscript '*' sign denotes complex conjugation.

The estimated τ in Equation 2.31 is not the same as the Brownian and/or the Néel time constant, but is rather an unknown combination of the two with dependencies to parameters such as viscosity or temperature. Although the relaxation effect deteriorates the MPI signal, it also provides an important functionality to MPI. Recent

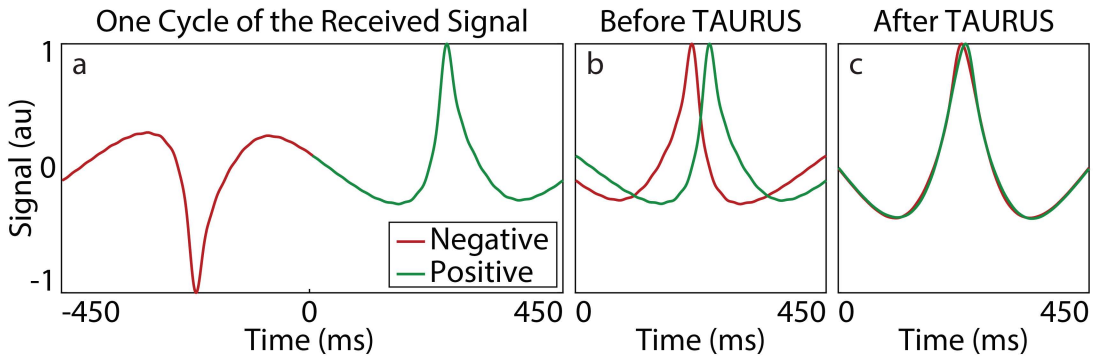

Figure 2.4: (a) One cycle of the received signal is shown. (b) The negative and positive half cycles before TAURUS is plotted on top of each other. (c) After the received signal is deconvolved with the correct relaxation kernel, which is estimated using TAURUS, the mirror symmetry property can be restored.

"color" MPI studies focus on using the relaxation behavior to differentiate different SPIO types and/or chemical environments [57, 56, 142]. One such application with functional MPI is viscosity mapping. Since cancer tissues have higher viscosity levels than healthy tissues [61, 63], MPI can potentially probe cancer through estimating viscosity of the tissue where the SPIONs are located in. Theoretically, the Brownian time constant depends linearly on viscosity, however as mentioned before, MPI signal is acquired with an AC excitation.

2.4.1 Probing Viscosity with TAURUS

In this section, the capability of TAURUS to probe viscosity is explained via proof-of-concept experimental results that were previously measured using an in-house magnetic particle spectrometer (MPS) device [60]. An MPS device can be considered as a zero-dimensional MPI scanner without the selection field magnets that spatially encode SPIONs. Instead, SPION characterization that reflects the MPI response in an imaging experiment can be acquired with MPS using a much simpler hardware configuration. The schematic comparison of these two devices is shown in Figure 2.5. The previously obtained measurement results were performed with an in-house MPS setup at four different frequencies (i.e., 250 Hz, 550 Hz, 1.1 kHz, and 10.8 kHz) and at three different drive field peak amplitudes (i.e., 5 mT/μ_0, 10 mT/μ_0, and 15 mT/μ_0). Further

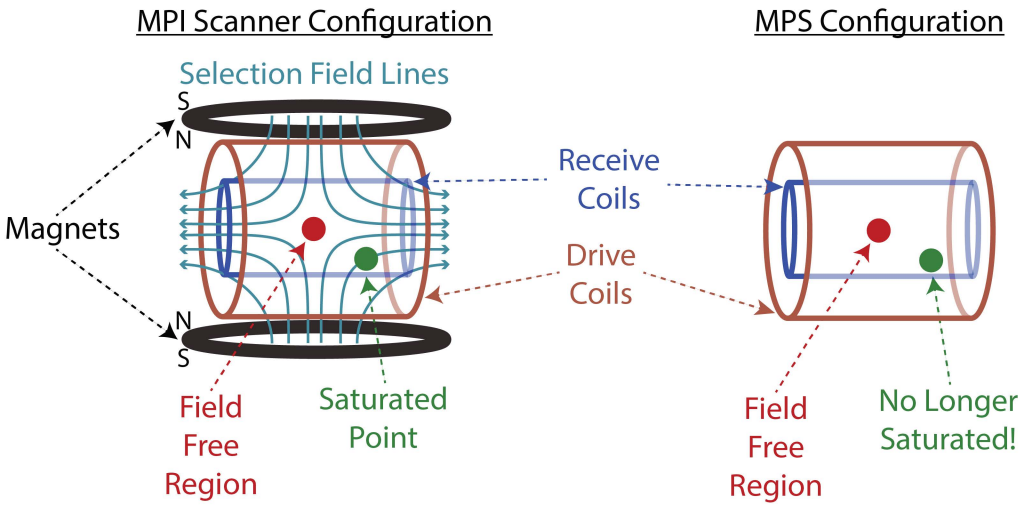

Figure 2.5: The schematic comparison of an MPI scanner (left) and an MPS setup (right) is shown. Here, the only difference between the two setups is the permanent magnets that generate the selection field for spatial encoding. In the MPS case, the SPION samples in the whole measurement chamber induce response in the receive coil, enabling the characterization of the SPION response.

information on signal processing steps are given in [60].

2.4.1.1 Time Constant Estimations with TAURUS

To assess the effect of viscosity on TAURUS, eleven samples with viscosity levels ranging between 0.89 mPa·s and 15.33 mPa·s were previously prepared using a commercially available SPION Nanomag-MIP, and an extensive experimentation was previously performed that contained a total of 396 MPS measurements [60]. For all acquired signals, τ values were estimated using TAURUS as given in Equation 2.31. The resulting τ vs. viscosity curves are presented in Figure 2.6. At fixed frequency, τ decreases with increasing amplitude, which is expected due to easier alignment of the magnetic moments at higher field strengths. τ vs. viscosity curves have a non-monotonic trend at 250 Hz such that τ values first increases sharply up to the viscosity levels of around 2-3 mPa·s and then decreases with increasing viscosity, finally converging to a roughly constant value. As the frequency increases, interestingly, there seems to be a global trend where the τ vs. viscosity curves are scaled down and shifted towards the left. Finally, at 10.8 kHz τ slowly but steadily increases with increasing

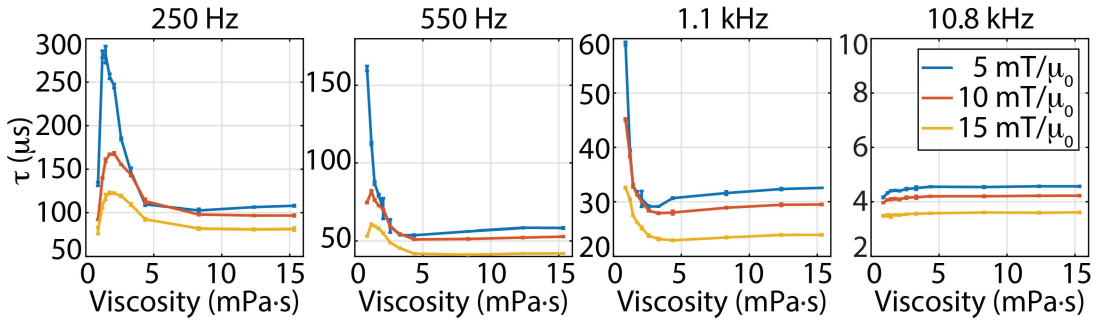

Figure 2.6: Estimated time constants vs. viscosity curves for samples at eleven different viscosity levels between 0.89-15.33 mPa·s. Measurements were performed at four drive field frequencies and three different drive field amplitudes. Error bars denote the standard deviations over three repetition experiments. This figure is reproduced from Ref. [60] by permission of IOP Publishing. All rights reserved. ©Institute of Physics and Engineering in Medicine.

viscosity. Overall, considering the percentage effect of relaxation (τ with respect to the period), the relaxation effects are more prominent at higher frequencies. This is expected as the SPION alignment cannot keep up with the frequency of the applied field.

Theoretically, the Brownian time constant, τ_B, depends linearly on viscosity. However, τ has a more complex relation with the viscosity of the environment as displayed in Figure 2.6 [60]. Yet, viscosity mapping in MPI using TAURUS is possible via characterizing the changes in τ beforehand and working in optimal drive field settings where one-to-one relation is possible (e.g., curves at 1.1 kHz in Figure 2.6).

2.4.1.2 SPIONs in Chemically Different Viscous Environments

An ideal viscosity mapping technique should be able to estimate the viscosity levels independent of the chemical environment of the medium. To ensure that TAURUS actually probes the viscosity level, two chemically different environments (i.e., glycerol and sucrose) were previously examined [144]. A rheometer instrument (Anton Paar, M-PTD200, Austria) was used to measure the dynamic viscosity level of glycerol and sucrose. The measured viscosity levels using this instrument are plotted in Figure 2.7.

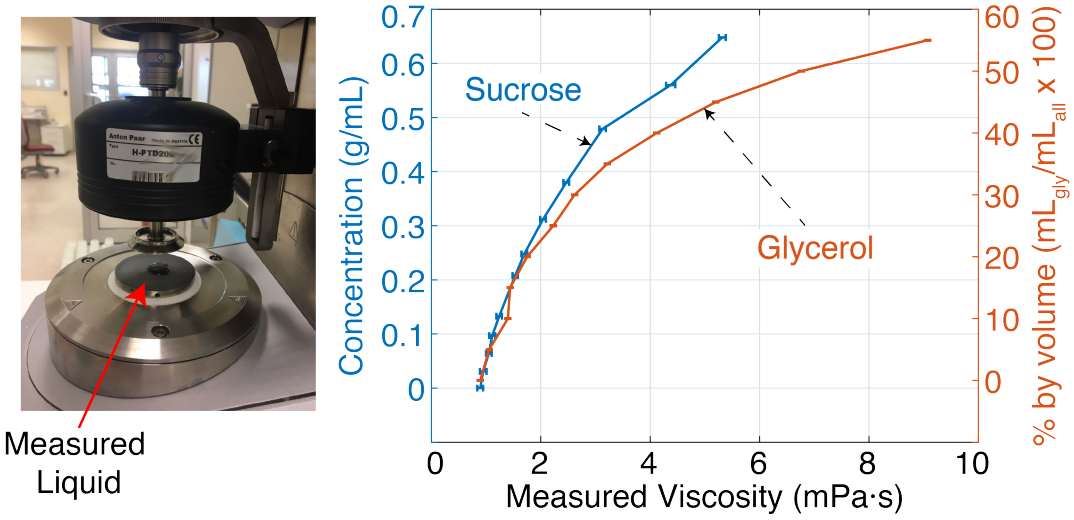

Figure 2.7: The dynamic viscosity measurements of the glycerol/water mixtures and sucrose/water solutions at 25°C were performed using a rheometer instrument. The mean values and standard deviations were calculated over twelve different measurements.

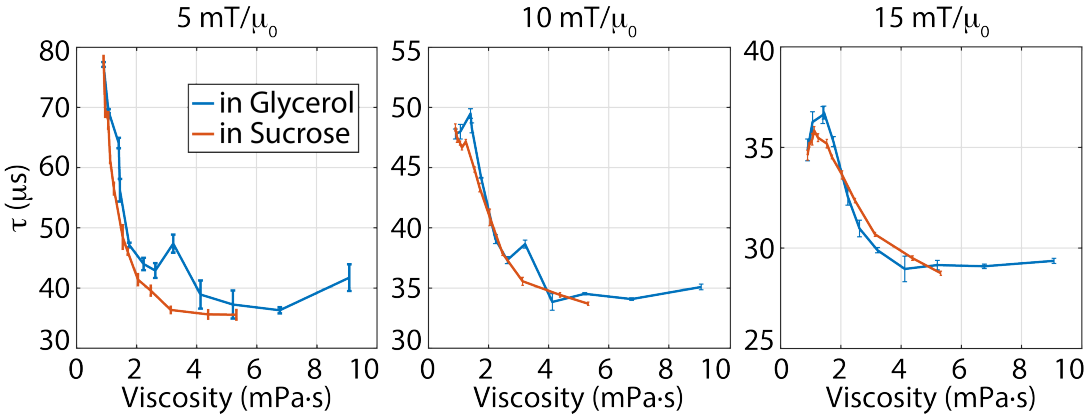

Figure 2.8: The estimated time constant vs. viscosity curves for 11 different glycerol/water mixtures and sucrose/water solutions measured at 1.1 kHz and three different drive field amplitudes: 5 mT/μ_0, 10 mT/μ_0, and 15 mT/μ_0.

The estimated τ results at three different drive field amplitudes are presented in Figure 2.8. τ values in all three field amplitudes first decrease for viscosity values up to 4 mPa·s and then gradually increase for increasing viscosity levels [60]. While a similar trend is observed at all amplitudes, the change in τ is more significant at lower drive field amplitude, which is consistent with the previous results [60]. Under different viscous environments, the estimated time constants demonstrate identical trends, suggesting a direct relation between viscosity and relaxation time constant in the model in Equation 2.31. For example, the rheometer instrument can perform such measurements for a variety of fluids, but only for *in vitro* samples. The results show that estimated τ values with TAURUS yields similar trends for chemically different mediums, building a potential towards future *in vivo* viscosity mapping applications of MPI.

Chapter 3

Design and Construction of a 4.8 T/m/μ_0 MPI Scanner

- M. Utkur, Y. Muslu and E. U. Saritas, "A 4.8 T/m magnetic particle imaging scanner design and construction", Proc. 21st Nat. Biomed. Eng. Meeting (BIYOMUT), pp. 1-4, Nov./Dec. 2017. DOI: 10.1109/BIYOMUT.2017.8479214.

3.1 Introduction

To determine the spatial location of SPIONs in MPI, a gradient magnetic field called the selection field must be generated with the help of permanent magnets or electromagnets. The selection field contains a region where the magnetic field is zero, which is called the field-free-region (FFR). When the SPIONs in FFR are exposed to a time-varying magnetic field (i.e., drive field), they induce a voltage on the receive coil, according to the Faraday's law of induction. The magnetization of SPIONs at locations far from FFR saturates and therefore do not contribute to the received signal. The

drive field is typically chosen as a single frequency AC magnetic field. Since SPIONs have a nonlinear magnetization curve, there will be harmonics in the multiples of the drive field frequency in the received signal. These harmonics are then used to reconstruct the MPI image. Finally, a 3D imaging can be performed by scanning the FFR over the object of interest. In this chapter, the design, construction and testing stages of an in-house MPI scanner with 4.8 T/m/μ_0 selection field gradient and 9.7 kHz drive field frequency that is developed at Bilkent University National Magnetic Resonance Research Center (UMRAM) as part of this thesis are presented in detail.

3.2 Method

For successful acquisition of SPION signal, the hardware components of the in-house MPI scanner consists of a pair of permanent magnets that generate the selection field, a solenoidal drive coil that generates the drive field, a gradiometric receive coil that picks up the SPION response, a copper cylinder for shielding the high frequency interferences, and a linear motion actuator that provides three-dimensional positioning of the imaging phantom.

3.2.1 Permanent Magnet

A pair of 7 cm wide, 2 cm thick disc-shaped neodymium iron boron (NdFeB) permanent magnets with their north poles facing each other were placed at a 8 cm distance from each other as shown in Figure 3.1 The FFR in this configuration resembles a point, hence, the in-house MPI scanner possesses a field-free-point (FFP) topology. The selection field generated by these magnets was measured using a gaussmeter (LakeShore, 475 DSP) by moving its axial probe step by step in the z-direction with the help of a linear motion actuator (Velmex BiSlide). Note that, in this scanner, the FFP position is fixed and the object is moved in the selection field such that the focus field coils are not used.

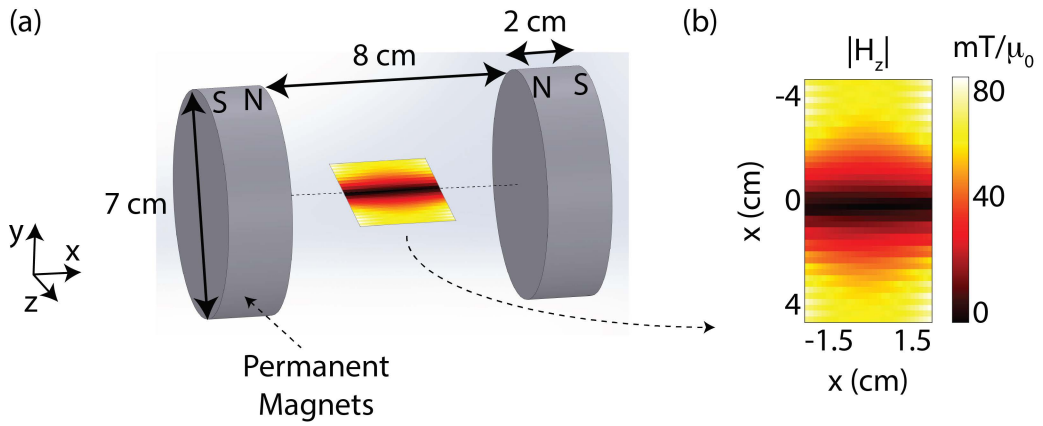

Figure 3.1: (a) The selection field in the in-house MPI scanner was generated with a pair of disc-shaped permanent magnets that are placed 8 cm apart from each other. (b) The field-free-region in this MPI scanner resembles a point, hence, possessing a field-free-point (FFP) topology.

3.2.2 Drive Coil

The drive field amplitudes used in MPI is in the order of mT, and the drive field frequencies is in the order of kHz. Since the received SPION signals depend on the drive field amplitude, the homogeneity of the drive field gains importance according to the size of the region to be imaged. The drive coil in this MPI scanner has inner and outer diameters of 3.2 cm and 3.9 cm, respectively. In addition, it consists of 3 layers of a 1.2 mm diameter (i.e., 125-strand, 40 AWG) Litz wire with 80 turns per layer, resulting in a sensitivity of 1.5 mT/μ_0/A. The homogeneous length of the drive field, where the field remains within 95% of its maximum value, is 4.5 cm in the z-direction. The inductance and internal DC resistance of the drive coil were measured using an LCR meter (GW Instek LCR-8100) as 463 μH and 1.57 Ω, respectively. In Figure 3.2, the drive coil and its magnetic field map simulation using MATLAB are shown.

3.2.3 Receive Coil

In MPI scanners, the induced SPION response is usually picked up by a solenoid coil that is placed coaxially with the drive coil. Their coaxiality causes the drive field to couple with the receive coil and induce voltage on it. This direct-feedthrough signal is

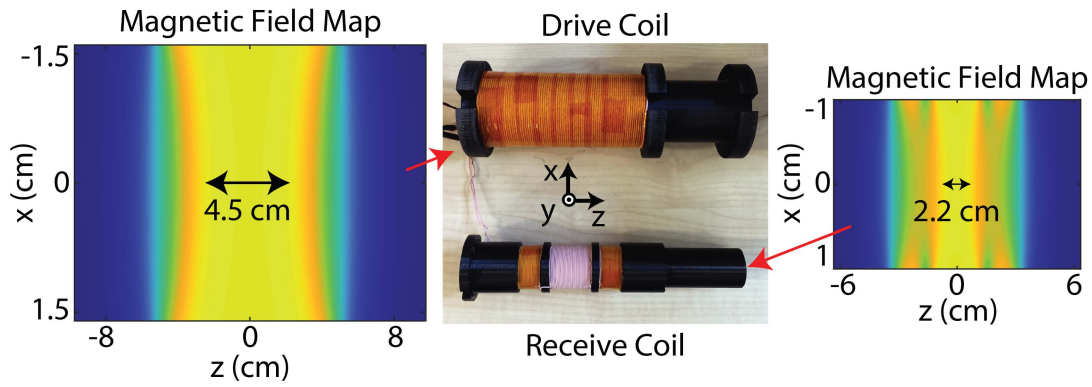

Figure 3.2: The drive and receive coils, and their simulated magnetic field maps in x-z planes. The homogeneous length of the drive field is 4.5 cm within 95% of its maximum value, and the sensitive region of the receive coil drops to its 75% within 2.2 cm. Copyright © 2017, IEEE.

approximately 6 orders of magnitude greater than the voltage induced by the SPIONs. Therefore, one of the essential steps for successful signal acquisition in MPI is to minimize the mutual inductance between the drive and receive coils. For the in-house MPI scanner, the receive coil was designed and developed as a three-section gradiometer-type coil, where the windings on the side sections were wound in the opposite direction with respect to the middle section [145]. The receive coil has inner and outer diameters of 1.9 cm and 2.5 cm, respectively, and it was wound with a 0.8 mm diameter (i.e., 125-strand, 44 AWG) Litz wire in a single layer, with 17.5 turns on the sides and 34 turns in the middle. Each section of the receive coil is separated with a 4 mm gap. The resulting sensitivity at the center of the receive coil was measured using a gaussmeter as 0.5 mT/μ_0/A. The homogeneous region of the receive coil where the sensitivity drops to 75% of its maximum value is 2.2 cm in the z-direction. The self-resonance frequency of this receive coil was measured at 280 kHz using an LCR meter, which corresponds to a distortion in the SPION signal beyond its 28th harmonics when the drive field frequency is 9.7 kHz. The receive coil and its magnetic field map simulation using MATLAB are shown in Figure 3.2.

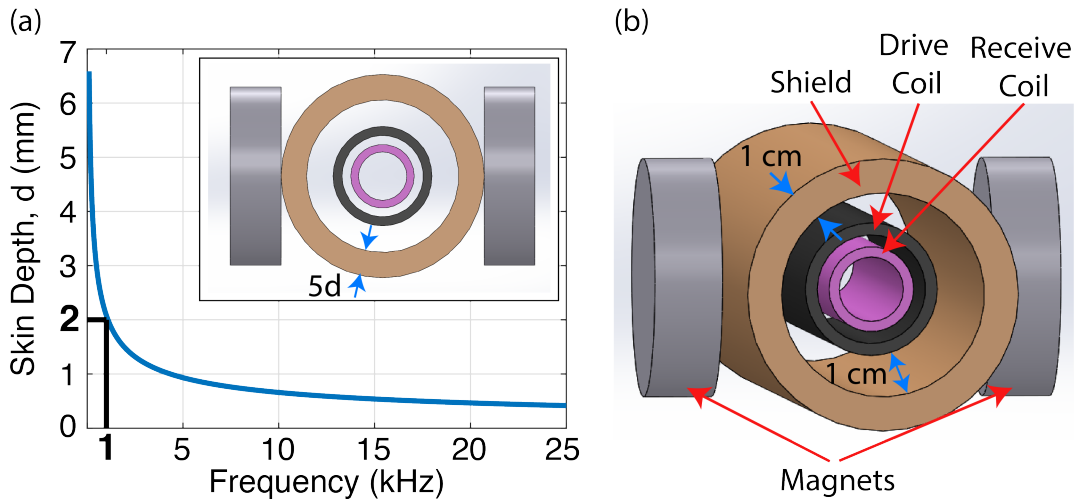

Figure 3.3: (a) The conductor material for the shield is selected as copper, and to be able to operate at as low as 1 kHz drive field frequency, the 2 mm skin-depth of copper at 1 kHz should be considered. Since 99% of the induced eddy currents are concentrated within a layer thickness of 5 times the skin depth, 1 cm shield thickness is utilized in this design. (b) The final Solidworks design of the shield of the in-house MPI scanner as part of the magnets and coil set.

3.2.4 Shield

In addition to the components mentioned above, a cylindrical copper shield was utilized and placed coaxially to the outside of the drive and receive coils to attenuate high frequency interference as shown in Figure 3.3. The selection of the shield thickness is based on the skin depth, d, of the conductor material, where it can be expressed as follows [146]:

$$d = \frac{1}{\sqrt{\pi f \mu_r \mu_0 \sigma}} \tag{3.1}$$

Here, μ_r and σ are the relative permeability and conductivity of the material, respectively. For copper, μ_r = 1 and σ = 58.7 M℧/m.

Typically, a shielding thickness of 5 times the skin depths is enough to reduce the interference, since the 99% of the current flows within this layer. To be able to perform imaging experiments at drive field frequencies as low as 1 kHz, the thickness of the copper shield is selected as 1 cm, as shown in Figure 3.3. Furthermore, the drive coil and the shield are separated by a gap of 1 cm to minimize the eddy current losses on

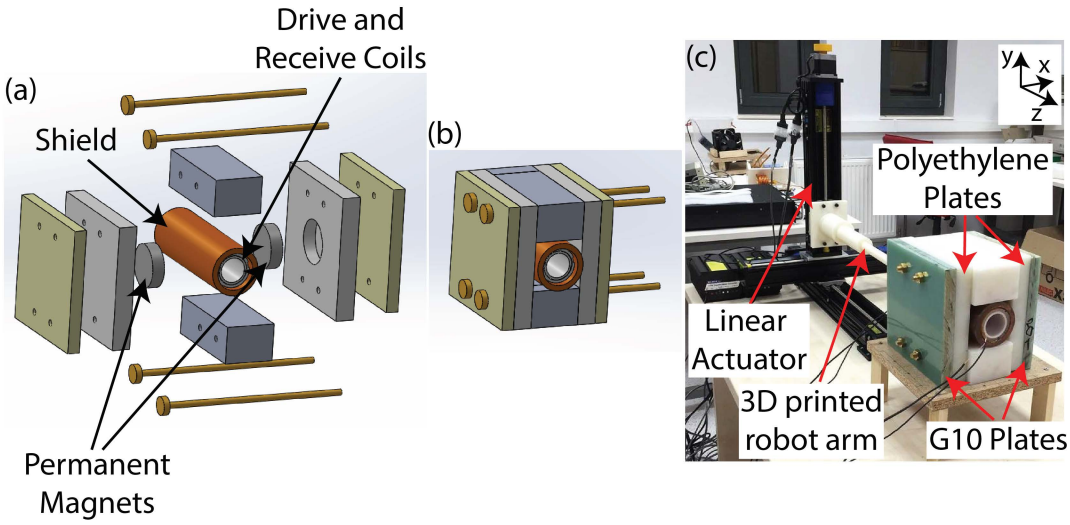

Figure 3.4: (a) The Solidworks design of the MPI scanner with the magnets, coils and shield. (b) The completed form of the design with the components mated together. (c) In the developed MPI scanner, the magnets are placed inside of the polyethylene plates and the G10 plates strengthens the overall structure together with the help of non-magnetic brass screws. The imaging phantom is placed in the plastic robot arm, and a linear actuator moves the phantom in the selection field. Copyright © 2017, IEEE.

the shielding surface. Accordingly, the length of the shield is 22 cm, and its inner and outer diameters are 6 cm and 8 cm, respectively. The complete MPI scanner is shown in Figure 3.4.

3.2.5 Signal Flow

The signal flow of the MPI scanner is as follows: The drive field signal is coded in MATLAB environment and sent to a power amplifier (AE Techron 7224) via a data acquisition card (NI-USB 6363). The amplified drive field signal reaches the drive coil by passing through a capacitive circuitry, which has two purposes: To provide maximum power transfer at 9.7 kHz from the power amplifier to the drive coil (i.e., impedance matching), and to low pass filter the high frequency components at the output of the power amplifier as the drive field is desired to be a single-frequency AC field. The received SPION signal is amplified with a low-noise pre-amplifier (SRS, SR-560) and recorded with the same data acquisition card with a sampling frequency

of 2 MS/s. To calibrate the drive field amplitude, a current probe (PEM, LFR 06/6/300) is used to measure the current through the drive coil. The overall signal flow for this MPI scanner is shown in Figure 3.5.

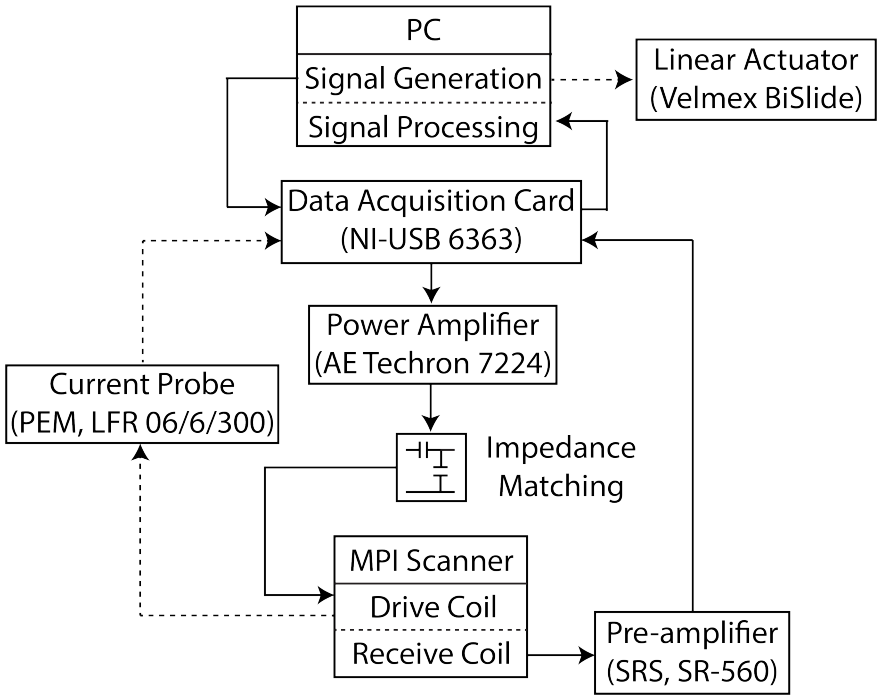

Figure 3.5: The overall signal flow for the MPI scanner. The straight lines show the main signal flow, and the dashed lines show the control of equipment used for the field calibration and the motion of the object. Copyright © 2017, IEEE.

3.2.6 Image Reconstruction

To scan the entire object at once, it is necessary to create a high-amplitude drive field, which is challenging due to the associated high current requirements. Hence, the field-of-view (FOV) must be divided into partial lengths called partial FOVs, each scanned with lower drive field amplitudes. These partial FOVs are combined by first compensating for the loss of the fundamental harmonic due to direct-feedthrough filtering, and then stitching them together [14]. The partial FOV length, W, can be expressed as follows [14, 129, 130, 147]:

$$W = \frac{2H_{peak}}{G} \tag{3.2}$$

Here, H_{peak} is the drive field peak amplitude, and G is the gradient of the selection field along the drive field direction.

3.3 Results

The simulated selection field along the z-direction and its measurement using a gaussmeter are shown in Figure 3.6. The selection field gradient was calculated by taking the derivative of the selection field along the z-direction (i.e., down the bore of the scanner). At the center of the MPI scanner indicated with dashed lines in Figure 3.6(a), the selection field gradient was calculated as 2.4 T/m/μ_0 as shown in Figure 3.6(b). Because of the symmetry of the magnet configuration, the gradient in the y-direction must also be the same, although it was not explicitly measured here. Due to Maxwell's law, the gradient in the x-direction, on the other hand, must be twice as high when compared to the z- and y-directions. Therefore, the gradient in the x-direction can be computed as 4.8 T/m/μ_0 due to anisotropic field gradient [130].

An example image from the constructed MPI scanner with a 4.8 T/m/μ_0 selection field gradient is shown in Figure 3.7. The imaging phantom was prepared with two commercially available SPIONs, namely Nanomag-MIP (Micromod GmbH, Germany) and Vivotrax (Magnetic Insight, CA, USA). The drive field amplitude and frequency were 15 mT/μ_0 and 9.7 kHz, respectively. The overall FOV was 8 mm $\times$ 65 mm in the x-z plane. The FOV of 65 mm along the z-direction was divided into 69 partial FOVs each with a length of 8.3 mm and an overlap percentage of 90%.

3.4 Discussion and Conclusion

MPI is a relatively new biomedical imaging modality. The constructed scanner described in this chapter is also the first MPI scanner designed and developed in Turkey. The MPI image is affected by several parameters such as the selection field gradient,

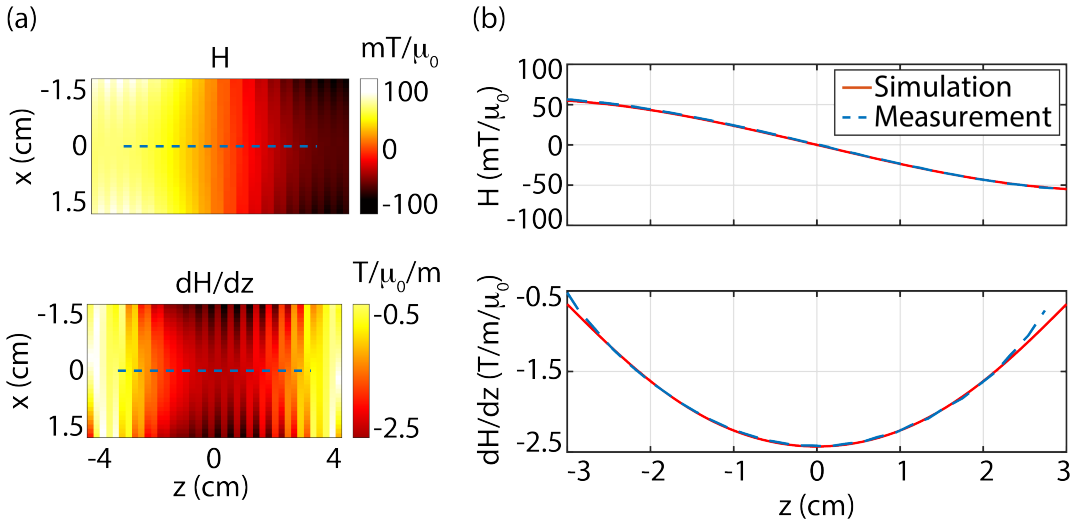

Figure 3.6: (a) The measurement results of the selection field along the z-direction and its gradient (i.e., $G = dH/dz$) using a gaussmeter. (b) The simulation and measurement results are in agreement at the centerline of the magnets indicated by the dashed lines in (a), and the selection field gradient at the center of the MPI scanner was calculated as 2.4 T/m/μ_0. Copyright © 2017, IEEE.

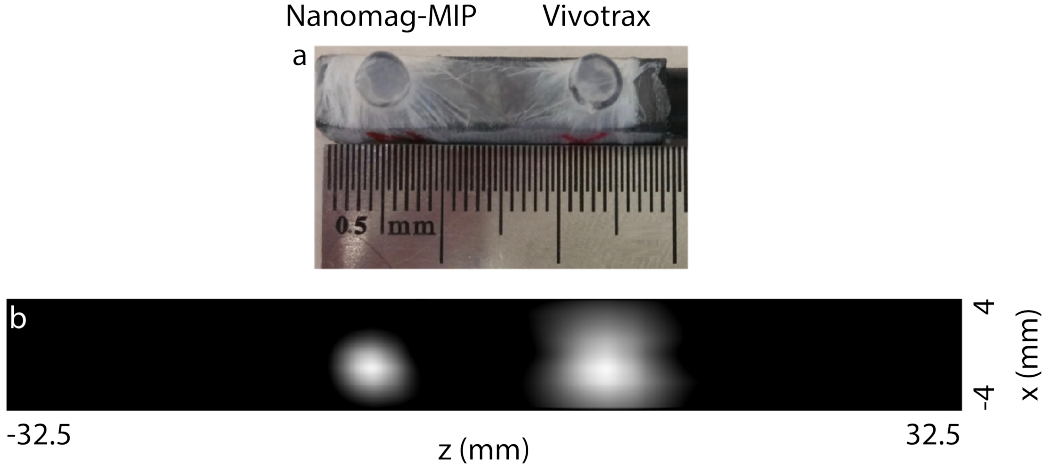

Figure 3.7: (a) The imaging phantom was prepared with two commercially available SPIONs, namely Nanomag-MIP and Vivotrax. (b) 2D MPI image of the imaging phantom was acquired using the in-house MPI scanner at the drive field amplitude and frequency of 15 mT/μ_0 and 9.7 kHz, respectively. The effect of SPION type on the spatial resolution in MPI is clearly visible in this image.

the drive field amplitude and frequency, the SPION type, and the FFP scanning trajectory. Therefore, the selection of the parameters and the hardware components of an MPI scanner mainly depend on the requirements of the targeted application. The free imaging bore of the in-house MPI scanner in x-y direction is 1.9 cm (there is no limit in the z-direction, along the bore). When a robot arm is used to move the imaging phantom across the FFP, the maximum FOV along the radial direction falls down to approximately 1 cm (depending on the size of the phantom). Although the diameter of this MPI scanner is not wide enough for small animal imaging experiments, it can be successfully used for proof-of-concept experiments to demonstrate novel MPI techniques, such as the ones presented in the following chapters of this thesis.

The application areas of MPI are rapidly growing. For example, non-invasive viscosity mapping cannot be achieved with current biomedical imaging modalities, for which MPI shows a great potential. The imaging experiments for viscosity mapping in the following chapters are performed with this developed MPI scanner.

Chapter 4

Relaxation-Based Color MPI for Viscosity Mapping

This chapter is reproduced from the following publications, with the permission of AIP Publishing:

- M. Utkur, Y. Muslu, and E. U. Saritas , "Relaxation-based color magnetic particle imaging for viscosity mapping", Applied Physics Letters 115, 152403 (2019) DOI: 10.1063/1.5110475

4.1 Introduction

The potential applications of MPI have recently been broadened by the introduction of "color" MPI techniques that can distinguish different SPIONs type and/or environments by exploiting the relaxation behavior of SPIONs. One of the important applications of color MPI techniques is viscosity mapping. Certain diseases, such as atherosclerosis [62] and cancer [61, 63], are known to result in increased levels of cellular viscosity. These diseases can potentially be probed with MPI through measuring viscosity of the tissue where the SPIONs are located in.

This chapter demonstrates the imaging results of relaxation-based color MPI for viscosity mapping. The color MPI experiments are based on TAURUS technique [60, 142]. Comparing the imaging results at three different drive field frequencies show that around 10 kHz provide one-to-one mapping between the estimated time constant and viscosity for multi-core cluster SPION of Nanomag-MIP. The 2D color MPI results are presented that differentiate different viscosity levels in the biologically relevant range of up to 5 mPa·s.

4.2 Method

4.2.1 Sample Preparation

An imaging phantom that contained SPION samples at 5 different viscosity levels were prepared using varying ratios of water/glycerol mixtures, as shown in Figure 4.1(a). Each sample was prepared in a capillary tube with 2 mm diameter, had a total volume of 20 μL, and contained 5 μL of undiluted Nanomag-MIP SPIONs (plain, c(Fe) = 89 mmol Fe/L). The resulting samples had viscosity levels ranging between 0.89 mPa·s and 5.04 mPa·s, covering biologically relevant viscosity levels [148, 149]. Table 4.1 lists the details of each SPION sample.

4.2.2 Experimental Setup and Procedures

The imaging experiments were performed on the in-house MPI scanner shown in Chapter 3. The default operating frequency of this in-house MPI scanner was 9.7 kHz [150]. In addition, frequencies around 25 kHz are widely used in MPI literature [13, 151, 32]. Moreover, the MPS measurements in Chapter 2.4.1.1 (Figure 2.6) suggested that lower frequencies around 1 kHz may be promising for probing viscosity [60]. Therefore, using capacitive L-section circuits, the drive coil was impedance matched to the power amplifier (AE Techron 7224) at three different frequencies: 1.1 kHz, 9.7 kHz, and 26.3 kHz. The drive coil was air-cooled to prevent heating

Table 4.1: The contents and viscosity levels at 25°C for the SPION samples. Each sample started from 5 μL of undiluted Nanomag-MIP SPIONs suspended in water, and had a final volume of 20 μL. The table lists the added glycerol and water volumes, and the final glycerol percentage by volume.

#	Viscosity (mPa·s)	Glycerol (μL)	Water (μL)	Glycerol %
1	0.89	0	15	0
2	1.54	4	11	20
3	2.16	6	9	30
4	3.97	9	6	45
5	5.04	10	5	50

of the scanner bore and SPION samples. The scanner bore had an axial diameter of 1 cm in x-y plane, with flexible length along the z-direction. The imaging phantom had a length of 14.5 cm in z-direction, which cannot be scanned with a single drive field amplitude due to high current requirements as discussed in Chapter 3.2.6. Therefore, the drive field was applied along the z-direction with amplitudes varying between 10 mT/μ_0 and 25 mT/μ_0, corresponding to partial FOV (pFOV) sizes of 4.2 mm and 10.4 mm. The drive field amplitude was calibrated with a current probe (LFR 06/6/300) promptly before each measurement. For all the 1D and 2D imaging experiments, the phantom was mechanically moved to the center of each pFOV using a linear actuator (Velmex BiSlide), with 85% overlap between neighboring pFOVs. For each pFOV, the signal was filtered and processed as previously described [142]. MPI images were then reconstructed using a signal-to-noise ratio (SNR) optimized x-space reconstruction [147] with DC recovery algorithm [14]. The relaxation time constant maps (τ maps) were directly estimated from the time-domain signals for each pFOV, using the aforementioned TAURUS technique.

4.3 Results

4.3.1 1D Imaging Experiment Results

First, six different 1D imaging experiments (at 3 different drive field frequencies and 2 different drive field amplitudes) were conducted to determine the optimal drive field parameters for relaxation-based viscosity mapping. The drive field amplitudes tested were 10 mT/μ_0 and 15 mT/μ_0 at 1.1 kHz and 9.7 kHz, and 10 mT/μ_0 and 14 mT/μ_0 at 26.3 kHz (the latter restricted by hardware limitations). Experiments were first performed with the samples ordered randomly (results not shown), and then with the samples ordered in increasing viscosity levels. Both cases yielded matching results, ensuring that there was no position-induced bias. The resulting 1D MPI images and τ maps were replicated along the vertical direction for display purposes, as shown in Figure 4.2(a) and (b). Note that for simplicity of labeling, the results at 26.3 kHz and 14 mT/μ_0 are grouped under 15 mT/μ_0 results.

As seen in Figure 4.2(b), τ maps at 26.3 kHz appear flat. Hence, although frequencies around 25 kHz are widely popular in MPI, this high frequency range is not favorable for probing viscosity. On the other hand, τ maps at 1.1 kHz and 9.7 kHz display a variety of colors, indicating a viscosity-sensitive contrast capability. Furthermore, the MPI images at these lower frequencies display better resolution, which is consistent with the literature [152, 153]. Next, mean τ values were computed from the corresponding regions-of-interest (ROIs) in τ maps, and plotted as a function of viscosity in Figure 4.2(c). Accordingly, there is a considerable differentiation with more than 40% change in τ values with respect to viscosity at 9.7 kHz. At 1.1 kHz and 26.3 kHz, on the other hand, the curves are either non-monotonic or remain approximately flat.

The trends observed in Figure 4.2 are consistent with the previous experimental work in a MPS setup [60], with one important difference: In the MPS setup, τ vs. viscosity curves displayed a non-monotonic trend at lower drive field frequencies of up to 550 Hz, switched to a monotonic trend at 1.1 kHz, and finally became flat at 10.8 kHz. In this work, with the added selection field of an MPI scanner, the switch from non-monotonic to monotonic trend occurs at a higher frequency range. A side-by-side

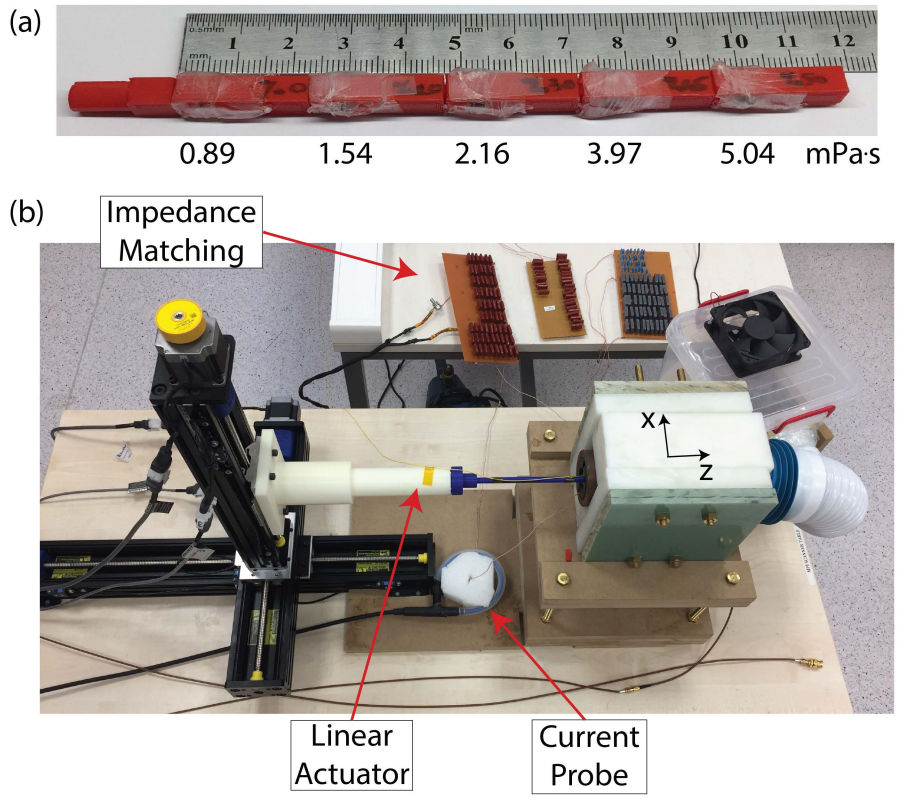

Figure 4.1: (a) SPION samples at 5 different viscosity levels ranging between 0.89 mPa·s and 5.04 mPa·s were placed in the imaging phantom for color MPI experiments. (b) The drive coil in this MPI scanner was impedance matched at three different frequencies: 1.1 kHz, 9.7 kHz, and 26.3 kHz. The imaging phantom was moved in the x-z plane using a linear actuator. A current probe was used to calibrate the drive field amplitude.

comparison of normalized τ values from MPS and MPI experiments are shown in Figure 4.3, color matched to highlight similar trends at different frequencies. The trend seen at 550 Hz in the MPS experiments is similar to that at 1.1 kHz in the MPI experiments. Likewise, 1.1 kHz and 10.8 kHz in MPS experiments display similar trends as in 9.7 kHz and 26.3 kHz in MPI experiments, respectively. Importantly, for MPI experiments, the monotonic τ vs. viscosity curve at 9.7 kHz indicates that this operating frequency is highly promising for one-to-one mapping of viscosity from a measured τ value.

To further investigate the viscosity mapping capability at 9.7 kHz, 1D imaging experiments were performed at four different drive field amplitudes between 10 mT/μ_0

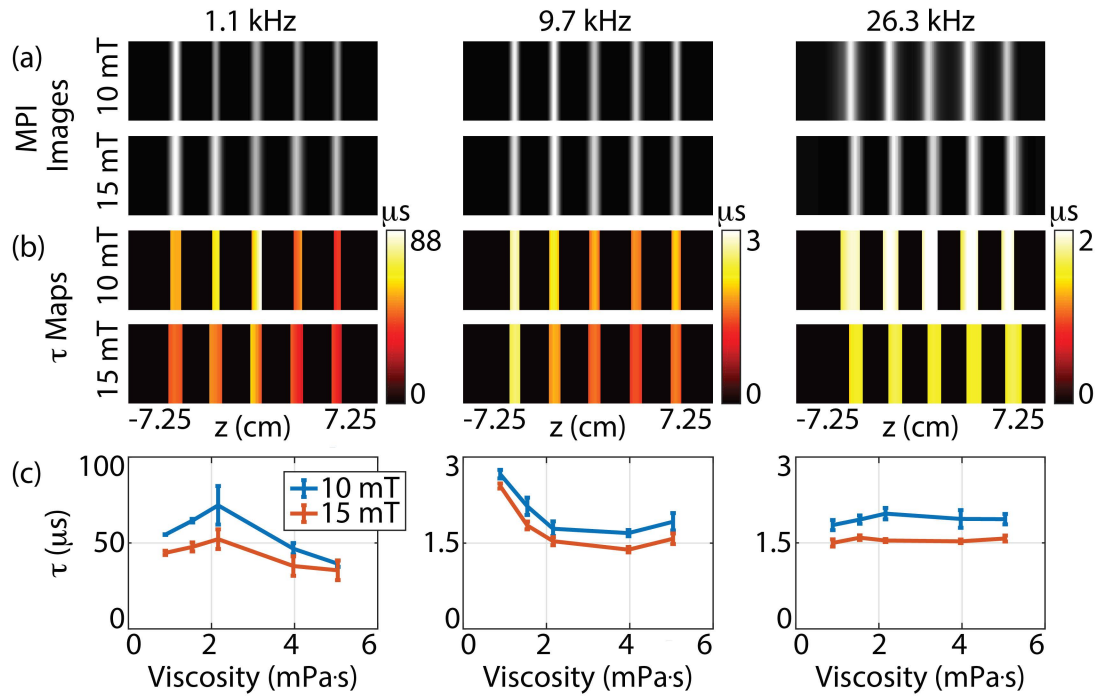

Figure 4.2: 1D color MPI results at 3 different drive field frequencies and 2 different drive field amplitudes, for the phantom shown in Figure 4.1(a) where the samples were ordered in increasing viscosity levels between 0.89 mPa·s and 5.04 mPa·s. (a) 1D MPI images and (b) 1D relaxation (τ) maps were replicated in the vertical direction for display purposes. (c) τ vs. viscosity curves were extracted from the τ maps. The predominantly monotonic trend at 9.7 kHz indicates that this drive field frequency is well-suited for one-to-one viscosity mapping. The error bars denote the standard deviations computed from corresponding ROIs in τ maps for each sample.

and 25 mT/μ_0. The corresponding MPI images, τ maps, and τ vs. viscosity curves are displayed in Figure 4.4. At this frequency, τ values vary by more than 50% in the tested viscosity range (i.e., >10%/mPa/s between 0.89-5.04 mPa·s), which is a highly desirable feature for mapping purposes. Note that a superior monotonicity is reached at 25 mT/μ_0 drive field amplitude. Furthermore, given that the MPI signal increases linearly with the drive field amplitude[153], the increased SNR at 25 mT/μ_0 results in reduced deviation in τ estimations (see error bars in Figure 4.4(c)).

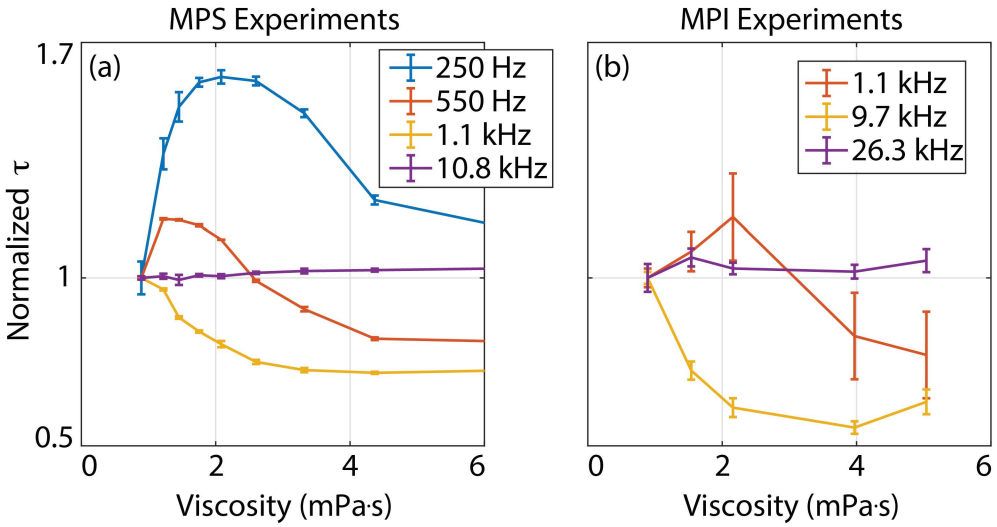

Figure 4.3: Comparison of τ vs. viscosity curves for (a) MPS experiments (re-plotted from Ref.([60]) and (b) color MPI experiments, performed at different drive field frequencies at a 15 mT/μ_0 amplitude. The results are color matched to highlight similar trends. A monotonic τ vs. viscosity curve is observed at 1.1 kHz in MPS experiments, whereas a similar trend is achieved at 9.7 kHz with the additional selection field of the MPI scanner.

4.3.2 2D Imaging Experiment Results

Finally, a 2D color MPI demonstration was performed at the optimal drive field parameters: 9.7 kHz and 25 mT/μ_0. The phantom in Figure 4.5(a) was scanned with a FOV of 0.8 cm $\times$ 14.5 cm in x- and z- direction, respectively. This FOV was rastered along the z-direction as 9 evenly-spaced lines, each made up of 39 overlapping pFOVs. The resulting 2D MPI image and τ map, as well as their color overlay, are shown in Figures 4.5(b) - (d). The SPION samples at different viscosity levels are easily distinguishable in the τ map, confirming the suitability of these drive field parameters for one-to-one viscosity mapping.

In MPI, the properties of the SPIONs such as their size, dispersity, and anisotropy have a large impact on their signal [151]. These factors affect the performance of the SPIONs not just in MPI, but also in other modalities such as magnetic resonance imaging (MRI) or magnetic fluid hyperthermia (MFH) [154, 155]. Similarly, the optimal drive field parameters may depend on the SPION type. In a previous work, τ vs. viscosity trends were compared for two multi-core SPIONs, Nanomag-MIP and

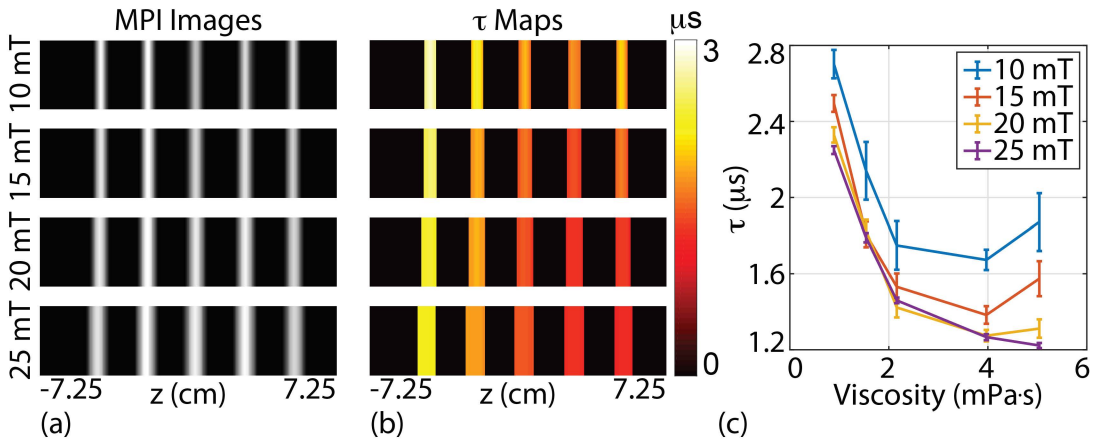

Figure 4.4: 1D color MPI results at 4 different drive field amplitudes at 9.7 kHz, for the phantom in Figure 4.3(a) where samples are ordered in increasing viscosity levels. (a) 1D MPI images and (b) τ maps, replicated in the vertical direction for display purposes. (c) τ vs. viscosity curves indicate that a higher drive field amplitude of 25 mT/μ_0 yields superior monotonicity. The error bars denote the standard deviations computed from the corresponding ROIs in τ maps for each sample.

VivoTrax, where the latter has the same chemical structure as Resovist. It is observed that Vivotrax displayed similar global trends as Nanomag-MIP, but at higher drive field frequencies [60]. Therefore, the optimal drive field parameters, particularly the drive field frequency, may need to be tuned for a given SPIO type.

4.4 Discussion

Brownian and Néel relaxation time constants of SPIONs are normally calculated using zero-field formulas, which are not valid for the sinusoidal drive field in MPI [156]. In τ vs. viscosity curves at lower drive field frequencies/amplitudes, the estimated τ values initially increase with increasing viscosity [60], seemingly obeying Brownian relaxation dynamics. At higher frequencies/amplitudes/viscosities, however, this initial trend can no longer be observed. The reason behind this phenomenon may stem from the SPION magnetization not having the sufficient time to reach its steady-state value under these "more demanding" cases. Hence, one can no longer observe the expected monotonic increase with increasing viscosity, causing a different trend to

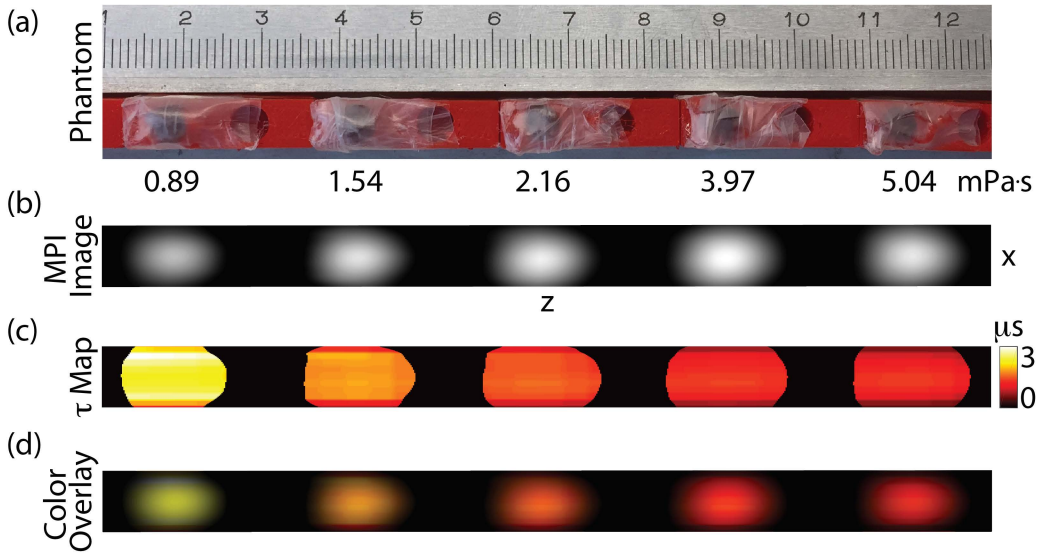

Figure 4.5: 2D color MPI demonstration at the optimal drive field parameters: 9.7 kHz and 25 mT/μ_0. (a) The imaging phantom with 5 different samples ordered in increasing viscosity levels ranging between 0.89 mPa·s and 5.04 mPa·s. (b) 2D MPI image, (c) 2D τ map, and (d) their color overlay. Different viscosity levels are easily distinguishable in the τ map, as well as the color overlay. The phantom was scanned with a FOV of 0.8 cm $\times$ 14.5 cm in x- and z-directions, respectively. The displayed FOV is 0.8 cm$\times$ 11.5 cm.

emerge. A similar phenomenon was also described in a recent work, where it was shown that the magnetization could not reach its steady-state value (i.e., the value dictated by Langevin physics) in the case of square-wave pulsed excitation with higher frequencies/amplitudes [157].

The above-cited work has also shown that SPIONs farther from the FFP are characterized with faster relaxation when compared to the SPIONs closer to the FFP [157]. Likewise, preliminary experiments on the MPS setup also demonstrated that τ values can be reduced in the presence of an additional DC field (results not shown). Importantly, the change in τ values can be at different rates for different viscosity levels, which in turn can change the overall τ vs. viscosity trend. Hence, under the static selection field of an MPI scanner, the observed τ values as well as the τ vs. viscosity trend can change when compared to those in an MPS setup. Understanding the physical reasons behind the latter affect requires future experiments and analysis.

Previous work has shown that SNR scales almost linearly with the product of the

drive field frequency and amplitude [153]. Therefore, even if a monotonic trend could be achieved at a lower drive field frequency/amplitude than the tested range, the SNR of the images/maps would suffer considerably. For example, 1.1 kHz and 5 mT/μ_0 would yield approximately 44 times lower SNR than at 9.7 kHz and 25 mT/μ_0, which is a massive difference. At very high frequencies/amplitudes, on the other hand, the τ vs. viscosity trends flatten out [60]. Hence, the goal in this work was to operate at as high a frequency/amplitude as possible, while attaining a one-to-one mapping between τ and viscosity in the biologically relevant range.

Even when operating at high drive field frequency/amplitude, SNR can be low in *in vivo* settings. A noise robustness of the TAURUS technique was previously performed [142], showing that even at a very low SNR value of 2, the relaxation time constant can be estimated with a standard deviation that is less than 0.4% of the drive field period (around 0.4 μs at 9.7 kHz). For SNR values greater than 15, the standard deviations rapidly decrease to less than 0.05% of the drive field period (around 0.05 μs at 9.7 kHz). The specific iron amount corresponding to a given SNR level depends on the scanner geometry and SPION type, as well as the scanning parameters [21]. Considering that MPI features a state-of-the-art detection limit in the order of 5-100 ng Fe [16, 49, 158], with a theoretical picogram sensitivity capability [21, 159], the SNR robustness of the TAURUS technique makes it an excellent candidate for *in vivo* viscosity mapping with MPI.

Here, TAURUS technique has been demonstrated using multi-core cluster SPIONs. In *in vivo* settings, size selective uptake may take place during the internalization of the SPIONs into the tissue/cells, which may change the MPI response for SPIONs that contain different-sized cores. To avoid such effects, single-core SPIONs may be preferred. Investigating such *in vivo* challenges and potential solutions for the proposed technique remains a future work.

4.5 Conclusion

To summarize, this chapter demonstrates the viscosity mapping capability of MPI for functional imaging applications. With an in-house MPI scanner, it is shown that a one-to-one mapping between the relaxation time constant and viscosity can be achieved at drive field parameters around 10 kHz and 25 mT/μ_0 using multi-core cluster Nanomag-MIP SPION. These results present relaxation-based color MPI experiments distinguishing the biologically relevant viscosity range.

Chapter 5

Simultaneous Temperature and Viscosity Mapping for MPI

This chapter is based on the following manuscript which was submitted to *Medical Physics*:

- M. Utkur and E. U. Saritas, "Simultaneous Temperature and Viscosity Mapping for Magnetic Particle Imaging", Medical Physics (2021)

5.1 Introduction

Temperature mapping, or thermometry, presents itself as one of the important application areas of MPI, especially considering the fact that SPIONs are also used in thermal therapy applications such as MFH. When subjected to relatively high-frequency AC magnetic fields (e.g., 300-400 kHz), SPIONs become very efficient heat sources that can be used to target and heat up tumor tissue without any depth limitations and achieve immunogenicity [28, 89]. The heat generation property of SPIONs is based on the same relaxation mechanisms that give MPI its functional imaging capability. Moreover, the hardware of MPI and MFH are compatible, enabling hybrid MPI-MFH

systems to be constructed for image-guided localized heat therapy [87, 160]. By positioning the field-free-region of an MPI scanner over the tumor region, MPI can equip MFH with localized heating capability [90, 161]. In addition, the MPI image can be utilized to predict the temperature rise prior to MFH therapy [162, 90], or to provide real-time temperature feedback through temperature mapping during MFH therapy (e.g., via a short break of imaging). The current thermal ablation studies for prostate and breast cancers utilize integrated magnetic resonance imaging (MRI) and high intensity focused ultrasound (HIFU) systems, where MRI non-invasively monitors the temperature and HIFU delivers thermal energy to the tumor tissue [73, 75]. Some of the major drawbacks of this approach include extremely long treatment times reaching up to hours, and technical limitations in HIFU beam conformation that may result in inhomogeneous thermal dose or damage to the surrounding healthy tissue [77]. Here, a hybrid MPI-MFH system emerges as a very promising alternative for thermal ablation treatment of cancer, as MFH is depth independent and the imaging duration of MPI is in the range of seconds to minutes.

To date, several groups have proposed different methods to estimate temperature in MPI. Some studies worked with the spectral information of the SPION response using a magnetic particle spectrometer (MPS) setup, where the ratios of harmonics were related to the temperature change [163, 164, 165, 166]. Other studies in an MPI scanner utilized a system function approach, where the frequency response of SPIONs at different temperatures were acquired during a calibration procedure, and the temperatures during imaging were mapped by solving a linear system of equations [167, 168, 169]. In contrast to the aforementioned spectral methods, TAURUS works with the time-domain SPION response and estimates a relaxation time constant that recovers the underlying mirror symmetric response [60]. A powerful feature of this technique is that it can be directly applied to both MPS and MPI signal responses, since the underlying mirror symmetry assumption is valid independent of the spatial distribution of SPIONs [142, 143]. The viscosity mapping capability of TAURUS was already shown in Chapter 4, and the optimal drive field parameters was obtained using commercially available multi-core SPIONs [143].

An important consideration for temperature mapping with MPI is that the viscosity of the environment also needs to be accounted for, as these two parameters are bound

to have confounding effects on the MPI signal. Different tissues may show varying degrees of change in their viscosity levels as a function of temperature [170], or different initial viscosity levels may lead to different trends on the relaxation time constant as a function of temperature. These factors can in turn lead to erroneous temperature estimations. Therefore, to achieve accurate temperature estimations, either the MPI signal needs to be desensitized to the viscosity effect, or viscosity and temperature need to be estimated simultaneously. In this chapter, the effects of temperature on TAURUS were experimentally analyzed while taking the viscosity level into account to enable simultaneous mapping of these two parameters. With extensive experiments, the therapeutically applicable temperature range (25-45°C) and the biologically relevant viscosity range (<4 mPa·s) was covered, and utilize 60 different operating points with drive field amplitudes ranging between 5-25 mT/μ_0 and frequencies ranging between 1-7 kHz. To enable this experimental procedure, an in-house arbitrary-waveform MPS setup with temperature-controlled heating capability was developed, which can rapidly acquire a wide range of operating points grouped together with respect to their signal levels to ensure gain maximization. The results show that the temperature sensitivity of TAURUS slowly varies in these drive field settings and reaches a maximum value of 1.19%/°C, whereas viscosity sensitivity is mainly concentrated at lower frequencies around 1 kHz with a maximum value of 12.2%/mPa/s. Furthermore, strategies for simultaneous mapping of temperature and viscosity were proposed using two different drive field settings, or temperature mapping alone at frequencies where viscosity sensitivity is minimized.

5.2 Theory

Using Faraday's law of induction, the received signal in MPI can be expressed as follows [129, 118]:

$$\begin{aligned} s_{received}(t) &= -\frac{d\phi(t)}{dt} = -\mu_0 \int_V \mathbf{B_1}(\mathbf{r}) \cdot \frac{\partial \mathbf{M}(\mathbf{r},t)}{\partial t}\, dV \\ &= -\mu_0 \int_V \mathbf{B_1}(\mathbf{r}) \cdot c(\mathbf{r}) \frac{\partial \overline{\mathbf{m}}(\mathbf{H}(\mathbf{r},t))}{\partial t}\, dV \end{aligned} \tag{5.1}$$

Here, $\phi(t)$ is the magnetic flux, $\mathbf{B_1}(\mathbf{r})$ is the position-dependent receive coil sensitivity, $\mathbf{H}(\mathbf{r},t)$ is the applied field, and '$\cdot$' indicates vector dot product. In addition, $\mathbf{M}(\mathbf{r},t)$ is the SPION magnetization, which is equal to the multiplication of SPION concentration, $c(\mathbf{r})$, and the average magnetic dipole moment, $\overline{\mathbf{m}}(\mathbf{H})$.

In the case of a typical MPS setup, it can be assumed that the applied field over the sample is homogeneous in space and unidirectional (e.g., only along the z-direction), the receive coil sensitivity in that direction is also homogeneous, and the SPION concentration is uniform within the sample. Under these assumptions, Equation 5.1 can be rewritten as:

$$s_{received}(t) = -\mu_0 \int_V B_1 c \frac{d\overline{m}(H(t))}{dt} dV = -\mu_0 B_1 c V_S \frac{d\overline{m}(H(t))}{dt} \tag{5.2}$$

Here, V_S is the sample volume, and the multiplication of c and V_S is equal to the total iron mass within the sample.

Assuming that the SPIONs follow Langevin physics with an adiabatic approximation that their dipole moments immediately align with the applied field, $s_{adiabatic}$(t) can be written as:

$$s_{adiabatic}(t) = -\mu_0 B_1 c V_S m \frac{d\mathscr{L}(kH(t))}{dt} = -\alpha \dot{\mathscr{L}}(kH(t))\dot{H}(t) \tag{5.3}$$

where

$$\alpha = \mu_0 B_1 c V_S m k \tag{5.4}$$

Here, m is the magnetic moment of a single SPION, $\mathscr{L}(\cdot)$ is the Langevin function and $\dot{\mathscr{L}}(\cdot)$ is its derivative, and k is a parameter that depends on m and SPION temperature.

In reality, the adiabatic approximation is not valid for rapidly time-varying applied fields, where the alignment of the magnetic moment lags behind due to the relaxation mechanism of SPIONs through a combination of an external physical rotation (i.e., Brownian relaxation) and an internal rotation (i.e., Néel relaxation) [51, 52]. The governing relations for these two relaxation mechanisms for the "zero-field" case (i.e., when a DC field is abrutly set to zero) are already given in Equations 2.18 and 2.19.

As seen in these equations, the relaxation time constants are dependent on the environmental conditions, namely temperature and viscosity. This feature makes the

relaxation mechanism particularly important for functional imaging purposes in MPI. However, the zero-field condition does not directly apply in MPI, since a continuous sinusoidal drive field is utilized together with simultaneous signal reception. While the theoretical aspect of the relaxation mechanisms under an oscillating magnetic field is still incomplete [119], the "effective" relaxation process in the case of a sinusoidal drive field was previously modeled as a first-order Debye process, where the relaxation behavior causes the time-domain SPION response to simultaneously get delayed in time and lose signal amplitude [141, 153]. The relationship between the received signal and ideal signal is already expressed in Equation 2.30.

As described previously, ideal signal has mirror symmetric positive and negative half cycles, but that mirror symmetry is broken due to the relaxation effects on the received signal. TAURUS directly estimates τ as shown in Equation 2.31. Note that this estimated relaxation time constant, τ is also dependent on both temperature and viscosity [60], since τ corresponds to an effective combination of τ_B and τ_N under a sinusoidal drive field. Furthermore, viscosity is known to decrease with temperature, which causes these two environmental parameters to have confounding effects on the SPION response. In the following sections, the effects of temperature and viscosity on τ are analyzed under a wide range of drive field settings using an in-house arbitrary-waveform MPS setup.

5.3 Materials and Methods

5.3.1 Sample Preparation

A total of 15 samples with glycerol volume percentages ranging between 0% and 55.1% were prepared in 0.2 mL PCR tubes, to achieve targeted biologically relevant viscosity levels at different temperatures. Each sample had a total volume of 150 μL and contained 60 μL of undiluted Perimag nanoparticles (Micromod GmbH, Germany) at 303.6 mM initial concentration (i.e., each sample had 1 mg Fe). For the remaining 90 μL, varying volumes of double-distilled water and glycerol were added to achieve

the desired glycerol percentages as listed in Table. 5.1. The viscosity levels at 30°C and 40°C were taken directly from the literature, and the viscosity levels at 25°C, 35°C, and 45°C were computed via linear interpolation [171]. As seen in Table. 5.1, at fixed temperature, viscosity increases with increasing glycerol percentage. On the other hand, the viscosity of a sample at a fixed glycerol percentage decreases with increasing temperature. This physical phenomenon enabled the experiments to be designed such that 4 different target viscosity levels (0.9 mPa·s, 1.8 mPa·s, 2.7 mPa·s, and 3.6 mPa·s) were achieved at 5 different temperatures (25°C, 30°C, 35°C, 40°C, and 45°C), as highlighted with different colors in Table. 5.1.

Table 5.1: Glycerol volume percentages and viscosity levels at 5 different temperatures for the 15 SPION samples used in this work. Each sample contained 60 μL of undiluted Perimag nanoparticles. The colors highlight 4 different target viscosity levels achieved at 5 different temperatures.

Glycerol %	Viscosity (mPa·s)				
	25°C	30°C	35°C	40°C	45°C
0.0	0.9	0.8	0.7	0.7	0.6
4.4	1.0	0.9	0.8	0.7	0.7
8.7	1.1	1.0	0.9	0.8	0.7
13.1	1.3	1.1	1.0	0.9	0.8
16.7	1.4	1.2	1.1	1.0	0.9
23.9	1.8	1.6	1.4	1.2	1.1
28.7	2.1	1.8	1.6	1.4	1.3
31.9	2.4	2.0	1.8	1.6	1.4
35.3	2.7	2.3	2.1	1.8	1.6
39.5	3.2	2.7	2.4	2.0	1.8
42.2	3.6	3.1	2.7	2.3	2.0
46.1	4.4	3.6	3.2	2.7	2.4
49.6	5.0	4.2	3.6	3.1	2.7
52.5	6.1	4.5	4.3	3.6	3.2
55.1	7.1	5.7	4.9	4.1	3.6

5.3.2 Experimental Setup and Procedures

Experiments were performed on an in-house arbitrary-waveform MPS setup (see Figure 5.1). The nanoparticle samples were placed in a temperature-controlled water tube

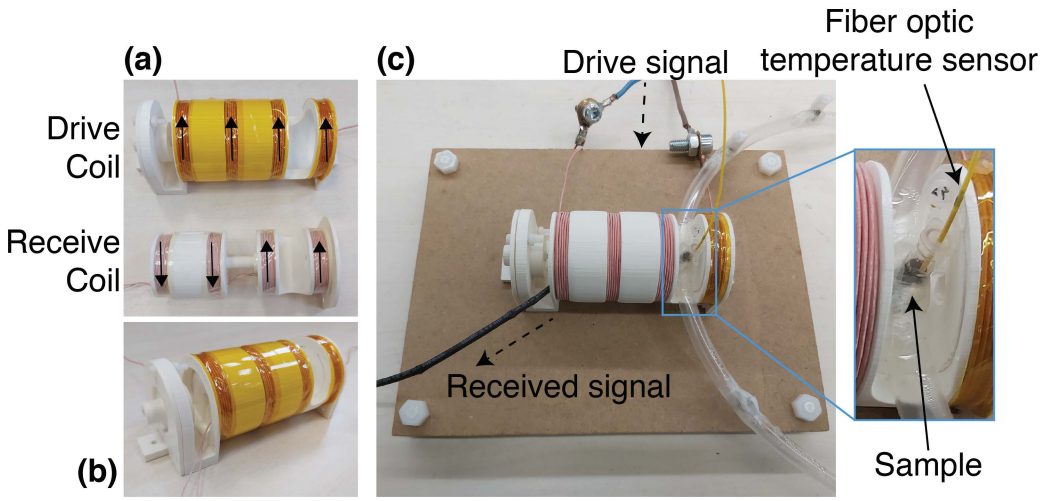

Figure 5.1: In-house arbitrary-waveform MPS setup, designed to enable temperature-controlled heating of the SPION samples. (a) The drive coil consisted of 4 sections and the receive coil was a two-section gradiometer-type coil that mirrors the structure of the drive coil. The arrows show the winding directions. (b) The drive and receive coils were placed co-axially, and the moving sub-parts of the receive coil were adjusted with a screw mechanism to minimize the mutual inductance between the two coils. (c) An overview of the experimental setup. The samples were placed in a temperature-controlled water tube, and the temperature of each sample was monitored with a fiber optic temperature probe. The dashed arrows indicate the direction of signal flow.

during the experiments. To accommodate the placement of this structure into the measurement chamber (see Figure 5.1(c)), a 41.5-mm inner diameter drive coil was designed to consist of 4 sections of equal length separated by 20-mm gaps. Each section had 3 layers of windings with 6 turns per layer, wound using 125-strand 40 AWG Litz wire (MWS Wire Industries). The sensitivity of the drive coil was measured using a gaussmeter (LakeShore, 475 DSP) by applying 1 A of current at frequencies ranging between 1 kHz and 10 kHz. The sensitivity was measured as 0.65 mT/μ_0/A, with a negligible standard deviation of 2 μT/μ_0/A in this frequency range.

As shown in Figure 5.1(a), an 11-mm inner diameter receive coil was designed as a two-section gradiometer-type coil, where each section was further divided into two sub-parts to mirror the structure of the drive coil. These sub-parts were separated by 21.6-mm gaps, and each part contained 15 layers with 9 turns per layer, wound using 125-strand 44 AWG Litz wire (MWS Wire Industries). The two sub-parts where the sample was placed in between were fixed to the drive coil, whereas the other two

sub-parts were attached to a plastic screw to enable fine-tuned adjustment of their position. These moving sub-parts enabled high precision decoupling between the drive and the receive coils, which were placed co-axially as shown in Figure 5.1(b). The sensitivity of the receive coil was measured as 4.1 mT/μ_0/A at 1 kHz and its self-resonance was measured to be above 200 kHz, which is well outside the range of frequencies of interest in this work. The simulated magnetic field maps of the drive and the receive coils of the arbitrary-waveform MPS setup in x-z planes is shown in Figure 5.2(a) and (b). The centerline in the magnetic field maps at x = 0 is also plotted in Figure 5.2(d), where the adjustable position of the receive coil corresponds to the negative portion in this plot.

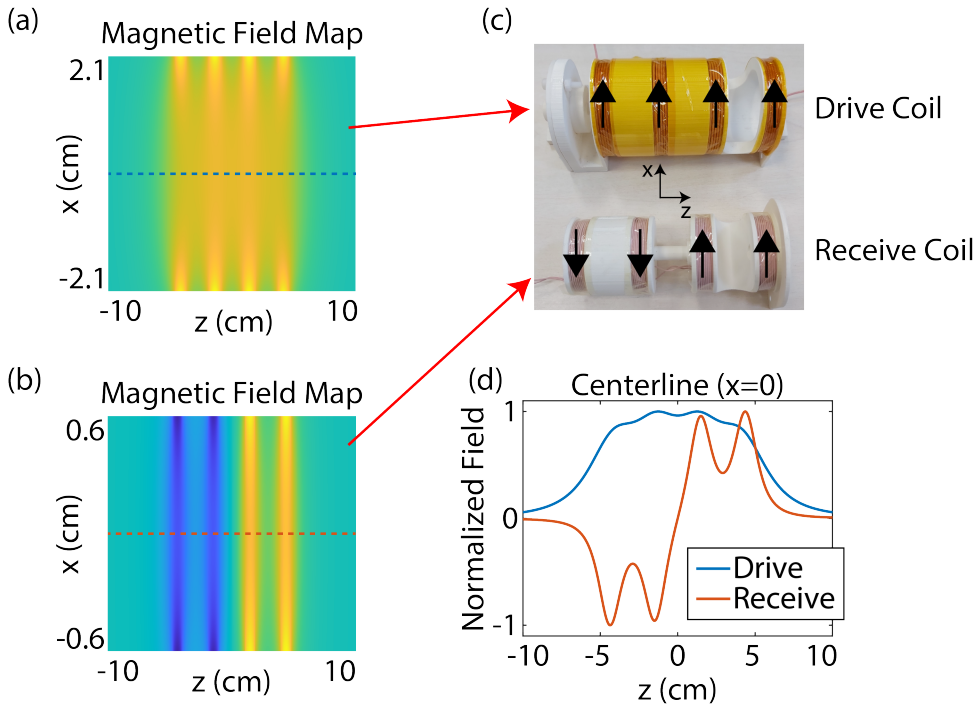

Figure 5.2: The simulated magnetic field maps of the drive coil (a) and receive coil (b) of the arbitrary-waveform MPS setup (c). The centerline of the dashed lines in the magnetic field maps are plotted with respect to the z-direction (d).

The resistance and the inductance of the drive coil were measured with an LCR meter (GW Instek LCR-8100) as 0.29 Ω and 92 μH, respectively, for frequencies lower than 10 kHz. Owing to the low inductance of the drive coil, the need for impedance matching was eliminated so that the drive coil could be directly connected to an AC power amplifier (AE Techron 7224). This arbitrary-waveform MPS characteristic

[172, 173] enabled any drive field signal below 10 kHz to be applied without using additional capacitive circuitry.

The experimental setup was controlled with a fully-automated custom script in MATLAB (Mathworks, Natick, MA). The drive field waveform was sent to the AC power amplifier via a data acquisition card (NI PCI-6115), and the received signal was also digitized using the same card with a sampling rate of 2 MS/s. The PCR tubes that contained the samples were placed vertically in the holes cut out on a water tube, and sealed with hot glue to prevent water leakages. A temperature-controlled water pump was used to circulate hot water inside the water tube, heating up the samples to the desired temperatures via conduction. During the experiments, the temperature of the sample of interest was monitored with a fiber optic temperature probe (Neoptix Reflex-4) placed inside the PCR tube. The drive coil was cooled with cold air to prevent resistive-heating-induced field fluctuations, and its temperature was monitored with a thermal camera (Seek Thermal Reveal Pro). On the receive side, the nanoparticle signal first passed through an analog Butterworth low pass filter (SRS SIM965) with 200 kHz cut-off frequency and 48 dB/octave roll-off, and then amplified with a BJT preamplifier (SRS SIM911).

To investigate the confounding effect of temperature and viscosity on the time constant estimations, drive field parameters that were similar to those in the previous MPS measurements in Chapter 2.4.1.1 (Figure 2.6) were chosen. The samples were tested at seven different drive field frequencies ranging between 1-7 kHz with 1 kHz increments, and nine different drive field amplitudes ranging between 5-25 mT/μ_0 with 2.5 mT/μ_0 increments. Among the resulting 63 operating points, the following 3 operating points could not be utilized due to hardware limitations: (6 kHz, 25 mT/μ_0), (7 kHz, 22.5 mT/μ_0), (7 kHz, 25 mT/μ_0). Since the received signal was picked up inductively, its amplitude is approximately proportional with both the drive field amplitude and frequency (see Equation 5.3). Therefore, the remaining 60 operating points were divided into four groups with comparable signal amplitudes, as shown in Figure 5.3(a). Within each group, the peak signal amplitude varied by at most three-fold among different operating points. The drive field waveform at each operating point contained 40 periods followed by a gap of the same duration to avoid any transient effects (see Figure 5.3(b)). A calibration stage was performed prior to the measurement

stage in which the drive amplitudes within a group were calibrated with a Rogowski current probe (LFR 06/6/300) using the coil sensitivity data measured earlier. Then, a single gain value for that group was selected as the maximum gain that does not overload the preamplifier. In the measurement stage, two consecutive acquisitions were performed: an empty-chamber baseline acquisition and an acquisition with the sample. In each case, the mean of 4 acquisitions were recorded to increase the SNR. Furthermore, all measurements were repeated three times by randomizing the ordering of the operating points within each group, with the goal of eliminating potential ordering related biases in the results. Overall, a total of 3600 measurements were performed (i.e., 4 viscosity levels, 5 temperatures, 60 operating points, and 3 repetitions).

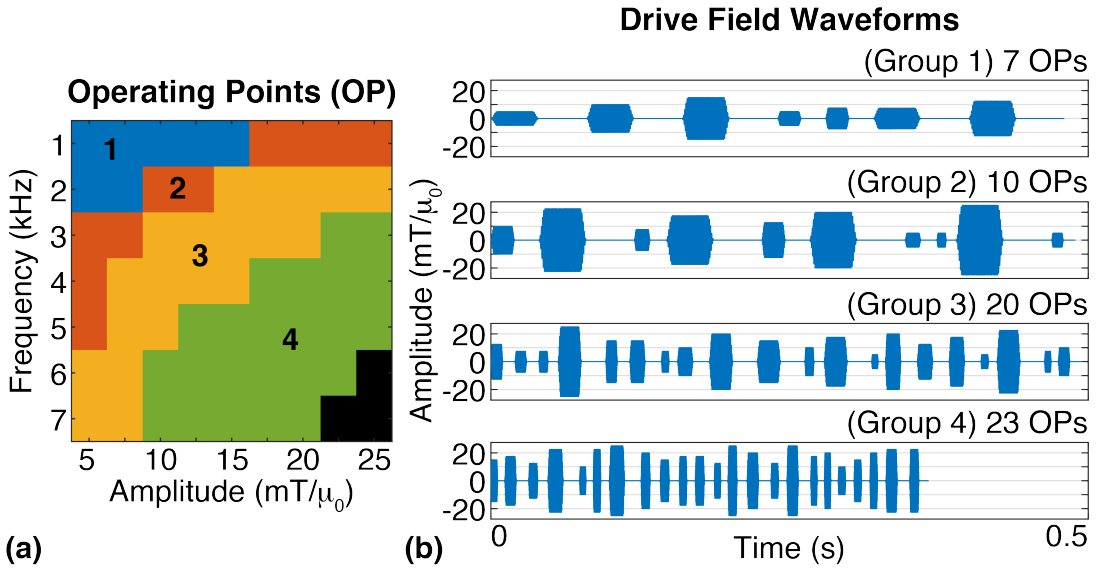

Figure 5.3: Operating points and the corresponding drive field waveforms. (a) 60 different operating points were divided into four groups with comparable signal amplitudes, as enumerated and marked with colors. The grouping ensured that the peak signal amplitude within each group varied by at most three-fold, enabling maximization of the signal gain. The black portion indicates the operating points that exceeded the hardware limitations. (b) The drive field waveform for each group and the number of operating points in each group. The waveform at each operating point contained 40 periods followed by a gap of the same duration.

5.3.3 Data post-processing

All post-processing was performed in MATLAB. Each baseline measurement was first subtracted from the corresponding sample measurement to eliminate any residual direct-feedthrough and potential interferences, and digitally upsampled 8 times. Then, the SPION signal was divided by the corresponding preamplifier gain used for that measurement. Next, the noise level was calculated using the non-harmonic frequencies, and the harmonics with signal levels above the noise level were selected. To avoid interference at the self-resonance frequency of the receive coil, only the frequencies smaller than 200 kHz were utilized. After that, a high-order zero-phase digital low-pass filter was applied in time domain, with the cut-off frequency set to the highest selected harmonic frequency.

5.3.4 Time Constant and Sensitivity Analysis

The relaxation time constant, τ, of the nanoparticle signal was estimated using TAURUS as described in Equation 2.31. The range of τ values among different drive field frequencies can differ considerably. Therefore, for quantitative comparison purposes, τ values were converted to percentages with respect to the corresponding drive field period, P_d, i.e.,

$$\hat{\tau} = \frac{\tau}{P_d} \times 100 \tag{5.5}$$

Here, $\hat{\tau}$ enables the quantification of the relative delay with respect to the period caused by relaxation.

Next, at each operating point, a linear fit was performed to the $\hat{\tau}$ values as a function of each functional parameter (i.e., temperature or viscosity) to quantify the sensitivity of the relaxation time constant to that parameter. The slope of this linear fit was utilized to define a sensitivity metric. Accordingly, temperature sensitivity of an operating point can be expressed as follows:

$$T_{sensitivity} = \frac{|\hat{\tau}_{end} - \hat{\tau}_{start}|/\hat{\tau}_{start}}{T_{end} - T_{start}} \times 100 \tag{5.6}$$

Here, $T_{sensitivity}$ describes the percentage change in $\hat{\tau}$ per 1°C change in temperature, and has the unit of %/°C. For the experiments in this work, T_{start} = 25°C and T_{end} = 45°C, and $\hat{\tau}_{start}$ and $\hat{\tau}_{end}$ are the $\hat{\tau}$ values corresponding to those temperatures on the fitted line. Likewise, viscosity sensitivity of an operating point can be expressed as follows:

$$\eta_{sensitivity} = \frac{|\hat{\tau}_{end} - \hat{\tau}_{start}|/\hat{\tau}_{start}}{\eta_{end} - \eta_{start}} \times 100 \tag{5.7}$$

Here, $\eta_{sensitivity}$ describes the percentage change in $\hat{\tau}$ per 1 mPa·s change in viscosity, and has the unit of %/mPa/s. For the experiments performed in this work, η_{start} = 0.9 mPa·s and η_{end} = 3.6 mPa·s, and $\hat{\tau}_{start}$ and $\hat{\tau}_{end}$ are the $\hat{\tau}$ values corresponding to those viscosity levels on the fitted line.

5.4 Results

5.4.1 Time Constant vs. Operating Point

The relative time constants with respect to period, $\hat{\tau}$'s, computed using Equation 5.5 are plotted in Figure 5.4 as a function of the drive field amplitude at seven different frequencies. The error bars indicate standard deviations (STD) across 3 repeated experiments. Here, the rows and the columns correspond to the results at distinct viscosity levels and temperatures, respectively. As expected, $\hat{\tau}$ decreases with drive field amplitude at all frequencies, as the SPIONs align faster under larger forcing fields. In contrast, $\hat{\tau}$ increases with drive field frequency, as the delay in the alignment of the SPIONs becomes more substantial at shorter periods. Interestingly, there is an outlier behavior at 0.9 mPa·s where $\hat{\tau}$ reaches its highest values at the lowest frequency of 1 kHz. In general, comparing the amount of change in $\hat{\tau}$ as the amplitude is increased five-fold and the frequency is increased seven-fold, it can be observed that the effect of amplitude on $\hat{\tau}$ is more dramatic than that of frequency. As the

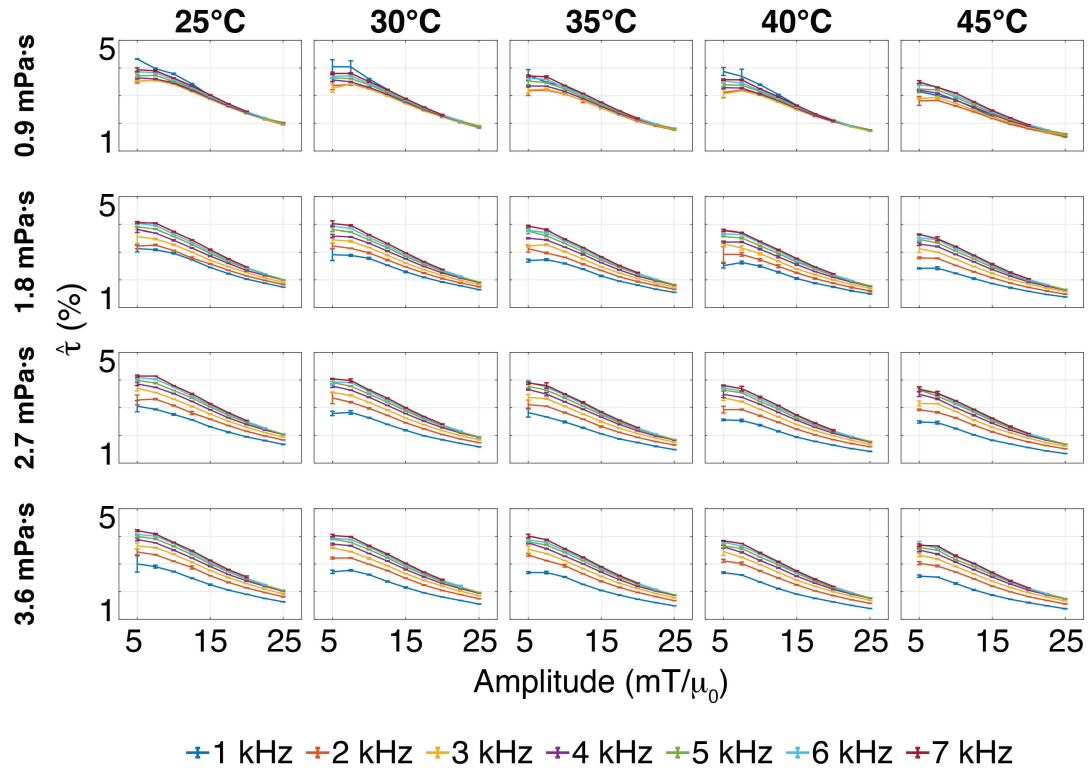

Figure 5.4: The relative time constants with respect to the drive field period, $\hat{\tau}$'s, plotted as a function of the drive field amplitude at seven different frequencies. The rows and the columns correspond to distinct viscosity levels and temperatures, respectively. Overall, $\hat{\tau}$ decreases with drive field amplitude and decreases with drive field frequency. Here, the error bars denote standard deviations across 3 repetitions.

field is increased from 5 mT/μ_0 to 25 mT/μ_0, $\hat{\tau}$ decreases by 48% on average (from 3.36% $\pm$ 0.40% to 1.75% $\pm$ 0.17%, mean $\pm$ STD). On the other hand, as the frequency is increased from 1 kHz to 7 kHz, $\hat{\tau}$ increases by 27% on average (from 2.47% $\pm$ 0.58% to 3.14% $\pm$ 0.60%, mean $\pm$ STD).

In Figure 5.5, the mean values of $\hat{\tau}$ at 60 different operating points are displayed as color maps, where the rows and the columns correspond to the results at distinct drive field frequencies and amplitudes, respectively. As stated previously, $\hat{\tau}$ decreases towards the low-frequency high-amplitude operating points, reaching the lowest values around (1 kHz, 25 mT/μ_0) and the highest values around (7 kHz, 5 mT/μ_0). The outlier behavior at 1 kHz and at 0.9 mPa·s in Figure 5.4 is also clearly visible in Figure 5.5 where $\hat{\tau}$ shows an abrupt increase. This behavior persists at higher temperatures, but

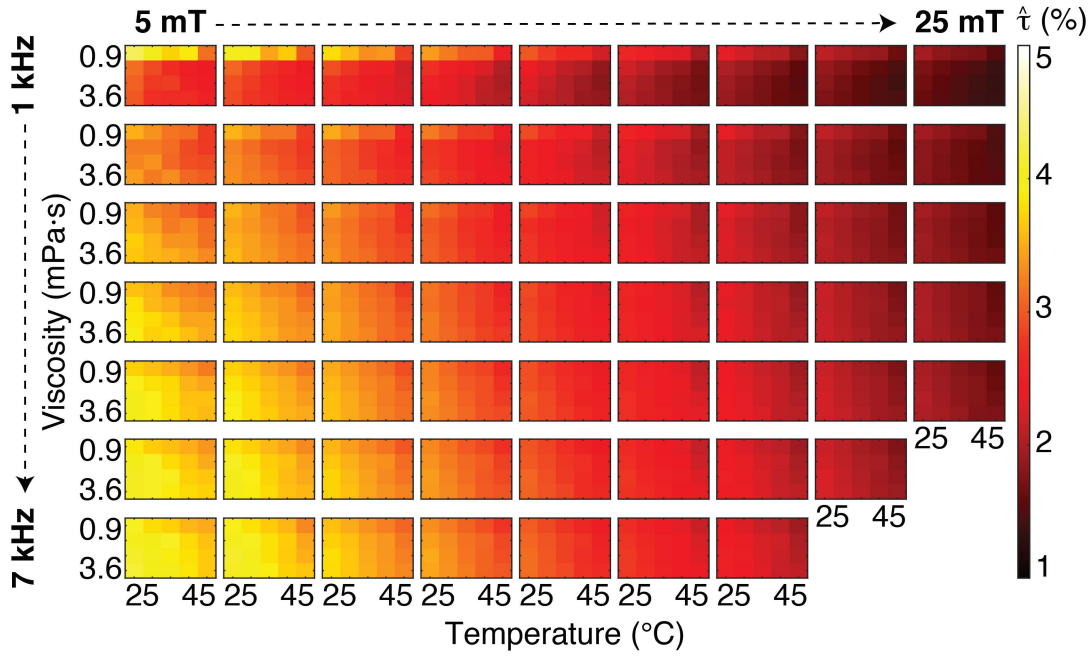

Figure 5.5: The mean values of $\hat{\tau}$ at 60 different operating points displayed as color maps, as a function of viscosity and temperature. The rows and the columns correspond to the results at distinct drive field frequencies with 1 kHz increments and amplitudes with 2.5 mT/μ_0 increments, respectively. Overall, $\hat{\tau}$ decreases with temperature and increases with viscosity.

diminishes at higher viscosity levels. As expected from Equations. 2.18 and 2.19, there is a global decrease in $\hat{\tau}$ as temperature increases. Moreover, $\hat{\tau}$ increases as viscosity increases at high frequencies, as expected from Equation 2.18. However, this trend changes at low frequencies indicating the insufficiency of the zero-field relaxation theory in explaining the trends for sinusoidal drive fields.

5.4.2 Temperature and Viscosity Sensitivities

In Figure 5.6, $\hat{\tau}$ is plotted with respect to each functional parameter (i.e., temperature or viscosity) at 4 selected operating points: (1 kHz, 5 mT/μ_0), (1 kHz, 25 mT/μ_0), (7 kHz, 5 mT/μ_0), and (6 kHz, 22.5 mT/μ_0). In Figure 5.6(a), a line is fitted to each $\hat{\tau}$ vs. temperature curve at 4 different viscosity levels. Likewise, in Figure 5.6(b), a line is fitted to each $\hat{\tau}$ vs. viscosity curve at 5 different temperatures. Here, the

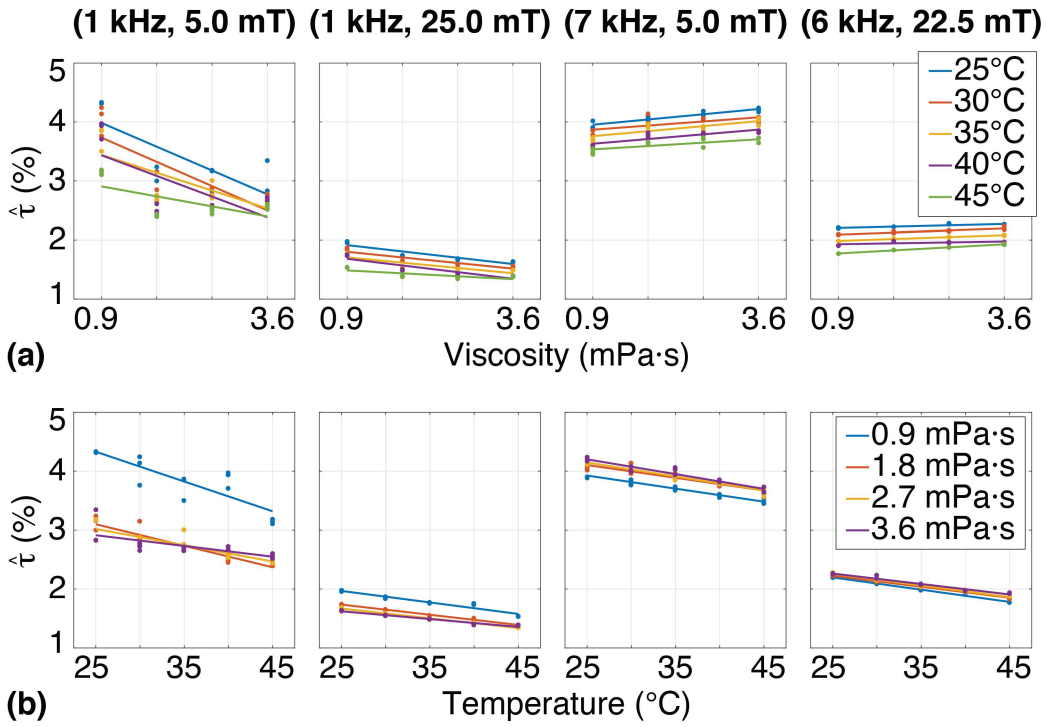

Figure 5.6: $\hat{\tau}$ with respect to temperature and viscosity at 4 selected operating points. From left to right: (1 kHz, 5 mT/μ_0), (1 kHz, 25 mT/μ_0), (7 kHz, 5 mT/μ_0), (6 kHz, 22.5 mT/μ_0). (a) $\hat{\tau}$ vs. temperature at 4 different viscosity levels, and (b) $\hat{\tau}$ vs. viscosity at 5 different temperatures. Here, each dot represents a measurement (all 3 repetitions marked separately), and the lines correspond to the linear fits to $\hat{\tau}$ vs. temperature or $\hat{\tau}$ vs. viscosity. This procedure is repeated at all operating points and the sensitivity metrics are computed using the slopes of the linear fits.

sensitivity metrics given in Equations. 5.6 and 5.7 are computed using the slopes of the above-mentioned linear fits, and they describe the percentage change in $\hat{\tau}$ as a function of temperature or viscosity. Accordingly, in Figure 5.6(a), $\hat{\tau}$ decreases with temperature at all operating points and at all viscosity levels, displaying the highest temperature sensitivities at 1 kHz. For example, at (1 kHz, 5 mT/μ_0), the temperature sensitivity is 1.17 %/°C at 0.9 mPa·s. As the frequency increases, the temperature sensitivity decreases, reaching a value of 0.57 %/°C at (7 kHz, 5 mT/μ_0) at 0.9 mPa·s. In Figure 5.6(b), $\hat{\tau}$ decreases rapidly with increasing viscosity at all temperatures at (1 kHz, 5 mT/μ_0), corresponding to a viscosity sensitivity of 11.3%/mPa/s at 25°C. In contrast, $\hat{\tau}$ vs. viscosity curves flatten out at higher frequencies, indicating reduced sensitivities to viscosity. For example, at (6 kHz, 22.5 mT/μ_0), the viscosity sensitivity

is 1.13%/mPa/s at 25°C.

Next, in Figure 5.7, the estimated sensitivities for temperature and viscosity for all operating points are given as color maps. Figure 5.7(a) shows temperature sensitivities at different operating points in units of %/°C, computed using Equation 5.6. Here, each subplot displays the temperature sensitivities at distinct viscosity levels from 0.9 mPa·s to 3.6 mPa·s. As seen in these results, temperature sensitivity changes relatively slowly across different operating points, displaying a smooth trend. The highest temperature sensitivity values of >1 %/°C are obtained at high-amplitude operating points, with a maximum value of 1.19 %/°C achieved at (1 kHz, 12.5 mT/μ_0) at 1.8 mPa·s. As a function of viscosity, temperature sensitivities have the highest values at the lowest viscosity level of 0.9 mPa·s, and they fall down gradually at higher viscosity levels.

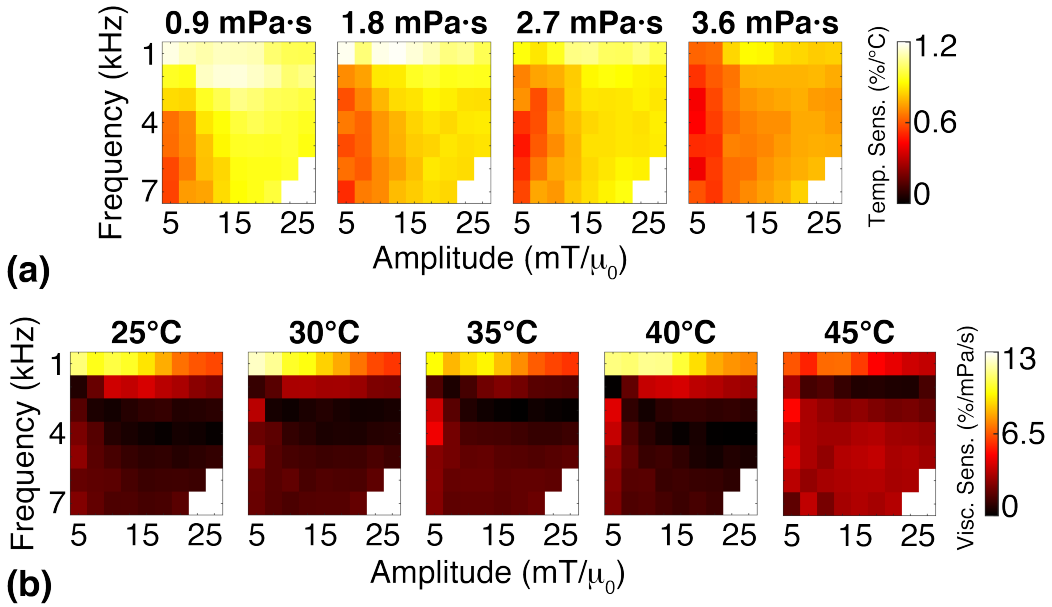

Figure 5.7: The estimated temperature and viscosity sensitivities at all operating points displayed as color maps. (a) The temperature sensitivities (in %/°C) at 4 different viscosity levels change relatively slowly across different operating points, reaching the highest values of >1 %/°C at high-amplitude operating points. (b) The viscosity sensitivities (in %/mPa/s) at 5 different temperatures show a drastic change as a function of drive field frequency, reaching the highest values of >10%/mPa/s at low frequencies around 1 kHz.

The viscosity sensitivities at different operating points estimated using Equation 5.7 are shown in Figure 5.7(b), in units of %/mPa/s. Here, each subplot corresponds to

viscosity sensitivities at a distinct temperature from 25°C to 45°C. In contrast to the slowly varying changes seen in the temperature sensitivity maps, viscosity sensitivity displays a drastic change as a function of drive field frequency. As seen in this figure, viscosity sensitivity reaches values >10%/mPa/s at low frequencies around 1 kHz with a maximum value of 12.2%/mPa/s achieved at (1 kHz, 5 mT/μ_0) at 30°C, but rapidly falls down at around 3-4 kHz. When evaluated as a function of temperature, viscosity sensitivity remains almost constant at temperatures ≤40°C, while it falls down at 45°C.

Overall, Figure 5.7 clearly demonstrates the viscosity dependence of temperature sensitivity and the temperature dependence of viscosity sensitivity, underscoring the confounding effects of these two environmental parameters on the relaxation time constant.

5.5 Discussion

In this work, the simultaneous effects of temperature and viscosity on relaxation time constant estimation via TAURUS were analyzed. The results show that the drive field settings have a substantial impact on how sensitive τ is to these environmental parameters. According to the results in Figure 5.7(a), temperature sensitivity varies smoothly as a function of frequency and amplitude, showing the highest values at high drive field amplitudes. In contrast, Figure 5.7(b) demonstrates that viscosity sensitivity is highly concentrated to low frequencies around 1 kHz, whereas the time constants largely get desensitized to the viscosity effect for frequencies higher than 3 kHz. This result indicates that the Néel relaxation process, which does not depend on viscosity, must dominate at higher frequencies. Note that these results are in line with the previous work, which has shown that the Brownian relaxation is dominant at lower frequencies [163, 174, 175, 176, 177]. Based on these results, two different strategies can be envisioned for simultaneous temperature and viscosity mapping via TAURUS: (1) Performing measurements at two different drive field frequencies, e.g., one measurement at (1 kHz, 5 mT/μ_0) where both temperature and viscosity sensitivities are high, and another measurement at (4 kHz, 15 mT/μ_0) where viscosity sensitivity is minimized

but temperature sensitivity is still high. (2) Performing measurements at two different drive field amplitudes at a fixed frequency around 1 kHz, e.g., one measurement at (1 kHz, 5 mT/μ_0) where both temperature and viscosity sensitivities are high, and another measurement at (1 kHz, 25 mT/μ_0) where temperature sensitivity is high but viscosity sensitivity is considerably lower. Alternatively, if the goal is to estimate the temperature alone, a single measurement can be performed at a medium-to-high amplitude drive field at frequencies above 3 kHz, where the signal is largely desensitized to the viscosity effect but is highly sensitive to temperature.

The temperature and viscosity metrics in Equations. 5.6 and 5.7 were defined using the slopes of the linear fits to $\hat{\tau}$ vs. temperature and $\hat{\tau}$ vs. viscosity curves. According to Equations. 2.18 and 2.19, while τ_B linearly depends on viscosity, neither τ_B nor τ_N has linear dependence with respect to temperature. However, from 25°C to 45°C, the absolute temperature in Kelvin changes by only about 6.7%. In this narrow range of temperatures, a linear approximation to $\hat{\tau}$ vs. temperature shows a very good fit with the measurements, as seen in Figure 5.6(a). Despite the small change in absolute temperature, the estimated time constants change by more than 20% at the highest sensitivity operating points, underscoring the temperature mapping capability of MPI. For the operating points tested in this work, the highest temperature sensitivity of TAURUS reaches 1.19%/°C. As a comparison, MRI thermometry was shown to have the following sensitivity levels [178]: equilibrium magnetization M_0 has a sensitivity of 0.3%/°C, T_1 relaxation constant has a sensitivity of 1%/°C, and the resonance frequency has a sensitivity of 0.01 ppm/°C. While some of these sensitivities are comparable to that of TAURUS, MFH treatments cannot be integrated within an MRI scanner, as the static B_0 field would saturate the SPION response. In contrast, MPI is compatible with MFH and provides localized heating capability, all the while promising high sensitivity thermometry. It should be noted that for *in vivo* cases, the accuracy of τ estimation itself will be as important as temperature sensitivity in determining the performance of MPI thermometry.

In contrast to the relatively small 6.7% change in absolute temperature, the change in viscosity from 0.9 mPa·s to 3.6 mPa·s is four-fold. While Equation 2.18 indicates a linear relationship between τ_B and viscosity for the zero-field case, τ as measured in this work does not correspond to the Brownian relaxation alone and the zero-field

assumption does not apply in MPI. Consequently, in this wide range of viscosity levels, the linear fits to $\hat{\tau}$ vs. viscosity curves may not reflect the true trends. For example, in Figure 5.6(b), $\hat{\tau}$ shows a nonlinear trend especially at (1 kHz, 5 mT/μ_0). The highest viscosity sensitivity of 12.2%/mPa/s is also achieved at this operating point. If the linear fits were computed using the lowest two viscosity levels of 0.9-1.8 mPa·s, the viscosity sensitivity would reach even higher values of >30%/mPa/s at 1 kHz. These high viscosity sensitivities underline the cancer imaging potential of MPI via viscosity mapping, as tumor micro-environment is known to have high viscosity levels [179].

According to Figure 5.7, temperature sensitivity decreases with viscosity and viscosity sensitivity decreases with temperature. As given in Equations. 2.18 and 2.19, viscosity is only effective on the Brownian relaxation process, whereas temperature is effective on both the Néel and Brownian relaxations. Therefore, the decrease in viscosity sensitivity seen at higher temperatures can potentially be interpreted as the Néel relaxation gradually dominating over the Brownian relaxation as the temperature is increased. On the other hand, at higher viscosity levels, the relaxation starts to get dominated by the Néel relaxation, as the Brownian rotation significantly slows down [180, 181]. Consequently, temperature sensitivity may be higher at low viscosity levels as it has both Brownian and Néel contributions, while being restricted to the Néel contribution alone at higher viscosity levels, explaining the decrease in temperature sensitivity.

The experiments in this work were performed on an arbitrary waveform MPS setup that enabled a wide range of operating points to be rapidly covered. It is important to note that TAURUS can be directly applied to MPI imaging experiments, as well [142, 143]. With that said, the previous work has shown that τ vs. viscosity curves follow similar trends for both MPS and MPI cases, but with a given trend observed at higher frequencies for the MPI case [143]. Furthermore, the previous MPS results have demonstrated that τ vs. viscosity curves of different SPIONs also showed similar trends but at different frequencies [60]. Both of these observations indicate that there are underlying global trends in τ dictated by SPION characteristics and environmental conditions, and that MPS results can be utilized to forecast MPI results. Notwithstanding, a similar analysis to the one presented in this work should also be

performed to demonstrate the simultaneous temperature and viscosity mapping capability of relaxation-based color MPI for imaging applications and using different SPIONs, which remains an important future work.

5.6 Conclusion

In this chapter, the simultaneous temperature and viscosity mapping capability of MPI was demonstrated, showing highly promising temperature sensitivity and viscosity sensitivity levels for relaxation time constant estimation via TAURUS. The results of the extensive experiments performed on an in-house arbitrary waveform MPS setup show that the temperature sensitivity changes slowly across different drive field settings, while the viscosity sensitivity is concentrated to low frequencies around 1 kHz. Accordingly, temperature and viscosity can be simultaneously mapped by performing measurements at two different drive field settings with complementary temperature/viscosity sensitivities. Alternatively, temperature mapping alone can be achieved at frequencies above 3 kHz by desensitizing the signal to the viscosity effect. The presented results demonstrate the functional imaging capability of MPI, revealing the potential of a hybrid MPI-MFH system for real-time monitored and localized thermal ablation treatment of cancer. In such a hybrid system, the simultaneous mapping of temperature and viscosity can provide feedback to adjust the thermal dose while pinpointing the treatment to the location of the tumor region.

Chapter 6

Relaxation-Based Color MPI for Simultaneous Temperature and Viscosity Mapping

This chapter is based on the following publications:

- M. Utkur and E. U. Saritas, "Temperature Mapping via Relaxation-Based Color MPI," in 10th International Workshop on Magnetic Particle Imaging (IWMPI), Digital, 2020.
- M. Utkur and E. U. Saritas, "Non-invasive and Simultaneous Temperature and Viscosity Estimation in Magnetic Particle Imaging via Relaxation Characterization of Iron Oxide SPIONs," in 14th World Molecular Imaging Congress (WMIC), Miami, 2021.

6.1 Introduction

This chapter presents the imaging results of relaxation-based color MPI for simultaneous temperature and viscosity mapping. The color MPI experiments are based on

TAURUS technique, and in line with the imaging experiments for viscosity mapping in Chapter 4. The temperature and viscosity sensitivity estimations in this chapter are quantitatively compared with the MPS results shown in Chapter 5. The color MPI results demonstrate the capability of TAURUS to differentiate therapeutically applicable temperature range (25-45°C) for biologically meaningful viscosity levels between 0.90-1.42 mPa·s.

6.2 Methods and Experimental Procedures

6.2.1 Experimental Setup

The in-house MPI scanner described in detail in Chapter 3 was used in color MPI experiments in this chapter (see Figure 6.1). This scanner utilized a drive field coil that had 3 layers of 125-strand 40 AWG Litz wire with 79 turns in each layer, and a receive coil that is a three-section gradiometer type coil with a single layer of 125-strand 44 AWG Litz wire. The middle and side sections of the receive coil had 34 turns and 19 turns, respectively. One side section of this receive coil was able to move independently from the other two sections and its position was adjusted manually to minimize the direct feedthrough signal.

6.2.2 Sample Preparation

An imaging phantom was prepared, containing five different SPION samples placed on a temperature-controlled water tube. Each sample had the same total volume of 20 μL, and the same SPION volume of 5 μL of Nanomag-MIP SPIONs. Then, different amounts of water/glycerol mixtures were added to each sample to obtain 0% (in only water), 8.8%, 16.8%, 24.4%, and 32.1% glycerol percentages by volume as shown in Figure 6.1. The viscosity levels of these samples at 25°C, 35°C, and 45°C are shown in the table in Figure 6.1, which were computed by interpolating the values in the literature [171].

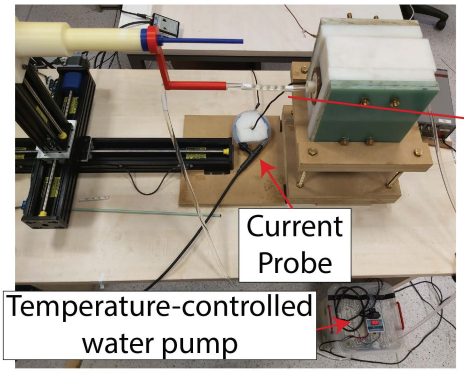

Glycerol (%)		0	8.8	16.8	24.4	32.1
Viscosity (mPa·s)	25˚C	0.90	1.12	1.42	1.83	2.40
	35˚C	0.73	0.90	1.12	1.42	1.83
	45˚C	0.60	0.73	0.90	1.12	1.42

Figure 6.1: The in-house MPI scanner and imaging phantom. Five samples containing Nanomag-MIP SPIONs at different viscosity levels were prepared on a temperature-controlled water tube with a solid 3D printed part holding the samples parallel to the bore axis. Since the viscosity level of a fixed glycerol percentage decreases with temperature, the imaging phantom was designed to achieve three targeted viscosity levels (0.90 mPa·s, 1.12 mPa·s, and 1.42 mPa·s) at three different temperatures (25°C, 35°C, and 45°C), as highlighted with different colors in the table.

6.2.3 Imaging Experiments

The different drive field frequencies and amplitudes can change the trends in τ significantly. It was observed via color MPI experiments in Chapter 4 that operating around 10 kHz is well suited for viscosity mapping purposes using Nanomag-MIP SPIONs. Therefore, the drive field frequency for the imaging experiments in this chapter was chosen as 9.8 kHz. The drive field was applied in the z-direction at four different drive field amplitudes between 15 mT/μ_0 and 45 mT/μ_0. For 1D imaging experiments, a 15 cm FOV was covered by 73, 41, 27, and 19 pFOVs with 85% overlap at drive field amplitudes of 15 mT/μ_0, 25 mT/μ_0, 35 mT/μ_0, and 45 mT/μ_0, respectively. The received signal was amplified with a low-noise pre-amplifier (Stanford Research Systems SR560) with the gains of 50 for measurement at 15 mT/μ_0 and 20 for measurements at 25 mT/μ_0, 35 mT/μ_0, and 45 mT/μ_0. The filter setting of the preamplifier was fixed to the cut off frequencies of 1 kHz in the high pass band and 300 kHz in the low pass band with 6 dB/octave roll-offs. The imaging phantom was fully sealed with hot glue, and wrapped with parafilm to prevent water leakage. A temperature-controlled water pump circulated hot water inside a water tube, and the imaging samples were placed inside the water tube and heated up to the targeted temperature conductively. The temperature of the circulating water was monitored throughout the experiments and considered

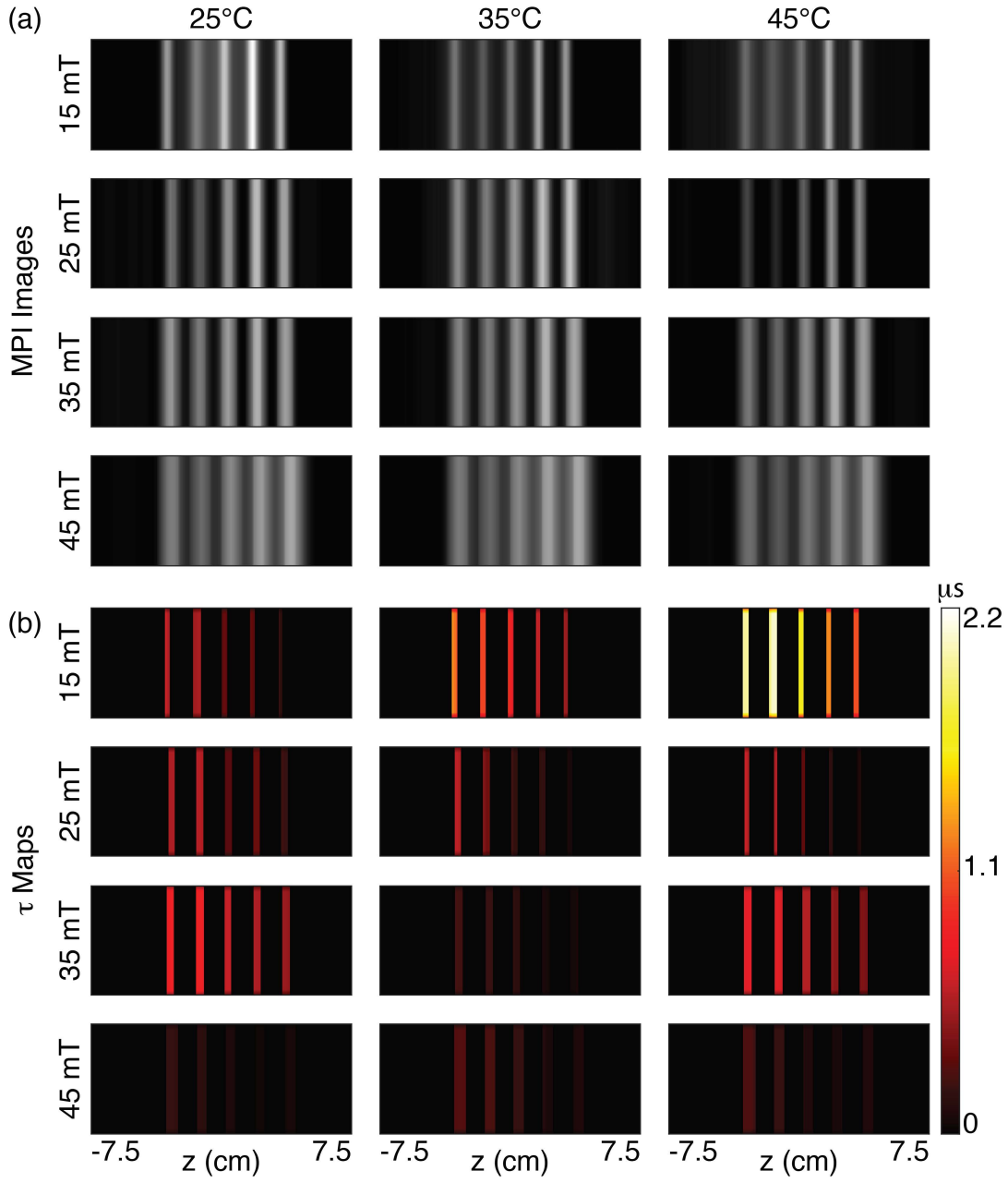

Figure 6.2: 1D imaging experiment results at four different drive fields amplitudes at 9.8 kHz, and at three different temperatures. (a) MPI images and (b) τ maps of the imaging phantom containing five SPION samples with increasing viscosity levels from left to right. These 1D MPI images and τ maps were replicated in the vertical direction for display purposes.

to be the same as the SPION temperature. A total of twelve 1D imaging experiments were performed (i.e., four drive field amplitudes and three temperatures).

6.2.4 Post-Processing

To quantitatively compare the results of the imaging experiments in this chapter with the MPS results in Chapter 5, the estimated relaxation time constant (i.e., τ) was converted to percentage (i.e., $\hat{\tau}$) with respect to the drive field period of 102 μs, using Equation 5.5. Then, a line was fitted to each $\hat{\tau}$ vs. temperature and $\hat{\tau}$ vs. viscosity curve, and the sensitivity metrics for temperature and viscosity were calculated with Equations 5.6 and 5.7 using the slopes of these linear fits. For the experiments in this chapter, T_{start} = 25°C and T_{end} = 45°C, and η_{start} = 0.9 mPa·s and η_{end} = 1.42 mPa·s.

6.3 Results

The 1D MPI images, and τ maps at four different drive field amplitudes and three different temperatures are shown in Figure 6.2. Each row and column in this figure corresponds to the results at distinct amplitudes and temperatures, respectively. The sample order in this figure is in increasing viscosity levels from left to right.

The τ values were extracted from the τ maps and converted to percentages using Equation 5.5, then plotted as a function of drive field amplitude in Figure 6.3. The mean values and standard deviations were computed from the regions-of-interest of the corresponding samples in τ maps. In general, $\hat{\tau}$ decreases with increasing amplitude due to the fact that the SPION alignment occurs faster at higher amplitudes. Surprisingly, $\hat{\tau}$ at low amplitudes increases with temperature and decreases with viscosity, which can not be explained by the zero-field Brownian and Néel relaxation mechanisms. It has been already discussed in Chapters 4 and 5 that zero-field mechanisms do not describe the relaxation behavior of SPIONs under sinusoidal drive fields [60, 143].

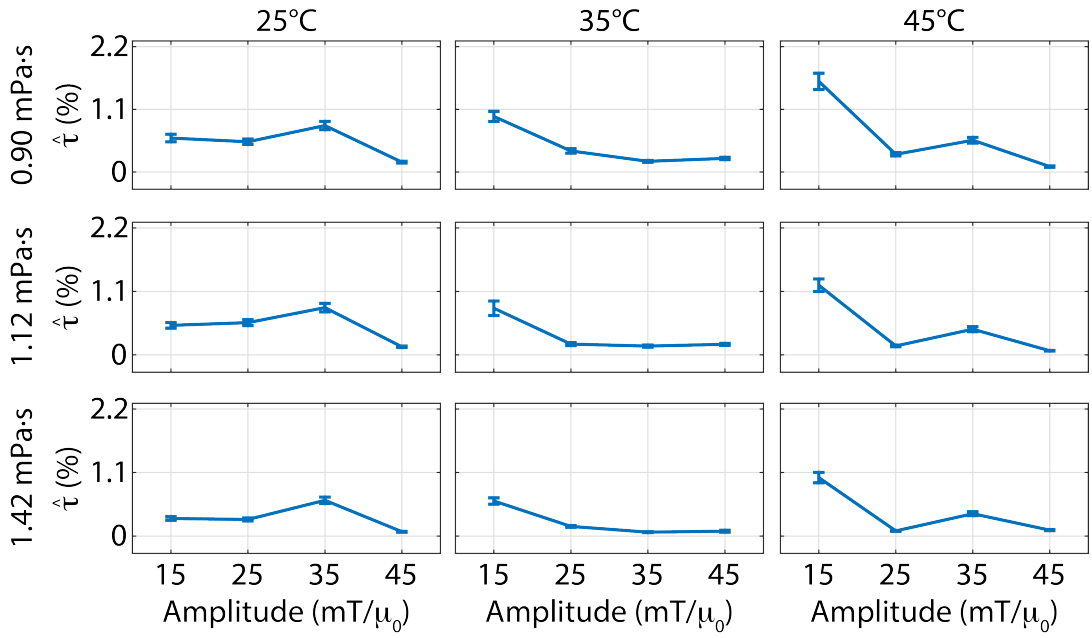

Figure 6.3: The relative time constants (i.e., $\hat{\tau}$'s) plotted as a function of drive field amplitude at three different viscosity levels and temperatures. Here, $\hat{\tau}$'s were calculated by τ values extracted from τ maps in Figure 6.2 and converted to percentages. Mean values and standard deviations were computed from the regions-of-interest of the samples.

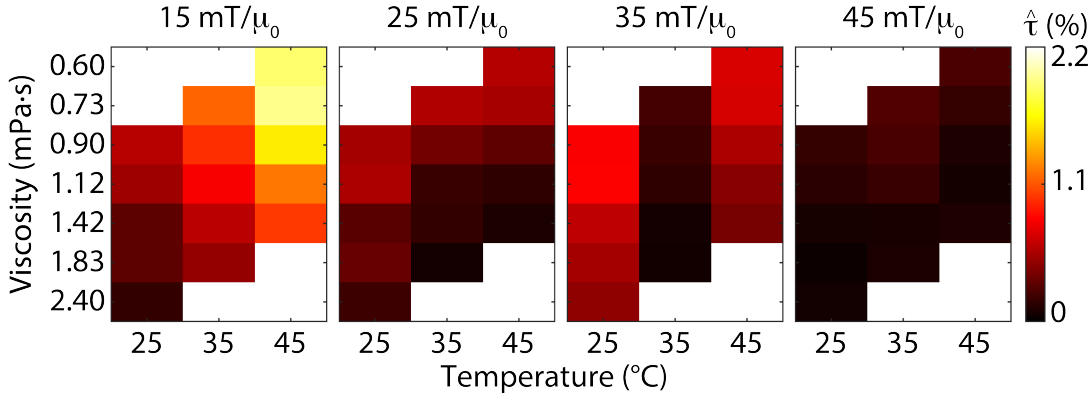

Figure 6.4: The color maps display the mean values of $\hat{\tau}$ at four different drive field amplitudes at 9.8 kHz, as a function of viscosity and temperature. As expected, $\hat{\tau}$ decreases with drive field amplitude since the SPION magnetization aligns faster under larger magnetic fields.

In Figure 6.4, the mean $\hat{\tau}$ values at four different drive field amplitudes are presented as color maps as a function of viscosity and temperature. As also seen in Figure 6.3, the decrease in $\hat{\tau}$ with respect to amplitude is clearly visible in this figure. The effect of temperature on $\hat{\tau}$ was observed to be highest at 15 mT/μ_0.

In Figure 6.5, $\hat{\tau}$ is plotted with respect to temperature and viscosity at four different drive field amplitudes. In Figure 6.5(a), a line is fitted to each $\hat{\tau}$ vs. temperature curve at viscosity levels of 0.90 mPa·s, 1.12 mPa·s, and 1.42 mPa·s. The slopes of these lines are used for computing the temperature sensitivity metric in Equation 5.6. $\hat{\tau}$ at 15 mT/μ_0 increases with temperature, whereas the trend switches after 25 mT/μ_0 and $\hat{\tau}$ starts to decrease with temperature. At 45 mT/μ_0, $\hat{\tau}$ vs. temperature curve becomes almost flat. Similarly in Figure 6.5(b), a line is fitted to each $\hat{\tau}$ vs. viscosity curve at three different temperature values of 25°C, 35°C, and 45°C. Again, the slopes of these lines are used for computing the viscosity sensitivity metric in Equation 5.7. Here, $\hat{\tau}$ decreases with increasing viscosity at all amplitudes.

In Figure 6.6, the estimated temperature and viscosity sensitivities are plotted as a function of drive field amplitude, where Figure 6.6(a) shows the temperature sensitivities between 0.90-1.42 mPa·s, and Figure 6.6(b) shows the viscosity sensitivities between 25-45°C. The highest temperature sensitivity among the different drive field amplitudes is observed at 15 mT/μ_0 with values around 10%/°C, then the sensitivity decreases to around 2%/°C as the amplitude reaches to 45 mT/μ_0. Unlike the temperature sensitivity, the viscosity sensitivity yields similar values among different amplitudes. Interestingly, the viscosity sensitivity increases with temperature. Across the tested drive field amplitudes, the viscosity sensitivity at 25°C is around 40%/mPa/s on average, and it goes up to approximately 85%/mPa/s on average at 45°C. These sensitivities clearly demonstrate the confounding effects of temperature and viscosity in MPI.

6.4 Discussion

In this work, the simultaneous effects of temperature and viscosity on relaxation time constant estimations with TAURUS were investigated via color MPI experiments at four different drive field amplitudes. The results indicate that τ estimations are highly dependent on the drive field amplitude. The maximum temperature sensitivity is estimated to be around 10%/°C at drive field amplitude of 15 mT/μ_0, then, the sensitivity suddenly drops to values around 2-3%/°C after 25 mT/μ_0. These trends are almost the same at all three viscosity levels. According to the MPS findings in Chapter 5 (Figure 5.7), the highest temperature sensitivity was estimated to be 1.19%/°C at drive field amplitudes around 15 mT/μ_0 and frequency of 1 kHz, and then the sensitivity slowly decreases to under 1%/°C as the amplitude increases. Although the sensitivity trends with respect to the drive field amplitude are similar in both the MPS and the color MPI measurements, the highest estimated sensitivities differ by almost one order of magnitude. This difference may stem from the difference in the drive field frequencies between the two measurements (i.e., 1.1 kHz in MPS and 9.8 kHz in MPI measurements). Nevertheless, the exact reason as to why the selection field causes such a drastic change in temperature sensitivity is still unknown.

The viscosity sensitivities in the color MPI measurements slowly vary across different field amplitudes but significantly increase with temperature. The viscosity sensitivity in Figure 6.6 is estimated to be approximately 40%/mPa/s at 9.8 kHz and 25 mT/μ_0, and at 25°C. Note that these viscosity sensitivities were computed for a viscosity range of 0.90-1.42 mPa·s. According to the color MPI findings in Chapter 4, the viscosity sensitivity was estimated to be around 12%/mPa/s at room temperature (i.e., 25°C) at 9.7 kHz and 25 mT/μ_0 in a viscosity range of 0.9-5.0 mPa·s. However, if a narrower viscosity range of 0.9-1.5 mPa·s had been selected, the sensitivity would have risen up to around 35%/mPa/s. Moreover, the MPS findings in Chapter 5 yields sensitivity values higher than 30%/mPa/s in a viscosity range of 0.9-1.8 mPa·s at 1 kHz drive field. Therefore, the viscosity sensitivity results provided in this chapter are in agreement with the previous measurements.

The strategy for simultaneous temperature and viscosity mapping proposed in

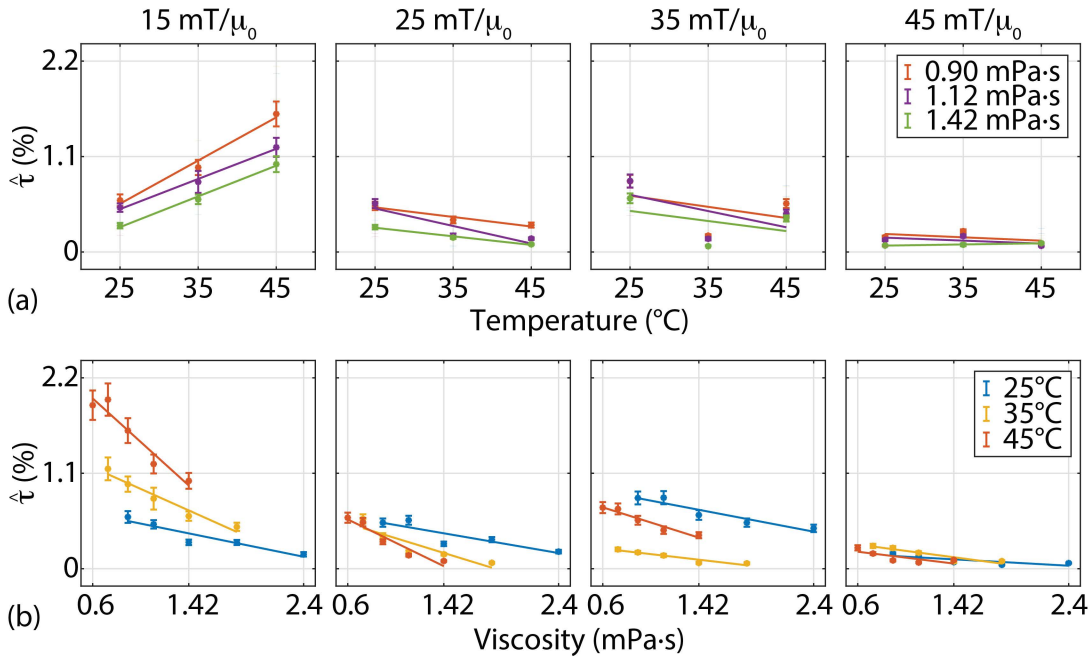

Figure 6.5: $\hat{\tau}$ plotted as a function of (a) temperature and (b) viscosity at four different drive field amplitudes at 9.8 kHz. Here, the errorbars represent the standard deviation from the region-of-interest of the samples, and the lines correspond to the linear fits to $\hat{\tau}$ curves.

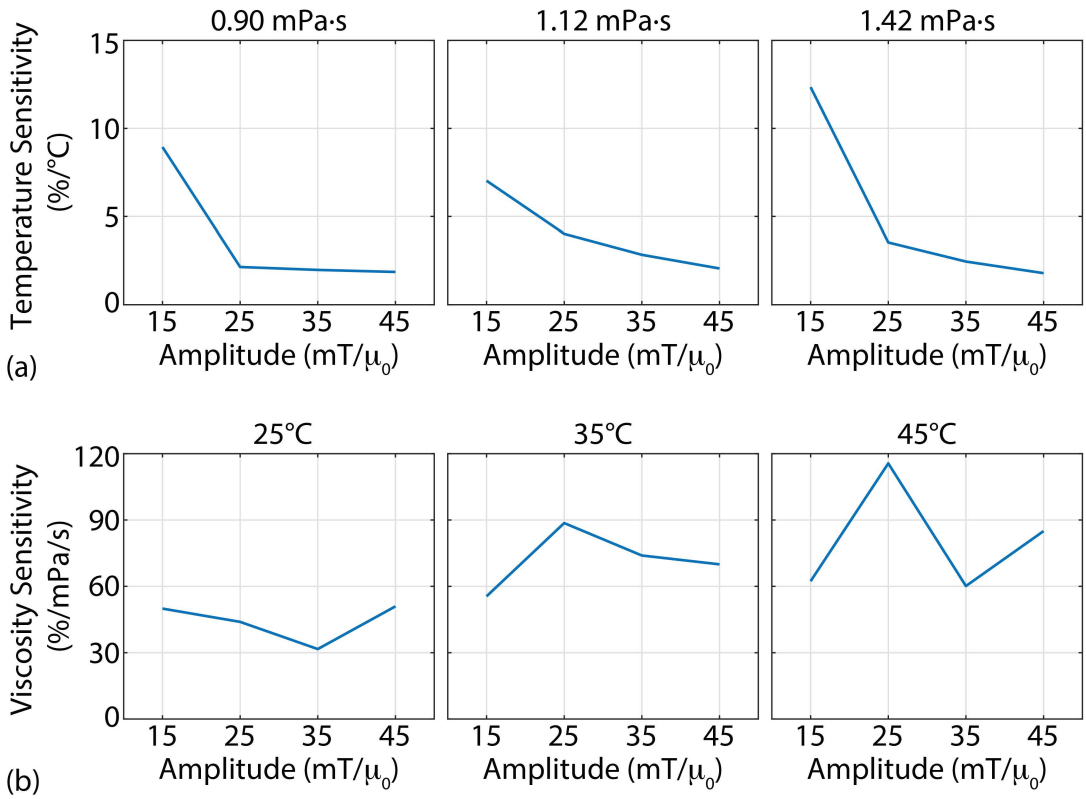

Figure 6.6: The estimated sensitivities for temperature and viscosity at four different drive field amplitudes at 9.8 kHz. (a) The temperature sensitivity is highest at 15 mT/μ_0 with a value of approximately 10%/°C and decreases as the amplitude increases. (b) The viscosity sensitivities are very similar between different amplitudes, and increase with temperature. The viscosity sensitivity at 25°C is around 40%/mPa/s on average, and almost doubles at 45°C to values around 85%/mPa/s on average.

Chapter 5 can be achieved by performing two measurements at two different amplitudes, e.g., one measurement at 9.8 kHz and 15 mT/μ_0 where the temperature sensitivity is the highest and the viscosity sensitivity is reasonably high, and another measurement at 9.8 kHz and an amplitude between 25-45 mT/μ_0 where temperature sensitivity is low but the viscosity sensitivity is still high. One concern for operating at lower amplitudes is the reduction in the SNR since the SPION response is picked up inductively. This disadvantage, however, can be compensated by the increased spatial resolution since the MPI images have better resolution at lower amplitudes as shown in the literature [153, 143]. The improvement in the spatial resolution at lower amplitudes is also clearly visible in Figure 6.2(a).

Here, the choice of the drive field parameters was based on the previous viscosity mapping results given in Chapter 4, however, an increased number of operating points may reveal better differentiation (i.e., higher contrast) between the functional parameters. In Chapter 5, the measurements were conducted using an in-house arbitrary waveform MPS setup. The arbitrary waveform characteristics of this setup enabled the investigation of the effect of temperature and viscosity on τ estimations at a wide range of operating points. Similar arbitrary waveform designs for an MPI scanner would be extremely useful to comprehensively understand the relaxation effects in MPI. To develop arbitrary waveform MPI scanners, however, the drive coils must be designed to have low inductance so that the requirement of impedance matching is eliminated. Such designs may utilize shorter drive coils with lower homogeneous regions, or alternatively, different winding patterns for the drive coil such as Roebel or Rutherford may be used [182, 183].

The decoupling of the drive and receive coils was performed by manually adjusting the position of the one end section of the receive coil. The imaging phantom was prepared using a water tube that had an outer diameter very close to the inner diameter of the receive coil. A 3D printed plastic rod held the water tube in line with the bore axis of the receive coil. Considering that the decoupling of the coils should not change during measurements, the imaging phantom can not hold more than five samples as the flexural rigidity of the plastic rod can not sustain the increased bending force of a longer water tube. In addition, a thicker rod could have been used to increase its rigidity, however, it was not applicable due to narrow bore diameter of the receive coil. Consequently, the choice of the highest viscosity level was limited to 1.42 mPa·s. The narrow free bore size of the in-house MPI scanner also led the imaging experiments to be performed in one dimension only. One possible approach to overcome the mutual inductance problem in MPI might be using active decoupling approaches, where stable receive coils can be designed without any moving parts [184].

6.5 Conclusion

In this chapter, the capability of TAURUS for simultaneous temperature and viscosity mapping has been demonstrated via color MPI experiments. The imaging experiments were performed on the in-house MPI scanner at four different drive field amplitudes. The proposed strategy to simultaneously map the functional parameters is applicable by performing two imaging experiments at two different amplitudes, and resolving for the complementary temperature and viscosity information. The presented results reveal the potential of MPI as a promising functional mapping technique.

Chapter 7

Summary and Future Work

7.1 Summary

MPI gains functional imaging capabilities through the relaxation behavior of the SPIONs, since the environmental conditions such as viscosity and temperature change the SPION response. One of the relaxation estimation techniques in MPI literature, which works directly with the time-domain SPION signal, is called TAURUS. This thesis investigates the functional imaging capability of MPI via TAURUS, and comprises of four main studies: (1) The design and development of an in-house MPI scanner to perform color MPI experiments, (2) relaxation-based color MPI for viscosity mapping, (3) a comprehensive analysis of the effects of temperature and viscosity on the estimated time constants using an in-house MPS setup, and finally (4) relaxation-based color MPI for simultaneous temperature and viscosity mapping.

The first study includes a detailed description of the design and construction steps of an in-house MPI scanner that has a field-free-point topology. The development of this MPI scanner took place in Bilkent University National Magnetic Resonance Research Center (UMRAM), and it is the first MPI scanner made in Turkey. Although the bore size of this scanner is too narrow for small animal imaging, it is sufficient to perform proof-of-concept color MPI experiments. The 4.8 T/m/μ_0 gradient strength of this

scanner achieves a spatial resolution of $\sim$5 mm for commercially available Nanomag-MIP and Perimag SPIONs (Micromod GmbH), and a spatial resolution of $\sim$7 mm for commercially available VivoTrax SPIONs (Magnetic Insight).

The imaging demonstration of TAURUS for viscosity mapping constitutes the second study of this thesis. The biologically meaningful viscosity range is distinguished via TAURUS with color MPI experiments using the in-house MPI scanner. To achieve the maximum contrast between different viscosity levels, three different drive field frequencies are compared using Nanomag-MIP SPIONs. The results show that one-to-one mapping between the viscosity level and the time constants estimated with TAURUS has the viscosity sensitivity of approximately 10%/mPa/s for viscosity range from 0.89 mPa·s (i.e., in water) to 5 mPa·s, and even higher viscosity sensitivity of approximately 30%/mPa/s for narrow viscosity range between 0.89-1.5 mPa·s. This successful differentiation between viscosity levels suggests that TAURUS can potentially be used for cancer imaging as cancerous tissues have higher viscosity levels than healthy tissues.

The next two studies incorporate the temperature mapping capability of TAURUS. The potential of MPI thermometry is especially useful for hybrid MPI-MFH systems, since treatment monitoring with MPI can enable guiding of the MFH treatments to accurately adjust the thermal dose. Considering the fact that temperature and viscosity have confounding effects on the SPION response, the third study of this thesis investigates the effects of temperature and viscosity on the estimated time constant using TAURUS. The temperature and viscosity sensitivities of MPI at a wide range of operating points are determined with extensive experiments using an in-house arbitrary waveform MPS setup with temperature-controlled heating capability. The highest temperature and viscosity sensitivities are estimated as 1.19%/°C and 12.2%/mPa/s, respectively. The results suggest that the temperature mapping can be achieved with a single measurement at the drive field frequencies where viscosity sensitivity is minimized. More importantly, the simultaneous mapping of temperature and viscosity can be achieved by performing measurements at two different drive field settings that provide complementary temperature/viscosity sensitivities.

In the fourth study, 1D color MPI experiments were performed with the in-house

MPI scanner for simultaneous temperature and viscosity mapping using TAURUS. The imaging experiments were performed at three different temperatures using an imaging phantom that contains SPIONs at different viscosity levels such that the confounding effects between the two functional parameters can be simultaneously analyzed. Accordingly, the temperature sensitivity is estimated to be approximately 10%/°C at lower drive field amplitudes, converging to around 2%/°C at higher amplitudes. In addition, the viscosity sensitivity varies relatively slowly with the drive field amplitude, and it is estimated to be around 40%/mPa/s at room temperature. The imaging results suggest that simultaneous temperature and viscosity mapping can be performed by operating at two different drive field settings (i.e., two different imaging experiments conducted at a fixed frequency and at two different amplitudes).

In conclusion, the results of this thesis demonstrate the potential of a hybrid MPI-MFH system as an alternative thermal ablation treatment approach. In such systems, simultaneous temperature and viscosity mapping by performing two imaging experiments could yield the information of the region and size of the cancerous tissues via viscosity mapping, and enable accurate adjustment of the thermal dose via temperature mapping.

7.2 Future Work

The relaxation behavior of the SPION response is highly dependent on the applied magnetic field. In this thesis, the imaging experiments were conducted using an in-house MPI scanner, and SPION characterization was performed using an in-house MPS setup. The only difference between these setups is the selection field in the MPI scanner that is generated by the magnets for spatial encoding. Although the estimated relaxation time constants using SPION response from both of these setups provided similar dependencies on the environmental conditions such as viscosity, these similar trends were observed at a higher frequency range in the MPI experiments. Understanding the reasons behind the frequency shift due to the additional DC magnetic field requires further investigation. One possible approach would be estimating the relaxation time constant in the MPS signal under additional DC magnetic field that is

parallel or perpendicular to the drive field.

The in-house MPS setup used in this thesis has an arbitrary waveform characteristic, so that the analysis of the SPION relaxation can be performed at a wide range of operating points without any capacitive circuitry. Although such designs can be easily constructed for small-sized MPS setups that already have relatively low drive coil inductance, the drive coil of the developed MPI scanner is larger in size to accommodate space for two dimensional scanning. In spite of the fact that an arbitrary waveform MPI scanner would provide very useful information on SPION relaxation, reducing the drive coil inductance to sufficiently low levels would pose a hardware challenge. To overcome such a problem, one could design the drive coil either with a shorter bore length, which would shrink the size of the homogeneous region, or alternatively with different winding types such as Rutherford pattern so that the coil has lower inductance.

The commercial SPIONs used in this thesis had multi-core clusters. In an *in vivo* measurement, the internalization of the SPIONs into tissues or cells may be size-selective. The core diameter of the SPIONs has a substantial effect on the relaxation behavior. Therefore, whether similar trends in TAURUS are valid for single core SPIONs with different core diameters or for selectively internalized SPIONs remains to be investigated as a future work.

Bibliography

[1] World Health Organization, "Cancer," 2020.

[2] C. P. Wild, E. Weiderpass, and B. W. Stewart, "World Cancer Report: Cancer research for cancer prevention," tech. rep., World Health Organization, Lyon, 2020.

[3] The Global Cancer Observatory, "Turkey," 2021.

[4] I. Corcuera-Solano, M. Wagner, and B. Taouli, "Imaging of Cancer Patients," in *Mount Sinai Expert Guides*, pp. 447–453, Wiley, Sep 2019.

[5] J. V. Frangioni, "New Technologies for Human Cancer Imaging," *Journal of Clinical Oncology*, vol. 26, pp. 4012–4021, Aug 2008.

[6] S. Adler, J. Seidel, P. Choyke, M. V. Knopp, K. Binzel, J. Zhang, C. Barker, S. Conant, and R. Maass-Moreno, "Minimum lesion detectability as a measure of PET system performance," *EJNMMI Physics*, vol. 4, p. 13, Dec 2017.

[7] M. M. Khalil, J. L. Tremoleda, T. B. Bayomy, and W. Gsell, "Molecular SPECT Imaging: An Overview," *International Journal of Molecular Imaging*, vol. 2011, no. 796025, pp. 1–15, 2011.

[8] H. Ryu, E. Eslick, K. P. Willowson, S. R. Meikle, and D. L. Bailey, "Performance Evaluation of Quantitative SPECT/CT: Applying NEMA NU2 PET Measurements to SPECT," in *IEEE Nuclear Science Symposium and Medical Imaging Conference (NSS/MIC)*, pp. 1–2, IEEE, Oct 2017.

[9] D. Stucht, K. A. Danishad, P. Schulze, F. Godenschweger, M. Zaitsev, and O. Speck, "Highest Resolution In Vivo Human Brain MRI Using Prospective Motion Correction," *PLOS ONE*, vol. 10, p. e0133921, Jul 2015.

[10] B. Gleich and J. Weizenecker, "Tomographic imaging using the nonlinear response of magnetic particles," *Nature*, vol. 435, pp. 1214–1217, Jun 2005.

[11] M. Reinert, Schlachter, Bregy, Lönnfors, Vajtai, Bernau, T. Weitzel, Mordasini, Slotboom, Herrmann, Bogni, Hofmann, M. Reinert, and M. Frenz, "Metabolic pathway and distribution of superparamagnetic iron oxide nanoparticles: in vivo study," *International Journal of Nanomedicine*, vol. 6, p. 1793, Aug 2011.

[12] E. U. Saritas, P. W. Goodwill, L. R. Croft, J. J. Konkle, K. Lu, B. Zheng, and S. M. Conolly, "Magnetic Particle Imaging (MPI) for NMR and MRI researchers," *Journal of Magnetic Resonance*, vol. 229, pp. 116–126, Apr 2013.

[13] J. Weizenecker, B. Gleich, J. Rahmer, H. Dahnke, and J. Borgert, "Three-dimensional real-time in vivo magnetic particle imaging," *Physics in Medicine and Biology*, vol. 54, pp. L1–L10, Mar 2009.

[14] K. Lu, P. W. Goodwill, E. U. Saritas, B. Zheng, and S. M. Conolly, "Linearity and shift invariance for quantitative magnetic particle imaging," *IEEE transactions on medical imaging*, vol. 32, pp. 1565–75, Sep 2013.

[15] J. W. M. Bulte, P. Walczak, M. Janowski, K. M. Krishnan, H. Arami, A. Halkola, B. Gleich, and J. Rahmer, "Quantitative "Hot-Spot" Imaging of Transplanted Stem Cells Using Superparamagnetic Tracers and Magnetic Particle Imaging," *Tomography*, vol. 1, pp. 91–97, Dec 2015.

[16] B. Zheng, T. Vazin, P. W. Goodwill, A. Conway, A. Verma, E. Ulku Saritas, D. Schaffer, and S. M. Conolly, "Magnetic Particle Imaging tracks the long-term fate of in vivo neural cell implants with high image contrast," *Scientific Reports*, vol. 5, p. 14055, Nov 2015.

[17] B. Zheng, M. P. von See, E. Yu, B. Gunel, K. Lu, T. Vazin, D. V. Schaffer, P. W. Goodwill, and S. M. Conolly, "Quantitative Magnetic Particle Imaging Monitors the Transplantation, Biodistribution, and Clearance of Stem Cells In Vivo," *Theranostics*, vol. 6, no. 3, pp. 291–301, 2016.

[18] K. Them, J. Salamon, P. Szwargulski, S. Sequeira, M. G. Kaul, C. Lange, H. Ittrich, and T. Knopp, "Increasing the sensitivity for stem cell monitoring in system-function based magnetic particle imaging," *Physics in Medicine and Biology*, vol. 61, pp. 3279–3290, May 2016.

[19] P. Ludewig, N. Gdaniec, J. Sedlacik, N. D. Forkert, P. Szwargulski, M. Graeser, G. Adam, M. G. Kaul, K. M. Krishnan, R. M. Ferguson, A. P. Khandhar, P. Walczak, J. Fiehler, G. Thomalla, C. Gerloff, T. Knopp, and T. Magnus, "Magnetic Particle Imaging for Real-Time Perfusion Imaging in Acute Stroke," *ACS Nano*, vol. 11, pp. 10480–10488, Oct 2017.

[20] R. Orendorff, A. J. Peck, B. Zheng, S. N. Shirazi, R. Matthew Ferguson, A. P. Khandhar, S. J. Kemp, P. Goodwill, K. M. Krishnan, G. A. Brooks, D. Kaufer, and S. Conolly, "First in vivo traumatic brain injury imaging via magnetic particle imaging," *Physics in Medicine and Biology*, vol. 62, pp. 3501–3509, May 2017.

[21] X. Y. Zhou, K. E. Jeffris, E. Y. Yu, B. Zheng, P. W. Goodwill, P. Nahid, and S. M. Conolly, "First in vivo magnetic particle imaging of lung perfusion in rats," *Physics in Medicine and Biology*, vol. 62, pp. 3510–3522, May 2017.

[22] J. Haegele, J. Rahmer, B. Gleich, J. Borgert, H. Wojtczyk, N. Panagiotopoulos, T. M. Buzug, J. Barkhausen, and F. M. Vogt, "Magnetic Particle Imaging: Visualization of Instruments for Cardiovascular Intervention," *Radiology*, vol. 265, pp. 933–938, Dec 2012.

[23] R. Duschka, H. Wojtczyk, N. Panagiotopoulos, J. Haegele, G. Bringout, T. Buzug, J. Barkhausen, and F. Vogt, "Safety Measurements for Heating of Instruments for Cardiovascular Interventions in Magnetic Particle Imaging (MPI) - First Experiences," *Journal of Healthcare Engineering*, vol. 5, pp. 79–94, Mar 2014.

[24] J. Haegele, N. Panagiotopoulos, S. Cremers, J. J. Rahmer, J. Franke, R. L. Duschka, S. Vaalma, M. Heidenreich, J. J. Borgert, P. Borm, J. J. Barkhausen, and F. M. Vogt, "Magnetic Particle Imaging: A Resovist Based Marking Technology for Guide Wires and Catheters for Vascular Interventions," *IEEE Transactions on Medical Imaging*, vol. 35, pp. 2312–2318, Oct 2016.

[25] D. Pantke, F. Mueller, S. Reinartz, F. Kiessling, and V. Schulz, "Flow velocity quantification by exploiting the principles of the Doppler effect and magnetic particle imaging," *Scientific Reports*, vol. 11, p. 4529, Dec 2021.

[26] E. E. Mason, C. Z. Cooley, S. F. Cauley, M. A. Griswold, S. M. Conolly, and L. L. Wald, "Design analysis of an MPI human functional brain scanner," *International journal on magnetic particle imaging*, vol. 3, no. 1, 2017.

[27] C. Z. Cooley, J. B. Mandeville, E. E. Mason, E. T. Mandeville, and L. L. Wald, "Rodent Cerebral Blood Volume (CBV) changes during hypercapnia observed using Magnetic Particle Imaging (MPI) detection," *NeuroImage*, vol. 178, pp. 713–720, Sep 2018.

[28] E. Y. Yu, M. Bishop, B. Zheng, R. M. Ferguson, A. P. Khandhar, S. J. Kemp, K. M. Krishnan, P. W. Goodwill, and S. M. Conolly, "Magnetic Particle Imaging: A Novel in Vivo Imaging Platform for Cancer Detection," *Nano Letters*, vol. 17, pp. 1648–1654, Mar 2017.

[29] H. Arami, E. Teeman, A. Troksa, H. Bradshaw, K. Saatchi, A. Tomitaka, S. S. Gambhir, U. O. Häfeli, D. Liggitt, and K. M. Krishnan, "Tomographic magnetic particle imaging of cancer targeted nanoparticles," *Nanoscale*, vol. 9, pp. 18723–18730, Dec 2017.

[30] P. W. Goodwill and L. R. Croft, "A 7 T/m 3D X-space MPI mouse and rat scanner," in *3rd International Workshop on Magnetic Particle Imaging (IWMPI)*, vol. 1, (Berkeley), 2013.

[31] K. Murase, T. Konishi, Y. Takeuchi, H. Takata, and S. Saito, "Experimental and simulation studies on the behavior of signal harmonics in magnetic particle imaging," *Radiological physics and technology*, vol. 6, pp. 399–414, Jul 2013.

[32] P. Vogel, M. A. Ruckert, P. Klauer, W. H. Kullmann, P. M. Jakob, and V. C. Behr, "Traveling Wave Magnetic Particle Imaging," *IEEE Transactions on Medical Imaging*, vol. 33, pp. 400–407, Feb 2014.

[33] G. Bringout, J. Stelzner, M. Ahlborg, A. Behrends, K. Bente, C. Debbeler, A. von Gladiss, K. Grafe, M. Graeser, C. Kaethner, S. Kaufmann, K. Ludtke-Buzug, H. Medimagh, W. Tenner, M. Weber, and T. M. Buzug, "Concept of a

rabbit-sized FFL-scanner," in *5th International Workshop on Magnetic Particle Imaging (IWMPI)*, pp. 1–1, IEEE, Mar 2015.

[34] J. Folkman, "The Vascularization of Tumors," *Scientific American*, vol. 234, no. 5, pp. 58–73, 1976.

[35] A. K. Iyer, G. Khaled, J. Fang, and H. Maeda, "Exploiting the enhanced permeability and retention effect for tumor targeting," *Drug Discovery Today*, vol. 11, pp. 812–818, Sep 2006.

[36] J. Kydd, R. Jadia, P. Velpurisiva, A. Gad, S. Paliwal, and P. Rai, "Targeting Strategies for the Combination Treatment of Cancer Using Drug Delivery Systems," *Pharmaceutics*, vol. 9, p. 46, Oct 2017.

[37] H. Nejadnik, S.-M. Taghavi-Garmestani, S. J. Madsen, K. Li, S. Zanganeh, P. Yang, M. Mahmoudi, and H. E. Daldrup-Link, "The Protein Corona around Nanoparticles Facilitates Stem Cell Labeling for Clinical MR Imaging," *Radiology*, vol. 286, pp. 938–947, Mar 2018.

[38] A. V. Makela, J. M. Gaudet, and P. J. Foster, "Quantifying tumor associated macrophages in breast cancer: a comparison of iron and fluorine-based MRI cell tracking," *Scientific Reports*, vol. 7, p. 42109, Feb 2017.

[39] A. S. Arbab, G. T. Yocum, H. Kalish, E. K. Jordan, S. A. Anderson, A. Y. Khakoo, E. J. Read, and J. A. Frank, "Efficient magnetic cell labeling with protamine sulfate complexed to ferumoxides for cellular MRI," *Blood*, vol. 104, pp. 1217–1223, Aug 2004.

[40] W. Liu and J. A. Frank, "Detection and quantification of magnetically labeled cells by cellular MRI," *European Journal of Radiology*, vol. 70, pp. 258–264, May 2009.

[41] B. Addicott, M. Willman, J. Rodriguez, K. Padgett, D. Han, D. Berman, J. M. Hare, and N. S. Kenyon, "Mesenchymal stem cell labeling and in vitro MR characterization at 1.5 T of new SPIO contrast agent: Molday ION Rhodamine-B," *Contrast Media and Molecular Imaging*, vol. 6, pp. 7–18, Jan 2011.

[42] A. Y. Sheu, Z. Zhang, R. A. Omary, and A. C. Larson, "MRI-Monitored Transcatheter Intra-Arterial Delivery of SPIO-Labeled Natural Killer Cells to Hepatocellular Carcinoma," *Investigative Radiology*, vol. 48, pp. 492–499, Jun 2013.

[43] K. D. Brewer, K. Lake, N. Pelot, M. M. Stanford, D. R. DeBay, A. Penwell, G. M. Weir, M. Karkada, M. Mansour, and C. V. Bowen, "Clearance of depot vaccine SPIO-labeled antigen and substrate visualized using MRI," *Vaccine*, vol. 32, pp. 6956–6962, Dec 2014.

[44] S. Zanganeh, G. Hutter, R. Spitler, O. Lenkov, M. Mahmoudi, A. Shaw, J. S. Pajarinen, H. Nejadnik, S. Goodman, M. Moseley, L. M. Coussens, and H. E. Daldrup-Link, "Iron oxide nanoparticles inhibit tumour growth by inducing pro-inflammatory macrophage polarization in tumour tissues," *Nature Nanotechnology*, vol. 11, pp. 986–994, Nov 2016.

[45] A. V. Makela, J. M. Gaudet, M. A. Schott, O. C. Sehl, C. H. Contag, and P. J. Foster, "Magnetic Particle Imaging of Macrophages Associated with Cancer: Filling the Voids Left by Iron-Based Magnetic Resonance Imaging," *Molecular Imaging and Biology*, vol. 22, pp. 958–968, Aug 2020.

[46] N.-K. Chen, C. C. Dickey, S.-S. Yoo, C. R. Guttmann, and L. P. Panych, "Selection of voxel size and slice orientation for fMRI in the presence of susceptibility field gradients: application to imaging of the amygdala," *NeuroImage*, vol. 19, pp. 817–825, Jul 2003.

[47] S. Robinson, C. Windischberger, A. Rauscher, and E. Moser, "Optimized 3 T EPI of the amygdalae," *NeuroImage*, vol. 22, pp. 203–210, May 2004.

[48] C. A. Olman, L. Davachi, and S. Inati, "Distortion and Signal Loss in Medial Temporal Lobe," *PLoS ONE*, vol. 4, p. e8160, Dec 2009.

[49] B. Zheng, E. Yu, R. Orendorff, K. Lu, J. J. Konkle, Z. W. Tay, D. Hensley, X. Y. Zhou, P. Chandrasekharan, E. U. Saritas, P. W. Goodwill, J. D. Hazle, and S. M. Conolly, "Seeing SPIOs Directly In Vivo with Magnetic Particle Imaging," *Molecular Imaging and Biology*, vol. 19, pp. 385–390, Jun 2017.

[50] O. C. Sehl, A. V. Makela, A. M. Hamilton, and P. J. Foster, "Trimodal Cell Tracking In Vivo: Combining Iron- and Fluorine-Based Magnetic Resonance Imaging with Magnetic Particle Imaging to Monitor the Delivery of Mesenchymal Stem Cells and the Ensuing Inflammation," *Tomography*, vol. 5, pp. 367–376, Dec 2019.

[51] L. Néel, "Théorie du traînage magnétique des ferromagnétiques en grains fins avec application aux terres cuites," *Annales de Géophysique*, vol. 5, no. 2, pp. 99–136, 1949.

[52] W. F. Brown, "Thermal Fluctuations of a Single-Domain Particle," *Physical Review*, vol. 130, pp. 1677–1686, Jun 1963.

[53] M. Martsenyuk, Y. L. Raikher, and M. I. Shliomis, "On the kinetics of magnetization of suspensions of ferromagnetic particles," *Soviet Journal of Experimental and Theoretical Physics*, vol. 38, no. 2, p. 413, 1974.

[54] M. I. Shliomis, "Magnetic fluids," *Soviet Physics - Uspekhi*, vol. 17, pp. 153–169, Feb 1974.

[55] W. T. Coffey, D. S. F. Crothers, Y. P. Kalmykov, and J. T. Waldron, "Constant-magnetic-field effect in Néel relaxation of single-domain ferromagnetic particles," *Physical Review B*, vol. 51, pp. 15947–15956, Jun 1995.

[56] D. Hensley, P. Goodwill, L. Croft, S. Conolly, and S. Connoly, "Preliminary experimental X-space color MPI," in *5th International Workshop on Magnetic Particle Imaging (IWMPI)*, vol. 29, (Istanbul), pp. 1–1, IEEE, Mar 2015.

[57] J. Rahmer, A. Halkola, B. Gleich, I. Schmale, and J. Borgert, "First experimental evidence of the feasibility of multi-color magnetic particle imaging," *Physics in Medicine and Biology*, vol. 60, pp. 1775–1791, Mar 2015.

[58] M. Möddel, C. Meins, J. Dieckhoff, and T. Knopp, "Viscosity quantification using multi-contrast magnetic particle imaging," *New Journal of Physics*, vol. 20, p. 083001, Aug 2018.

[59] A. M. Rauwerdink and J. B. Weaver, "Viscous effects on nanoparticle magnetization harmonics," *Journal of Magnetism and Magnetic Materials*, vol. 322, pp. 609–613, Mar 2010.

[60] M. Utkur, Y. Muslu, and E. U. Saritas, "Relaxation-based viscosity mapping for magnetic particle imaging," *Physics in Medicine and Biology*, vol. 62, pp. 3422–3439, May 2017.

[61] W. L. Chandler and G. Schmer, "Evaluation of a new dynamic viscometer for measuring the viscosity of whole blood and plasma," *Clinical chemistry*, vol. 32, pp. 505–7, Mar 1986.

[62] G. Deliconstantinos, V. Villiotou, and C. J. Stavrides, "Modulation of particulate nitric oxide synthase activity and peroxynitrite synthesis in cholesterol enriched endothelial cell membranes," *Biochem Pharmacol*, vol. 49, no. 11, pp. 1589–1600, 1995.

[63] G.-F. von Tempelhoff, N. Schönmann, L. Heilmann, K. Pollow, and G. Hommel, "Prognostic role of plasmaviscosity in breast cancer," *Clinical hemorheology and microcirculation*, vol. 26, no. 1, pp. 55–61, 2002.

[64] J. Murray and A. C. Tree, "Prostate cancer - Advantages and disadvantages of MR-guided RT," *Clinical and Translational Radiation Oncology*, vol. 18, pp. 68–73, Sep 2019.

[65] P. Wust, B. Hildebrandt, G. Sreenivasa, B. Rau, J. Gellermann, H. Riess, R. Felix, and P. Schlag, "Hyperthermia in combined treatment of cancer," *The Lancet Oncology*, vol. 3, pp. 487–497, Aug 2002.

[66] S. A. Curley, "Radiofrequency Ablation of Malignant Liver Tumors," *Annals of Surgical Oncology*, vol. 10, pp. 338–347, Jan 2003.

[67] B. Hildebrandt and P. Wust, "The Biologic Rationale of Hyperthermia," in *Peritoneal Carcinomatosis*, vol. 134, pp. 171–184, Boston, MA: Springer US, 2007.

[68] C. A. Arciero and E. R. Sigurdson, "Diagnosis and Treatment of Metastatic Disease to the Liver," *Seminars in Oncology*, vol. 35, pp. 147–159, Apr 2008.

[69] W. Rao, Z.-S. Deng, and J. Liu, "A Review of Hyperthermia Combined With Radiotherapy/Chemotherapy on Malignant Tumors," *Critical Reviews in Biomedical Engineering*, vol. 38, no. 1, pp. 101–116, 2010.

[70] L. J. Anghileri and J. Robert, *Hyperthermia in cancer treatment. Volume II*. CRC Press, 2019.

[71] G. F. Baronzio and E. D. Hager, *Hyperthermia in Cancer Treatment: A Primer*. Springer, Lander Bioscience, 2006.

[72] H. E. Cline, K. Hynynen, R. D. Watkins, W. J. Adams, J. F. Schenck, R. H. Ettinger, W. R. Freund, J. P. Vetro, and F. A. Jolesz, "Focused US system for MR imaging-guided tumor ablation," *Radiology*, vol. 194, pp. 731–737, Mar 1995.

[73] J. Chapelon, M. Ribault, A. Birer, F. Vernier, R. Souchon, and A. Gelet, "Treatment of localised prostate cancer with transrectal high intensity focused ultrasound," *European Journal of Ultrasound*, vol. 9, pp. 31–38, Mar 1999.

[74] B. Quesson, J. A. de Zwart, and C. T. Moonen, "Magnetic resonance temperature imaging for guidance of thermotherapy," *Journal of Magnetic Resonance Imaging*, vol. 12, pp. 525–533, Oct 2000.

[75] P. E. Huber, J. W. Jenne, R. Rastert, I. Simiantonakis, H. P. Sinn, H. J. Strittmatter, D. von Fournier, M. F. Wannenmacher, and J. Debus, "A new noninvasive approach in breast cancer therapy using magnetic resonance imaging-guided focused ultrasound surgery," *Cancer research*, vol. 61, pp. 8441–7, Dec 2001.

[76] F. Chavrier, J. Y. Chapelon, A. Gelet, and D. Cathignol, "Modeling of high-intensity focused ultrasound-induced lesions in the presence of cavitation bubbles," *The Journal of the Acoustical Society of America*, vol. 108, pp. 432–440, Jul 2000.

[77] R. Salomir, A.-S. Delemazure, J. Palussière, O. Rouvière, F. Cotton, and J.-Y. Chapelon, "Image-Based Control of the Magnetic Resonance Imaging-Guided Focused Ultrasound Thermotherapy," *Topics in Magnetic Resonance Imaging*, vol. 17, pp. 139–151, Jun 2006.

[78] O. Fiser, M. Helbig, J. Sachs, S. Ley, I. Merunka, and J. Vrba, "Microwave Non-invasive Temperature Monitoring Using UWB Radar for Cancer Treatment by Hyperthermia," *Progress In Electromagnetics Research*, vol. 162, pp. 1–14, 2018.

[79] M. H. Manjili, X.-Y. Wang, J. Park, I. J. Macdonald, Y. Li, R. C. A. A. Van Schie, and J. R. Subjeck, "Cancer immunotherapy: stress proteins and hyperthermia," *International Journal of Hyperthermia*, vol. 18, pp. 506–520, Jan 2002.

[80] S. K. Calderwood, J. R. Theriault, and J. Gong, "How is the immune response affected by hyperthermia and heat shock proteins?," *International Journal of Hyperthermia*, vol. 21, pp. 713–716, Dec 2005.

[81] Y. Yagawa, K. Tanigawa, Y. Kobayashi, and M. Yamamoto, "Cancer immunity and therapy using hyperthermia with immunotherapy, radiotherapy, chemotherapy, and surgery," *Journal of Cancer Metastasis and Treatment*, vol. 3, p. 218, Oct 2017.

[82] A. Jordan, R. Scholz, P. Wust, H. Fähling, and Roland Felix, "Magnetic fluid hyperthermia (MFH): Cancer treatment with AC magnetic field induced excitation of biocompatible superparamagnetic nanoparticles," *Journal of Magnetism and Magnetic Materials*, vol. 201, pp. 413–419, Jul 1999.

[83] A. Jordan, P. Wust, H. Fählin, W. John, A. Hinz, and R. Felix, "Inductive heating of ferrimagnetic particles and magnetic fluids: Physical evaluation of their potential for hyperthermia," *International Journal of Hyperthermia*, vol. 9, pp. 51–68, Jan 1993.

[84] R. Hiergeist, W. Andrä, N. Buske, R. Hergt, I. Hilger, U. Richter, and W. Kaiser, "Application of magnetite ferrofluids for hyperthermia," *Journal of Magnetism and Magnetic Materials*, vol. 201, pp. 420–422, Jul 1999.

[85] H. Mamiya and B. Jeyadevan, "Hyperthermic effects of dissipative structures of magnetic nanoparticles in large alternating magnetic fields," *Scientific Reports*, vol. 1, Dec 2011.

[86] T. O. Tasci, I. Vargel, A. Arat, E. Guzel, P. Korkusuz, and E. Atalar, "Focused RF hyperthermia using magnetic fluids," *Medical Physics*, vol. 36, pp. 1906–1912, Apr 2009.

[87] A. Ohki, T. Kuboyabu, M. Aoki, M. Yamawaki, and K. Murase, "Quantitative Evaluation of Tumor Response to combination of Magnetic Hyperthermia Treatment and Radiation Therapy using Magnetic Particle Imaging," *Int J Nanomed Nanosurg*, vol. 2, no. 3, 2016.

[88] Z. W. Tay, P. Chandrasekharan, A. Chiu-Lam, D. W. Hensley, R. Dhavalikar, X. Y. Zhou, E. Y. Yu, P. W. Goodwill, B. Zheng, C. Rinaldi, and S. M. Conolly, "Magnetic Particle Imaging-Guided Heating in Vivo Using Gradient Fields for Arbitrary Localization of Magnetic Hyperthermia Therapy," *ACS Nano*, vol. 12, pp. 3699–3713, Apr 2018.

[89] A. Rivera-Rodriguez, L. B. Hoang-Minh, A. Chiu-Lam, N. Sarna, L. Marrero-Morales, D. A. Mitchell, and C. M. Rinaldi-Ramos, "Tracking adoptive T cell immunotherapy using magnetic particle imaging," *Nanotheranostics*, vol. 5, pp. 431–444, May 2021.

[90] D. Hensley, Z. W. Tay, R. Dhavalikar, B. Zheng, P. Goodwill, C. Rinaldi, and S. Conolly, "Combining magnetic particle imaging and magnetic fluid hyperthermia in a theranostic platform," *Physics in Medicine and Biology*, vol. 62, pp. 3483–3500, May 2017.

[91] P. Chandrasekharan, Z. W. Tay, D. Hensley, X. Y. Zhou, B. K. Fung, C. Colson, Y. Lu, B. D. Fellows, Q. Huynh, C. Saayujya, E. Yu, R. Orendorff, B. Zheng, P. Goodwill, C. Rinaldi, and S. Conolly, "Using magnetic particle imaging systems to localize and guide magnetic hyperthermia treatment: tracers, hardware, and future medical applications," *Theranostics*, vol. 10, no. 7, pp. 2965–2981, 2020.

[92] O. C. Farokhzad and R. Langer, "Impact of Nanotechnology on Drug Delivery," *ACS Nano*, vol. 3, pp. 16–20, Jan 2009.

[93] J. W. Baish, T. Stylianopoulos, R. M. Lanning, W. S. Kamoun, D. Fukumura, L. L. Munn, and R. K. Jain, "Scaling rules for diffusive drug delivery in tumor

and normal tissues," *Proceedings of the National Academy of Sciences*, vol. 108, pp. 1799–1803, Feb 2011.

[94] D. E. Bordelon, C. Cornejo, C. Grüttner, F. Westphal, T. L. DeWeese, and R. Ivkov, "Magnetic nanoparticle heating efficiency reveals magneto-structural differences when characterized with wide ranging and high amplitude alternating magnetic fields," *Journal of Applied Physics*, vol. 109, p. 124904, Jun 2011.

[95] K. L. Krycka, A. J. Jackson, J. A. Borchers, J. Shih, R. Briber, R. Ivkov, C. Grüttner, and C. L. Dennis, "Internal magnetic structure of dextran coated magnetite nanoparticles in solution using small angle neutron scattering with polarization analysis," *Journal of Applied Physics*, vol. 109, p. 07B513, Apr 2011.

[96] C. L. Dennis and R. Ivkov, "Physics of heat generation using magnetic nanoparticles for hyperthermia," *International Journal of Hyperthermia*, vol. 29, pp. 715–729, Dec 2013.

[97] R. Dhavalikar and C. Rinaldi, "Theoretical predictions for spatially-focused heating of magnetic nanoparticles guided by magnetic particle imaging field gradients," *Journal of Magnetism and Magnetic Materials*, vol. 419, pp. 267–273, Dec 2016.

[98] J. Sun, S. Zhou, P. Hou, Y. Yang, J. Weng, X. Li, and M. Li, "Synthesis and characterization of biocompatible Fe3O4 nanoparticles," *Journal of Biomedical Materials Research Part A*, vol. 80A, pp. 333–341, Feb 2007.

[99] A. Akbarzadeh, M. Samiei, and S. Davaran, "Magnetic nanoparticles: preparation, physical properties, and applications in biomedicine," *Nanoscale Research Letters*, vol. 7, p. 144, Feb 2012.

[100] Q.-h. Tian, W.-b. Ning, W.-j. Wang, X.-h. Yuan, and Z.-m. Bai, "Synthesis of size-controllable Fe3O4 magnetic submicroparticles and its biocompatible evaluation in vitro," *Journal of Central South University*, vol. 23, pp. 2784–2791, Nov 2016.

[101] R. C. Popescu, E. Andronescu, and B. S. Vasile, "Recent Advances in Magnetite Nanoparticle Functionalization for Nanomedicine," *Nanomaterials*, vol. 9, p. 1791, Dec 2019.

[102] P. M. Martins, A. C. Lima, S. Ribeiro, S. Lanceros-Mendez, and P. Martins, "Magnetic Nanoparticles for Biomedical Applications: From the Soul of the Earth to the Deep History of Ourselves," *ACS Applied Bio Materials*, p. acsabm.1c00440, Jul 2021.

[103] A. S. Thakor, J. V. Jokerst, P. Ghanouni, J. L. Campbell, E. Mittra, and S. S. Gambhir, "Clinically Approved Nanoparticle Imaging Agents," *Journal of Nuclear Medicine*, vol. 57, pp. 1833–1837, Dec 2016.

[104] A. A. Yetisgin, S. Cetinel, M. Zuvin, A. Kosar, and O. Kutlu, "Therapeutic Nanoparticles and Their Targeted Delivery Applications," *Molecules*, vol. 25, p. 2193, May 2020.

[105] N. Elahi and M. Rizwan, "Progress and prospects of magnetic iron oxide nanoparticles in biomedical applications: A review," *Artificial Organs*, p. aor.14027, Jul 2021.

[106] G. Kandasamy, A. Sudame, T. Luthra, K. Saini, and D. Maity, "Functionalized Hydrophilic Superparamagnetic Iron Oxide Nanoparticles for Magnetic Fluid Hyperthermia Application in Liver Cancer Treatment," *ACS Omega*, vol. 3, pp. 3991–4005, Apr 2018.

[107] P. Das, M. Colombo, and D. Prosperi, "Recent advances in magnetic fluid hyperthermia for cancer therapy," *Colloids and Surfaces B: Biointerfaces*, vol. 174, pp. 42–55, Feb 2019.

[108] J. Palzer, B. Mues, R. Goerg, M. Aberle, S. S. Rensen, S. W. Olde Damink, R. D. Vaes, T. Cramer, T. Schmitz-Rode, U. P. Neumann, I. Slabu, and A. A. Roeth, "Magnetic Fluid Hyperthermia as Treatment Option for Pancreatic Cancer Cells and Pancreatic Cancer Organoids," *International Journal of Nanomedicine*, vol. Volume 16, pp. 2965–2981, Apr 2021.

[109] M. Gogoi, "Magnetic Nanostructures for Cancer Theranostic Applications," *Current Pathobiology Reports*, pp. 1–8, Jul 2021.

[110] J. S. Weinstein, C. G. Varallyay, E. Dosa, S. Gahramanov, B. Hamilton, W. D. Rooney, L. L. Muldoon, and E. A. Neuwelt, "Superparamagnetic Iron Oxide

Nanoparticles: Diagnostic Magnetic Resonance Imaging and Potential Therapeutic Applications in Neurooncology and Central Nervous System Inflammatory Pathologies, a Review," *Journal of Cerebral Blood Flow and Metabolism*, vol. 30, pp. 15–35, Jan 2010.

[111] Y. X. J. Wáng and J.-M. Idée, "A comprehensive literatures update of clinical researches of superparamagnetic resonance iron oxide nanoparticles for magnetic resonance imaging," *Quantitative Imaging in Medicine and Surgery*, vol. 7, pp. 88–122, Feb 2017.

[112] J. Dulińska-Litewka, A. Łazarczyk, P. Hałubiec, O. Szafrański, K. Karnas, and A. Karewicz, "Superparamagnetic Iron Oxide Nanoparticles-Current and Prospective Medical Applications," *Materials*, vol. 12, p. 617, Feb 2019.

[113] R. Canese, F. Vurro, and P. Marzola, "Iron Oxide Nanoparticles as Theranostic Agents in Cancer Immunotherapy," *Nanomaterials*, vol. 11, p. 1950, Jul 2021.

[114] M. H. Pablico-Lansigan, S. F. Situ, and A. C. S. Samia, "Magnetic particle imaging: advancements and perspectives for real-time in vivo monitoring and image-guided therapy," *Nanoscale*, vol. 5, p. 4040, May 2013.

[115] J. W. Bulte, "Superparamagnetic iron oxides as MPI tracers: A primer and review of early applications," *Advanced Drug Delivery Reviews*, vol. 138, pp. 293–301, Jan 2019.

[116] L. Wu, Y. Zhang, G. Steinberg, H. Qu, S. Huang, M. Cheng, T. Bliss, F. Du, J. Rao, G. Song, L. Pisani, T. Doyle, S. Conolly, K. Krishnan, G. Grant, and M. Wintermark, "A Review of Magnetic Particle Imaging and Perspectives on Neuroimaging," *American Journal of Neuroradiology*, vol. 40, pp. 206–212, Feb 2019.

[117] N. Talebloo, M. Gudi, N. Robertson, and P. Wang, "Magnetic Particle Imaging: Current Applications in Biomedical Research," *Journal of Magnetic Resonance Imaging*, vol. 51, pp. 1659–1668, Jun 2020.

[118] T. Knopp and T. M. Buzug, *Magnetic Particle Imaging*, vol. 9783642041. Berlin, Heidelberg: Springer Berlin Heidelberg, Mar 2012.

[119] C. Shasha and K. M. Krishnan, "Nonequilibrium Dynamics of Magnetic Nanoparticles with Applications in Biomedicine," *Advanced Materials*, p. 1904131, Jun 2020.

[120] J. Rahmer, J. Weizenecker, B. Gleich, and J. Borgert, "Signal encoding in magnetic particle imaging: properties of the system function," *BMC Medical Imaging*, vol. 9, p. 4, Dec 2009.

[121] R. M. Ferguson, K. R. Minard, A. P. Khandhar, and K. M. Krishnan, "Optimizing magnetite nanoparticles for mass sensitivity in magnetic particle imaging," *Medical Physics*, vol. 38, pp. 1619–1626, Feb 2011.

[122] J. Weizenecker, B. Gleich, J. Rahmer, and J. Borgert, "Micro-magnetic simulation study on the magnetic particle imaging performance of anisotropic monodomain particles," *Physics in Medicine and Biology*, vol. 57, no. 22, pp. 7317–7327, 2012.

[123] D. Eberbeck, C. L. Dennis, N. F. Huls, K. L. Krycka, C. Gruttner, and F. Westphal, "Multicore Magnetic Nanoparticles for Magnetic Particle Imaging," *IEEE Transactions on Magnetics*, vol. 49, pp. 269–274, Jan 2013.

[124] H. Arami, R. M. Ferguson, A. P. Khandhar, and K. M. Krishnan, "Size-dependent ferrohydrodynamic relaxometry of magnetic particle imaging tracers in different environments," *Medical Physics*, vol. 40, p. 071904, Jun 2013.

[125] R. Hufschmid, H. Arami, R. M. Ferguson, M. Gonzales, E. Teeman, L. N. Brush, N. D. Browning, and K. M. Krishnan, "Synthesis of phase-pure and monodisperse iron oxide nanoparticles by thermal decomposition," *Nanoscale*, vol. 7, pp. 11142–11154, Jul 2015.

[126] M. Graeser, K. Bente, A. Neumann, and T. M. Buzug, "Trajectory dependent particle response for anisotropic mono domain particles in magnetic particle imaging," *Journal of Physics D: Applied Physics*, vol. 49, no. 4, p. 045007, 2016.

[127] A. P. Khandhar, P. Keselman, S. J. Kemp, R. M. Ferguson, P. W. Goodwill, S. M. Conolly, and K. M. Krishnan, "Evaluation of PEG-coated iron oxide nanoparticles as blood pool tracers for preclinical magnetic particle imaging," *Nanoscale*, vol. 9, pp. 1299–1306, Jan 2017.

[128] A. Tomitaka, S. Ota, K. Nishimoto, H. Arami, Y. Takemura, and M. Nair, "Dynamic magnetic characterization and magnetic particle imaging enhancement of magnetic-gold core-shell nanoparticles," *Nanoscale*, vol. 11, no. 13, pp. 6489–6496, 2019.

[129] P. W. Goodwill and S. M. Conolly, "The X-Space Formulation of the Magnetic Particle Imaging Process: 1-D Signal, Resolution, Bandwidth, SNR, SAR, and Magnetostimulation," *IEEE Transactions on Medical Imaging*, vol. 29, pp. 1851–1859, Nov 2010.

[130] P. W. Goodwill and S. M. Conolly, "Multidimensional X-Space Magnetic Particle Imaging," *IEEE Transactions on Medical Imaging*, vol. 30, pp. 1581–1590, Sep 2011.

[131] T. Knopp, T. Sattel, S. Biederer, J. Rahmer, J. Weizenecker, B. Gleich, J. Borgert, and T. Buzug, "Model-Based Reconstruction for Magnetic Particle Imaging," *IEEE Transactions on Medical Imaging*, vol. 29, pp. 12–18, Jan 2010.

[132] R. Rosensweig, "Heating magnetic fluid with alternating magnetic field," *Journal of Magnetism and Magnetic Materials*, vol. 252, pp. 370–374, Nov 2002.

[133] Y. L. Raikher and M. I. Shliomis, "The Effective Field Method in the Orientational Kinetics of Magnetic Fluids and Liquid Crystals," in *Relaxation Phenomena in Condensed Matter* (W. Coffey, ed.), ch. 8, pp. 595–751, John Wiley and Sons, Ltd, Mar 2007.

[134] W. T. Coffey, P. J. Cregg, and Y. U. P. Kalmykov, "On the Theory of Debye and Néel Relaxation of Single Domain Ferromagnetic Particles," in *Advances in Chemical Physics*, vol. LXXXIII, pp. 263–464, John Wiley and Sons, Inc, Mar 2007.

[135] A. Aharoni, "Effect of a Magnetic Field on the Superparamagnetic Relaxation Time," *Physical Review*, vol. 177, pp. 793–796, Jan 1969.

[136] P. Debye, "Part I. Dielectric constant. Energy absorption in dielectrics with polar molecules," *Transactions of the Faraday Society*, vol. 30, p. 679, 1934.

[137] M. Shliomis and Y. Raikher, "Experimental investigations of magnetic fluids," *IEEE Transactions on Magnetics*, vol. 16, pp. 237–250, Mar 1980.

[138] P. C. Fannin, "Wideband Measurement and Analysis Techniques for the Determination of the Frequency-Dependent, Complex Susceptibility of Magnetic Fluids," in *Advances in Chemical Physics*, pp. 181–292, John Wiley and Sons, Ltd, Mar 2007.

[139] D. V. Berkov and N. L. Gorn, "Susceptibility of the disordered system of fine magnetic particles: a Langevin-dynamics study," *Journal of Physics: Condensed Matter*, vol. 13, pp. 9369–9381, Oct 2001.

[140] S. Ota, S. B. Trisnanto, S. Takeuchi, J. Wu, Y. Cheng, and Y. Takemura, "Quantitation method of loss powers using commercial magnetic nanoparticles based on superparamagnetic behavior influenced by anisotropy for hyperthermia," *Journal of Magnetism and Magnetic Materials*, vol. 538, p. 168313, Nov 2021.

[141] L. R. Croft, P. W. Goodwill, and S. M. Conolly, "Relaxation in X-Space Magnetic Particle Imaging," *IEEE Transactions on Medical Imaging*, vol. 31, pp. 2335–2342, Dec 2012.

[142] Y. Muslu, M. Utkur, O. B. Demirel, and E. U. Saritas, "Calibration-Free relaxation-based multi-color magnetic particle imaging," *IEEE Transactions on Medical Imaging*, vol. 37, pp. 1920–1931, Aug 2018.

[143] M. Utkur, Y. Muslu, and E. Saritas, "Relaxation-based color magnetic particle imaging for viscosity mapping," *Applied Physics Letters*, vol. 115, Oct 2019.

[144] M. Utkur, A. Alipour, Y. Muslu, and E. U. Saritas, "Relaxation-Based Viscosity Mapping in Different Viscous Environments," in *7th International Workshop on Magnetic Particle Imaging (IWMPI)*, (Prague), p. 137, 2017.

[145] M. Utkur and E. U. Saritas, "Comparison of different coil topologies for an MPI relaxometer," in *5th International Workshop on Magnetic Particle Imaging (IWMPI)*, (Istanbul), p. 1, 2015.

[146] H. A. Wheeler, "Formulas for the Skin Effect," *Proceedings of the IRE*, vol. 30, pp. 412–424, Sep 1942.

[147] E. Bozkurt and E. U. Saritas, "Signal-to-noise ratio optimized image reconstruction technique for magnetic particle imaging," *Journal of the Faculty of Engineering and Architecture of Gazi University*, vol. 32, pp. 999–1013, Sep 2017.

[148] M. K. Kuimova, S. W. Botchway, A. W. Parker, M. Balaz, H. A. Collins, H. L. Anderson, K. Suhling, and P. R. Ogilby, "Imaging intracellular viscosity of a single cell during photoinduced cell death," *Nature Chemistry*, vol. 1, pp. 69–73, Apr 2009.

[149] B. Pirofsky, "The determination of blood viscosity in man by a method based on Poiseuille's law," *The Journal of clinical investigation*, vol. 32, pp. 292–298, Apr 1953.

[150] M. Utkur, Y. Muslu, and E. U. Saritas, "A 4.8 T/m Magnetic Particle Imaging Scanner Design and Construction," in *21st National Biomedical Engineering Meeting (BIYOMUT)*, (Istanbul), IEEE, Nov 2017.

[151] A. P. Khandhar, R. M. Ferguson, H. Arami, and K. M. Krishnan, "Monodisperse magnetite nanoparticle tracers for in vivo magnetic particle imaging," *Biomaterials*, vol. 34, pp. 3837–3845, May 2013.

[152] A. Weber, J. Weizenecker, J. Rahmer, J. Franke, U. Heinen, and T. Buzug, "Resolution improvement by decreasing the drive field amplitude," in *5th International Workshop on Magnetic Particle Imaging (IWMPI)*, (Istanbul), pp. 1–1, IEEE, Mar 2015.

[153] L. R. Croft, P. W. Goodwill, J. J. Konkle, H. Arami, D. A. Price, A. X. Li, E. U. Saritas, and S. M. Conolly, "Low drive field amplitude for improved image resolution in magnetic particle imaging," *Medical Physics*, vol. 43, pp. 424–435, Dec 2015.

[154] A. Alipour, Z. Soran-Erdem, M. Utkur, V. K. Sharma, O. Algin, E. U. Saritas, and H. V. Demir, "A new class of cubic SPIONs as a dual-mode T1 and T2

contrast agent for MRI," *Magnetic Resonance Imaging*, vol. 49, pp. 16–24, Jun 2018.

[155] R. Dhavalikar, A. C. Bohórquez, and C. Rinaldi, "Image-Guided Thermal Therapy Using Magnetic Particle Imaging and Magnetic Fluid Hyperthermia," in *Nanomaterials for Magnetic and Optical Hyperthermia Applications* (R. M. Fratila and J. M. D. L. Fuente, eds.), Micro and Nano Technologies, pp. 265–286, Elsevier, 2019.

[156] R. J. Deissler and M. A. Martens, "Dependence of the Magnetization Response on the Driving Field Amplitude for Magnetic Particle Imaging and Spectroscopy," *IEEE Transactions on Magnetics*, vol. 51, Feb 2015.

[157] Z. W. Tay, D. Hensley, J. Ma, P. Chandrasekharan, B. Zheng, P. Goodwill, and S. Conolly, "Pulsed Excitation in Magnetic Particle Imaging," *IEEE Transactions on Medical Imaging*, vol. 38, pp. 2389–2399, Oct 2019.

[158] M. Graeser, T. Knopp, P. Szwargulski, T. Friedrich, A. von Gladiss, M. Kaul, K. M. Krishnan, H. Ittrich, G. Adam, and T. M. Buzug, "Towards Picogram Detection of Superparamagnetic Iron-Oxide Particles Using a Gradiometric Receive Coil," *Scientific Reports*, vol. 7, p. 6872, Dec 2017.

[159] B. Gleich, *Principles and Applications of Magnetic Particle Imaging*. Wiesbaden: Springer Fachmedien Wiesbaden, 2014.

[160] Z. W. Tay, P. Chandrasekharan, X. Y. Zhou, E. Yu, B. Zheng, and S. Conolly, "In vivo tracking and quantification of inhaled aerosol using magnetic particle imaging towards inhaled therapeutic monitoring," *Theranostics*, vol. 8, no. 13, pp. 3676–3687, 2018.

[161] E. Myrovali, N. Maniotis, T. Samaras, and M. Angelakeris, "Spatial focusing of magnetic particle hyperthermia," *Nanoscale Advances*, vol. 2, pp. 408–416, Jan 2020.

[162] K. Murase, M. Aoki, N. Banura, K. Nishimoto, A. Mimura, T. Kuboyabu, and I. Yabata, "Usefulness of Magnetic Particle Imaging for Predicting the Therapeutic Effect of Magnetic Hyperthermia," *Open Journal of Medical Imaging*, vol. 05, no. 02, pp. 85–99, 2015.

[163] J. B. Weaver, A. M. Rauwerdink, and E. W. Hansen, "Magnetic nanoparticle temperature estimation," *Medical Physics*, vol. 36, pp. 1822–1829, Apr 2009.

[164] A. M. Rauwerdink, E. W. Hansen, and J. B. Weaver, "Nanoparticle temperature estimation in combined ac and dc magnetic fields," *Physics in Medicine and Biology*, vol. 54, p. 51, Sep 2009.

[165] I. M. Perreard, D. B. Reeves, X. Zhang, E. Kuehlert, E. R. Forauer, and J. B. Weaver, "Temperature of the magnetic nanoparticle microenvironment: estimation from relaxation times," *Physics in Medicine and Biology*, vol. 59, pp. 1109–1119, Mar 2014.

[166] J. Zhong, M. Schilling, and F. Ludwig, "Excitation frequency dependence of temperature resolution in magnetic nanoparticle temperature imaging with a scanning magnetic particle spectrometer," *Journal of Magnetism and Magnetic Materials*, vol. 471, pp. 340–345, Feb 2019.

[167] C. Stehning, B. Gleich, J. Rahmer, ·. B. Gleich, and J. Rahmer, "Simultaneous magnetic particle imaging (MPI) and temperature mapping using multi-color MPI," *International Journal on Magnetic Particle Imaging*, vol. 2, pp. 1–6, Dec 2016.

[168] J. Salamon, J. Dieckhoff, M. G. Kaul, C. Jung, G. Adam, M. Möddel, T. Knopp, S. Draack, F. Ludwig, and H. Ittrich, "Visualization of spatial and temporal temperature distributions with magnetic particle imaging for liver tumor ablation therapy," *Scientific Reports*, vol. 10, p. 7480, Dec 2020.

[169] S. Draack, M. Schilling, and T. Viereck, "Magnetic particle imaging of particle dynamics in complex matrix systems," *Physical Sciences Reviews*, Feb 2021.

[170] X. Zhang, "A surface wave elastography technique for measuring tissue viscoelastic properties," *Medical Engineering and Physics*, vol. 42, pp. 111–115, Apr 2017.

[171] J. B. Segur and H. E. Oberstar, "Viscosity of Glycerol and Its Aqueous Solutions," *Industrial and Engineering Chemistry*, vol. 43, pp. 2117–2120, Sep 1951.

[172] Z. W. Tay, P. W. Goodwill, D. W. Hensley, L. A. Taylor, B. Zheng, and S. M. Conolly, "A High-Throughput, Arbitrary-Waveform, MPI Spectrometer and Relaxometer for Comprehensive Magnetic Particle Optimization and Characterization," *Scientific Reports*, vol. 6, p. 34180, Sep 2016.

[173] C. B. Top, "An arbitrary waveform magnetic nanoparticle relaxometer with an asymmetrical three-section gradiometric receive coil," *Turkish Journal of Electrical Engineering and Computer Sciences*, vol. 28, pp. 1344–1354, May 2020.

[174] T. Wawrzik, F. Ludwig, and M. Schilling, "Magnetic Particle Imaging: Exploring Particle Mobility," in *Magnetic Particle Imaging: A Novel SPIO Nanoparticle Imaging Technique* (T. M. Buzug and J. Borgert, eds.), vol. 140, pp. 21–25, Berlin, Heidelberg: Springer Berlin Heidelberg, 2012.

[175] J. Dieckhoff, D. Eberbeck, M. Schilling, and F. Ludwig, "Magnetic-field dependence of Brownian and Néel relaxation times," *Journal of Applied Physics*, vol. 119, p. 043903, Jan 2016.

[176] S. Ota, R. Kitaguchi, R. Takeda, T. Yamada, and Y. Takemura, "Rotation of Magnetization Derived from Brownian Relaxation in Magnetic Fluids of Different Viscosity Evaluated by Dynamic Hysteresis Measurements over a Wide Frequency Range," *Nanomaterials*, vol. 6, p. 170, Sep 2016.

[177] T. Viereck, C. Kuhlmann, S. Draack, M. Schilling, and F. Ludwig, "Dual-frequency magnetic particle imaging of the Brownian particle contribution," *Journal of Magnetism and Magnetic Materials*, vol. 427, pp. 156–161, Apr 2017.

[178] V. Rieke and K. Butts Pauly, "MR thermometry," *Journal of Magnetic Resonance Imaging*, vol. 27, pp. 376–390, Feb 2008.

[179] J. Yin, X. Kong, and W. Lin, "Noninvasive Cancer Diagnosis In Vivo Based on a Viscosity-Activated Near-Infrared Fluorescent Probe," *Analytical Chemistry*, vol. 93, pp. 2072–2081, Feb 2021.

[180] A. Wiedenmann, R. Gähler, C. D. Dewhurst, U. Keiderling, S. Prévost, and J. Kohlbrecher, "Relaxation mechanisms in magnetic colloids studied by stroboscopic spin-polarized small-angle neutron scattering," *Physical Review B*, vol. 84, p. 214303, Dec 2011.

[181] Â. L. Andrade, L. C. D. Cavalcante, J. D. Fabris, M. C. Pereira, L. E. Fernandez-Outon, D. C. Pedersoli, J. D. Ardisson, R. Z. Domingues, and J. M. Ferreira, "Magnetically induced heating by iron oxide nanoparticles dispersed in liquids of different viscosities," *Ceramics International*, vol. 46, pp. 21496–21504, Sep 2020.

[182] E. Pardo, M. Staines, Z. Jiang, and N. Glasson, "Ac loss modelling and measurement of superconducting transformers with coated-conductor roebel-cable in low-voltage winding," *Superconductor Science and Technology*, vol. 28, p. 114008, 11 2015.

[183] A. A. Ozaslan, A. R. Cagil, M. Graeser, T. Knopp, and E. U. Saritas, "Design of a Magnetostimulation Head Coil with Rutherford Cable Winding," in *International Journal on Magnetic Particle Imaging*, vol. 6, pp. 1–3, Infinite Science Publishing, Sep 2020.

[184] B. Tasdelen, M. Utkur, E. Atalar, and E. U. Saritas, "Vector Modulator Based Automated Active Compensation of Direct Feedthrough in Magnetic Particle Imaging," in *29th International Society for Magnetic Resonance in Medicine (ISMRM)*, (Online), 2021.